ELUCIDATING THE ORGANIC – OMS INTERFACE AND ITS IMPLICATIONS FOR HETEROGENEOUS CATALYSTS

A Dissertation

by

QINGQING WANG

Submitted to the Office of Graduate Studies of
Texas A&M University
in partial fulfillment of the requirements for the degree of

DOCTOR OF PHILOSOPHY

May 2011

Major Subject: Chemical Engineering

Elucidating the Organic – OMS Interface and Its Implications for Heterogeneous Catalysts

ELUCIDATING THE ORGANIC – OMS INTERFACE AND ITS IMPLICATIONS FOR HETEROGENEOUS CATALYSTS

A Dissertation

by

QINGQING WANG

Submitted to the Office of Graduate Studies of
Texas A&M University
in partial fulfillment of the requirements for the degree of

DOCTOR OF PHILOSOPHY

Approved by:

Chair of Committee,	Daniel F. Shantz
Committee Members,	Janet Bluemel
	Tahir Cagin
	Hae-Kwon Jeong
Head of Department,	Michael Pishko

May 2011

Major Subject: Chemical Engineering

ABSTRACT

Elucidating the Organic – OMS Interface and Its Implications for Heterogeneous Catalysts. (May 2011)

Qingqing Wang, B.S., Zhejiang University;

M.S., Zhejiang University

Chair of Advisory Committee: Dr. Daniel F. Shantz

Organic – ordered mesoporous silica (OMS) hybrid materials have attracted great interest due to their potential applications for gas separations and heterogeneous catalysis. Amine-functionalized OMS materials are active in a variety of base-catalyzed reactions. The key to successfully achieving the desired reactivity is the ability to rationally tether the targeted organic functionality onto the OMS surface. Understanding the organic-inorganic interface is crucial for rational design of heterogeneous catalysts, because the local structure and molecule dynamics are paramount in determining the reactivity of the organic groups attached to the OMS surface. This dissertation focuses on three goals that will lead to a description of the organic-OMS interface and designing hybrid catalysts: 1) Determining the dynamics of organic groups attached to the OMS surface, 2) Catalytic testing to understand how the local structure and dynamics of the organic moiety influence the catalytic properties of organic-OMS catalysts, and 3) Designing more active hybrid catalysts by introducing higher loadings of organic group using dendrimer structures. Solid-state NMR is uniquely suited for quantifying dynamic

in the milli- to nano-second time scale. Deuterium (^{2}H) NMR is a powerful tool to obtain detailed information about the dynamics or organic molecules. In this study, several simple functional groups isotopically labeled with deuterium have been attached to MCM-41 and SBA-15. The spectra display different molecular motions for different organic moieties. The results have indicated that the interactions between the functional groups and silanol groups on the surface influence the mobility of the organic fragments. Also, the porosity of the solid supports effects dynamics via confinement.

The catalytic properties of simple amine groups attached to MCM-41, containing primary, secondary, and tertiary amines have been compared in the Nitroaldol (Henry) reaction. The effects of amine identity, structure, loading, presence of surface silanols, and the substrate topology on the catalytic properties have been investigated. The result was consistent with the changes of the molecular motions shown by ^{2}H NMR measurements.

Fabricating OMS hybrid materials with high densities of organic functional groups leads to challenges in realizing uniform, catalytically active sites. Our group has immobilized melamine-based dendrimers on the surfaces of amine-functionalized SBA-15 materials by iterative synthesis procedures. The current studies in this dissertation mainly describe the catalytic properties of these dendrimers on SBA-15 and MCM-41 in the Nitroaldol (Henry) reaction, the transesterification reaction of triglycerides and methanol to synthesize methyl esters, and the cross aldol reaction between acetone and 5-hydroxymethylfurfural. The results indicate that the OMS-dendron materials have potential as solid base catalysts for a range of reactions.

ACKNOWLEDGEMENTS

I would like to express my deepest regard and appreciation to my advisor, Dr. Daniel F. Shantz, for his inspiring and valuable guidance during my dissertation work. His friendly, patient and always supportive approach has made my work and life at TAMU a very pleasant experience.

I would like to express my gratitude to my committee members, Dr. Bluemel, Dr. Cagin, and Dr. Jeong. Their valuable discussions and suggestions have improved this dissertation to a better scientific work.

I specifically thank Dr. Edgar Jordan for his great mentoring at my first step to solid-state NMR spectroscopy and a fruitful collaboration on our work. I thank Dr. Jon Lunn, Dr. Seunguk Yeu, and Victor for their interesting and fruitful discussions. I am thankful to my lab-mates Ale, Xiang, Nataly, Emily, Ben, and Fred, for the fun years of working together and thanks for their help, advice, and collaborations.

I would like to express my warmest thanks to my husband, Feijun, for his love, encouragement, endless understanding. My lovely baby Richard makes my pursuit colorful and meaningful. I also give thanks to my parents, brothers, and all other family members in China.

TABLE OF CONTENTS

Page

CHAPTER Page

LIST OF FIGURES

Page

Page

Page

Page

Page

LIST OF TABLES

Page

CHAPTER I

INTRODUCTION

1.1 Porous and Ordered Mesoporous Materials (OMS)

Porous solids have attracted much interest from academia and industry due to their high surface areas, tunable pore sizes and diverse array of accessible chemistries [1]. Porous materials have applications in ion exchanging, adsorption and catalysis because they show benefits based on their large reaction surface. Since the pore size is an important factor in many applications, porous materials can be classified into three categories based on their pore size: microporous (< 2 nm), mesoporous (2-50 nm), and macroporous materials (> 50 nm).

1.1.1 Microporous Materials

Zeolites are probably the most prominent group of microporous materials, and they are widely used acid catalysts in the petrochemical and fine chemical industries. Zeolites [2] can be described as "open 4-connected 3-D nets", AB_2 composition, A is either a SiO^{4-} or AlO^{4-} tetrahedron, and two tetrahedral are linked by a corner-sharing oxygen atom. The 3-dimensional crystalline framework of zeolites built from TO_4 tetrahedral (T=Si, Al) shows interconnected channels and cages. Figure 1.1 (left) shows

---

This dissertation follows the style of *Journal of Catalysis*.

one zeolite structure, MFI, or ZSM-5. Today, a wide variety of zeolitic structures either natural or synthetic, cover the pore size range of 0.25 to 1.5 nm [3]. The variety of pore size and pore arrangements in zeolitic structures make them useful in many applications, such as ion-exchange, separations, and catalytic reactors due to their shape and size selectivity. In addition to their porosity, the chemical compositions of porous solids also influence their properties. The development of modifications of zeolites adds new properties to the microporous materials. For example, a common way to introduce new properties to zeolites is the substitution of framework atoms by heteroelements, such as Mg, Ga, Ge, Fe, and many more. Another way is the synthesis of inorganic-organic hybrid zeolites. However, the small pore sizes (< 2 nm) of zeolites limit their applications to relatively small molecules.

MOFs (metal organic frameworks) are another useful class of microporous materials. The construction of MOFs is based on metals and organic bridging ligands. In the simplest case, a transition-metal ion (connector) is reacted with an organic ligand (linker) to form an infinite 1-D, 2-D, or 3-D framework. Self-assembled metal ions are the coordination centers, and they are linked together by the organic bridging ligands, which potentially leads to microporisity. MOFs, possessing high porosities and large surface area, are very interesting inorganic-organic hybrid materials. Figure 1.1 (right) shows the structure of MOF-5, one of the most heavily investigated MOF materials [4]. The framework is built from an octahedral $Zn_4O(CO_2)_6$-cluster by bridging carboxylate spacer ligands, such as 1,4-benzenedicarboxylate (BDC). The yellow area is the cavity of the MOF structure.

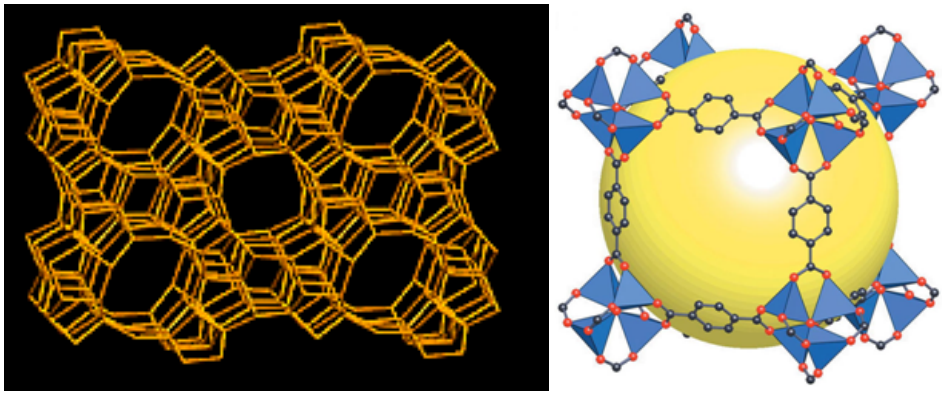

Figure 1.1. Structural renditions of MFI (left) and MOF-5 (right).

1.1.2 Macroporous Materials

Macroporous solids are materials with pore sizes larger than 50 nm. Macroporous solids show a variety of applications, especially for macroporous metal oxides, such as photocatalysis, catalyst supports, and chromatographic supports [5]. These expected applications are based on the porosity, low density, and multiple dimensional structures. Catalysis and large-molecule separation processes also require more uniform porous supports that provide optimal flow and improved efficiencies [6]. Many metal oxides display macroporous structures when they are calcined from sol-gels. Pine et al. prepared ordered macroporous ceramics of metal oxide by emulsion templating method, such as titania, zirconia, and silica [5]. The well-ordered 3-D macroporous structures of zirconium oxide particles were created by Stein and co-workers [6], as shown in Figure 1.2. Nearly monodisperse polystyrene (latex) spheres were used as a template, and simple metal alkoxide solvent was the precursors. This preparation, followed by calcination proceduces the macroporous solid. Using the

method, Stein's lab also prepared a series of highly ordered 3-D macroporous structures of inorganic oxides, phosphates, such as oxides of Si, Ti, Zr, Al, W, Fe, Sb, Zr/Y, Ni [7-10]. Another typical class of macroporous materials is macroporous beads of polymers, which are widely used as supports for solid-phase synthesis, catalysis, separations, carriers, adsorbents, and chromatographic media [11].

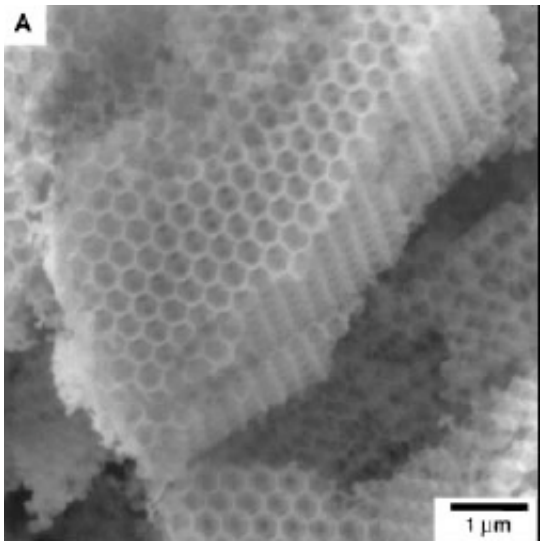

Figure 1.2. SEM image of the inorganic skeleton of a typical macroporous zirconium oxide particle after calcination [6].

1.1.3 Mesoporous Materials

Many applications require a specific range of pore size as well as high surface area. For the two classes of porous materials mentioned above, the diameters of microporous materials (< 2 nm) are too small for large organic molecules or complicated

functional fragments. While macroporous materials possess larger pore sizes (> 50 nm). The low surface area limits their use. The third class of porous materials, mesoporous materials, has attracted much interest based on their combination of pore size and surface area. Silica-based porous materials are one class of materials that possess unique properties. The unique pore sizes, shapes, and volumes of the pore structure in these materials makes significant effects on their applications. Many researches focused on introducing substitute atoms for Si in order to acquire variable frameworks as well as chemical compositions. Well-ordered mesoporous silicas have been extensively studies in the last two decades.

Beginning with the initial discovery of MCM-41 by the scientists of the Mobil lab in the early 1990s [12, 13] and the synthesis of SBA-15 by Stucky's lab [14, 15], ordered mesoporous silicas (OMS) have been intensely studied as catalysts, catalyst supports, adsorbents, and as containers for cluster/nanowire growth [1, 16-25] in the last fifteen years. There are several structural features of OMS that have led to their being heavily investigated. First, OMS materials have large surface areas and pore volumes, are of relevance for catalysis and separations. Second, OMS materials can be made that possess well-ordered pore arrangements. While hexagonal and cubic topologies are the most common observed, the development of OMS phases with a variety of pore topologies/connectivities has been explored. It is important to note that the walls of these materials are amorphous. Third, it is possible to make OMS materials that have narrow pore-size distributions. The ability of controlling or tuning the pore size of OMS has extended their applications as model system in materials research. The narrow pore size

distribution of the OMS phase results in a model support material. In the cases of the M41S and SBA classes of materials, the pore size can be tailored by changing the synthesis conditions, and can range from 1.5 to 10 nm, and 5 to 30 nm, respectively. Fourth, the surface silanols provide a specific chemical environment based on the hydrogen bonding between the silanol groups and the introduced molecules in the pores. Fifth, the surface properties can be chemically tuned by using well-developed silane chemistry, such as tethering various functionalities to the solid surface [21-24], or changing surface hydrophobicity for adsorptions of different molecules or ions. Thus, OMS materials have emerged as model supports for investigating a wide range of homogenous catalysts tethered to solid supports [26-30]. The surface silanols allow the generation of organic-inorganic hybrid materials by silane chemistry that have potential applications in catalysis, separations, sensing, etc.

Ordered mesoporous silicas are not crystalline in the matrix, however the pores possess long-range ordering relative to one another. The prototypical synthesis contains a silica source, e.g. tetraethylorthosilicate (TEOS), an organic template such as a surfactant or polymer, water, and base or acid for controlling the solution pH. Many different routes can be used to synthesize ordered mesoporous silicas depending on the choices of silicate sources, template agents, and pH range. These synthesis conditions make significant effects on the ordering of the structures, the pore size distributions, and the pore volume of OMS materials. Take the synthesis of MCM-41 for example. Kresge et al. [12] prepared MCM-41 materials with tailored pore size in the range of 1.6 nm to 10 nm by changing the alkyl chain length of the cationic surfactants, or adding auxiliary

hydrocarbons such as alkylated benzene to the synthesis mixture, or varying the reaction conditions, like temperature. Ryoo and Kim [31, 32] employed similar mixture compositions as Kresge, but they introduced acetic acid titration in the preparations, and produced MCM-41with higher long-range order, as determined by an increase in the number of diffraction peaks in the XRD patterns. In their synthesis, the mixture was titrated from time to time with acetic acid in order to keep the pH of the solution around 11 during the hydrothermal synthesis. Later, Edler and White [33-36] introduced an improved synthesis method based on Ryoo and Kim's method of pH adjusting, to prepare highly ordered all-silica MCM-41 with good stability. To control the pH the synthesis mixture was titrated repeatedly with acid (acetic, hydrochloric, or sulfuric acid) for 3 or 4 preparation days. From the comparisons of the structure based on the SAXS patterns and nitrogen adsorption isotherms, the synthesis conditions that maximized the ordering determined by XRD was determined by optimizing the mineral acid as well as the pH values. Zhao et al. [14] prepared well-ordered hexagonal mesoporous silica SBA-15 with uniform pore sizes and pore wall thicknesses. The pore sizes can be tailored in a wide range from 4.6 nm to 30 nm by using a variety of poly(alkylene oxide) triblock copolymers and by the addition of cosolvent organic molecules.

The formation mechanism of surfactant-based OMS has also been studied [37-40]. Beck et al. [13] postulated that the structure ordering observed in the mesoporous MCMs is related with the aggregation properties of the structure directing agents. They firstly proposed a Liquid-crystal templating (LCT) mechanism. As shown in Figure 1.3 B) [41], two pathways of the synthesis process were described for the LCT mechanism:

liquid-crystal-initiated and silicate-initiated. Liquid-crystal-initiated pathway indicates that the surfactant micelles arrange into ordered liquid crystals before the silicate species are added. Silica-initiated pathway indicates that the adsorption of silicate to surfactant micellar results in the ordering of micelles. Cheng et al. [42] synthesized MCM-41 with a wide range of surfactant concentrations from the critical micelle concentration (CMC) to very high concentrations where liquid crystals can form. Thus, the validity of the LCT mechanism is not settled, however most evidence points to individual cylindrical surfactant micelles becoming coated with silica and then condensing to form the hexagonal array of channels [42, 43]. Another description of OMS formation with the surfactants templates, which can also be shown in two steps, is referred to a cooperative

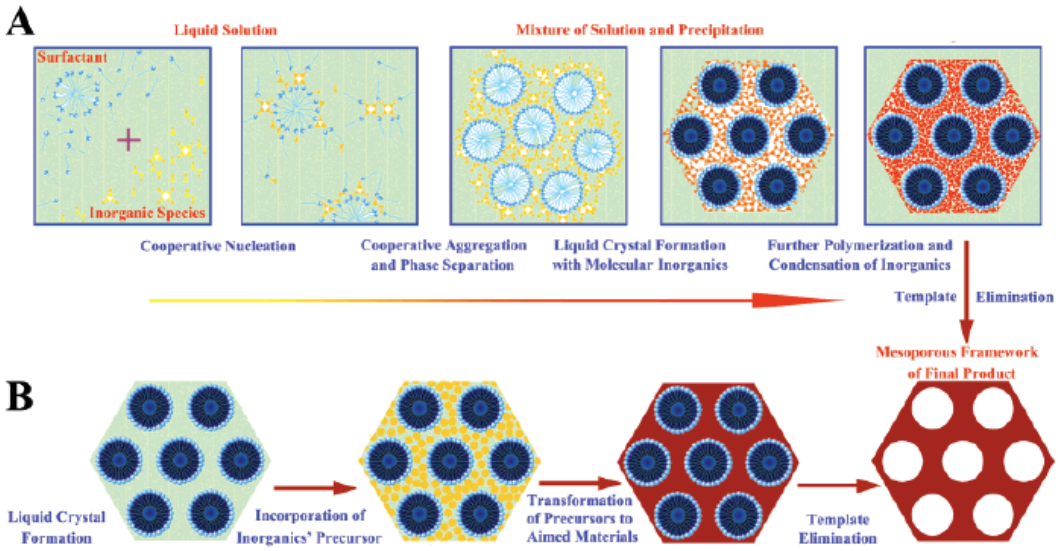

Figure 1.3. A) Cooperative self-assembly and B) Liquid-crystal-templating mechanisms which have been proposed for OMS formation [41].

self-assembly mechanism initial proposed by Stucky's group [37, 44-46] (shown in Figure 1.3 A)).

First, there is adsorption of silicate ions at the micellar interface. In this step, it is believed that the driving force is charge matching [13, 37, 44, 47-54] or hydrogen bonding [55, 56] between the SDA micelle and the silicate ions. Stucky and co-workers [37, 44, 45, 54] proposed four kinds of interactions based on charge matching between surfactant and the silicate components, and they are S^+I^-, S^-I^+, $S^+X^-I^+$, $S^-X^+I^-$ (S^+ = cationic surfactants, like long-chain quaternary ammonium cation surfactants, S^- = anionic surfactants, such as sulfonates, phosphonates, and carboxylates, I^+ = inorganic precursor cations, I^- = inorganic precursor anions, X^+ = cationic counterions, X^- = anionic counterions). Based on these interactions, it is very important to choose the chemistry of the surfactant according to the silicate source and the pH range of the mixtures. Take the synthesis of MCM-41 where cationic surfactants like CTAB are used. Then by charge matching, anionic silicate species should be chosen for the assembly, referred as S^+I^-, and usually this synthesis is performed in basic conditions. However, ordered mesoporous silica can also be synthesized by using non-ionic organic molecules, which indicates that charge matching is not the only factor. HMS and MSU, OMS materials with a worm-hole disordered pore topology, have been synthesized under neutral condition by the hydrolysis of tetraethylorthosilicate using non-ionic surfactants polyethylene oxide (PEO) by Pinnavaia and co-workers [55, 56]. They proposed the hydrogen-bonding interaction mechanism, S^0I^0 or N^0I^0, in which S^0 are neutral amines, N^0 are nonionic surfactants like the PEO surfactants used in the paper, and I^0 are

hydrated TEOS silicate oligomers. The neutral primary amine (S^0) or nonionic surfactant micelles (N^0) may be protonated by the silicate oligomers (I^0) with the hydrogen bonding interactions, and the silicate oligomers assembled to the outer surface of PEO micelles or neutral amine micelles, which makes the S^0I^0 or N^0I^0 templating work. Although only wormhole like mesoporous structures were synthesized, the hydrogen bonding mechanism extended the routes of preparing mesoporous structures via different surfactants or polymers. Well-ordered mesoporous silica SBA-15 was synthesized by using triblock copolymer P123 as a template under strongly acidic conditions by Stucky and co-workers, and an extended templating model based on the hydrogen bonding interaction, $S^0H^+X^-I^+$, was proposed [14, 15]. In a recent review by Wan [46], more kinds of interactions between the organic and inorganic species were summarized, such as coordination bonds between organic amines N^0 and transition metal I^+ in acid condition [57], covalent bond between cationic surfactants containing silicate S^+ and silicate species I^- in basic solution [58, 59]. The second step is related with the formation of long range ordering of OMS materials. There are two kinds of descriptions about the step. At the beginning, the adsorption of silicate ions onto the SDA micelles changes the surface energy of separate micelles in the solution, and then the micelles via sequential condensation of silica can rearrange and form long range ordered phases or non-crystalline structures. The other pathway is that the SDA micelles with changed surface energy aggregated first because of the adsorption of silicate, and then the disordered intermediate rearranges into the final well ordered mesoporous frameworks [60]. Although different descriptions were given for the second step, the significance of the

aggregation properties of the structure directing surfactants is in common to both. The different reaction pathways are based on the changes of the surfactant properties, the surfactant concentration in water and the effects of other ions [22, 41].

The OMS materials used in this dissertation are MCM-41 or SBA-15. Comparing the syntheses of MCM-41 and SBA-15, several differences can be found. Typically, MCM-41 syntheses are performed in basic media, while SBA-15 is prepared under acidic conditions. With the presence of CTAB, sodium silicate is used as the silicon resource. However, silicon alkoxides are used to synthesize SBA-15. The resultant products, MCM-41 and SBA-15, possess different porosity. SBA-15 possesses mesopores and the walls possess some microporosity, while MCM-41 possesses only mesopores. Figure 1.4 shows TEM images of these materials (left: MCM-41, hexagonal, 4 nm; right: SBA-15, hexagonal, 8 nm) [13, 14]. Figure 1.5 shows the comparison of the two kinds of OMS [17].

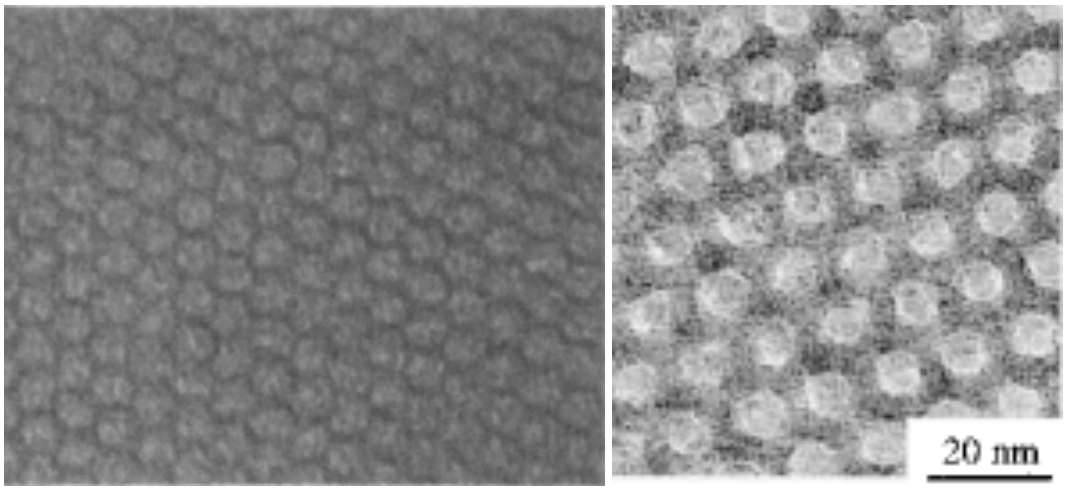

Figure 1.4. TEM images of MCM-41 (left) and SBA-15 (right) [13, 14].

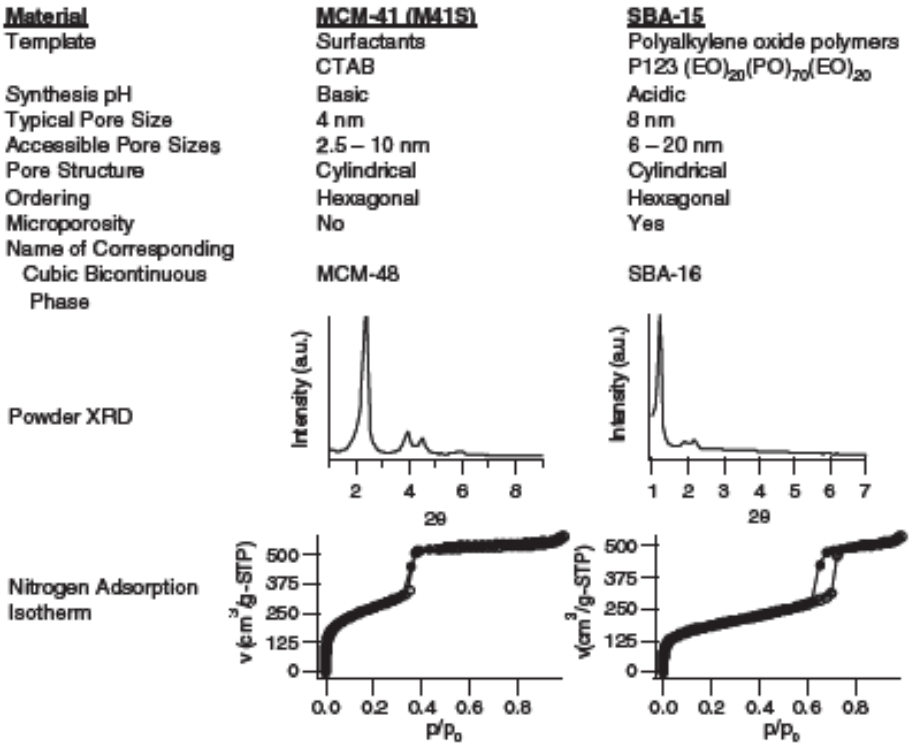

Figure 1.5. Comparison between MCM-41 and SBA-15 [17].

1.2 Organic - Ordered Mesoporous Materials (OMS) Hybrid

The initial investigations of OMS phases focused on catalysis, with the hope that aluminum-containing OMS materials would possess strong acid sites comparable to those found in zeolites. This would enable the cracking of large hydrocarbons that are too large to enter the pores of zeolites. Although this did not come to fruition, OMS was found to be a model support for producing OMS-nanoparticle and -nanowire composites, or functionalized hybrid catalysts.

Many studies attempted to introduce ionic metals into the OMS framework, and used as catalysts in different reactions [61-63]. Pauly et. al., found that aluminum substituted Al-HMS-HTx analogues showed high textural porosity and were efficient catalyst in condensed phase alkylation of 2,4-di-tert-butylphenol with cinnamyl alcohol [64]. Polyoxometalate [65] (inorganic metal-oxygen cluster compounds) was loaded in mesoporous silicas, SiW_{11}/MHS, by co-condensation route using Keggin-type monovacant as precursor, in the presence of block copolymer $EO_{20}PO_{70}EO_{20}$ (P123) and acidic conditions. The ordered surface shows hexagonal SBA-15 architecture, with directly grafted metal-oxygen cluster. The results indicate that the concentration of precusor, the prehydrolysis time of TEOS, and the aging temperature are important factors influencing the composition and structure of the hybrid material. Iglesias et al. [66] prepared Ti-MCM-41 materials with Ti loadings from 0.5% to about 35% wt by co-condensation of silicate precursors with different Ti sources. Both of the materials are active in oxidation reactions. And they found that the Ti sources influence the catalytic activity of the final materials. Loebick et al. produced bimetallic CoCr-MCM-41 catalysts used in selective synthesis of single-wall carbon nanotubes (SWNT) [67]. They combined two distinct steps to introduce two kinds of metals, incorporation and grafting. The monometallic Co-MCM-41 and Cr-MCM-41 were synthesized by isomorphous substitution of silicon atoms, and in this step the metal loading is an important factor for influencing the OMS frameworks. Then the second metallic components were grafted with refluxing the Co(II) and Cr(III) acetylacetonate with the as-premade monometallic catalysts. The results indicated that the bimetallic-MCM-41 catalysts increased the

maximum metal loading keeping the mesoporous frameworks constant ordering, which increased the yield of SWNT and narrowed the diameter distributions of small SWNT. In addition to incorporation of metal ions in the OMS frameworks, changing the surface environment, tuning the surface conditions or properties by surface passivation or introducing new functionalities by attaching organic fragments, also influences OMS catalytic properties.

1.2.1 Methods of Preparation of Organic-OMS Hybrid Materials

Two methods have been widely used for the synthesis of organic-OMS hybrid materials. A review by Hoffman and co-workers [19] has summarized many aspects of functionalized OMS materials. As shown in schematic Figure 1.6 [19] the first approach is called the direct co-condensation method, which is a ‘ one-pot’ approach. The silane containing the desired functional group is added to the OMS synthesis solution at the beginning, and the functional group is incorporated into the OMS structures during synthesis. The other method is called post-synthetic grafting. This approach contains two steps. First OMS materials are synthesized as usual, and the template is removed to generate the final porous material. Then the silane containing the desired functionality is reacted with the prepared OMS in dry toluene. Both approaches have shown advantages and disadvantages. A paper from Andreas Stein’s group compared the advantages and disadvantages of these methods by comparing the properties of vinyl functionalized MCM-41 [68]. The results of these works have shown that the direct co-condensation method is better to get uniform distribution of functional groups in the pores. However,

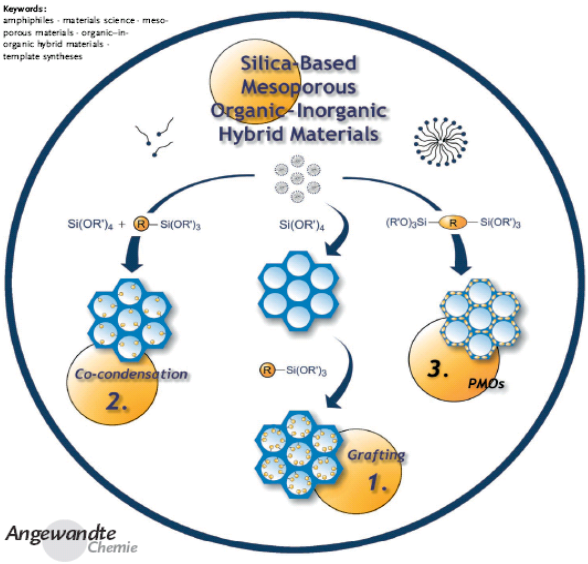

Figure 1.6. Scheme of methods of organic covalent attachment [19].

this approach can decrease the long-range ordering of the support structure because the presence of silane often leads to a disruption of the OMS pore architecture. Pikus [69-71] synthesized highly ordered SBA-15 containing ethylene, phenylene bridges or/and amine, thiol, vinyl and phenyl surface groups by direct co-condensation method. The characterized results revealed that the structural parameters, such as SBET, Vp, d and degree of ordering are dependent on the type of functionalized silane used in the synthesis. The higher concentrations of amine groups make the final structure less ordered. In the case of vinyl and vinyl/phenyl functionalized SBA-15 organosilicas, the ordering is even affected by adding relatively small amount of functional silanes. These functionalized SBA-15 organosilicas were active for the adsorption of Zn(II) ions. The results from aminopropyl-functionalized silicas by one-step co-condensation method indicated that the aminopropyl groups were condensed as the part of the silicate

framework [72]. For example, it is difficult to tune the pore diameters using the co-condensation method. If the pore size is important to the properties of the hybrid materials, the post-synthetic grafting method should be chosen. So, the organic functionalized OMS by the post-synthetic approach seems to be more hydrothermally stable and possesses a higher degree of OMS framework ordering. However, the main problem for the post-synthetic grafting method is the different loadings on the inner surface in the pore channel's direction. Vinyl groups, simple thiols or amines based on their available silicate sources can be co-condensed in the silica matrix in one step, then the prepared hybrids can be used for further immobilization of other functionalities to fulfill targeted properties or generate multiple functionalities. Lim et al. [68, 96, 129, 130] prepared vinyl-functionalized MCM-41 using both co-condensation and post-synthetic methods. Bromination reaction was used to probe the internal pore structure of vinyl-functionalized MCM-41. They synthesized thiol-MCM-41 with co-condensation method and then the product was further derived to prepare sulfonic acid functionalized MCM-41 used as solid acid catalyst.

1.2.2 Previous Research on Acid/Base, Bifunctional Organic-OMS Catalysts

One of the simple groups attached to OMS is alkyl species. The tethering of alkyl chains was performed to change the surface properties, such as hydrophobicity, surface acidity, and dielectric constant, which influence their applications in catalysis. Several kinds of alkyl chain groups, such as hexyl, dodecyl, and octadecyl groups, were attached to mesoporous organosilicas by co-condensation method using approapriate silanes [73].

The academic community has spent significant effort over the last several years investigating the catalytic properties of organic groups covalently attached to mesoporous silica [20, 24, 74-79].

Acid sites have been incorporated into OMS materials by both post-synthetic grafting and co-condensation methods, such as thiol and sulfonate ester groups [75, 80-82]. Thiol functionalized OMS can be used as a catalyst and adsorbent, but the thiol group can be subsequently oxidized to form sulfonic acid groups, or used to complex metal clusters. For example, Davis' lab [81] has designed heterogeneous catalysts with multiple sulfonic acid functional groups. They discussed the effects of the spatial arrangement of active sites on catalytic activity and selectivity. Propylsulfonic acid-functionalized hybrid silicas were used as acid catalysts for esterification reactions, as reported by Testa et al. [83]. The precursor thiol group functionalized silicas were synthesized by grafting or co-condensation methods. Catalysts with more sulfonic acid active sites were prepared by the method of in situ oxidation by hydrogen peroxide during the condensation reaction. These materials had more sulfonic groups than those from the oxidation following the post-synthetic grafting. Alvaro [75] has obtained sulfonic acid-OMS hybrid catalysts using a one-step method that does not need an oxidation step from thiol to sulfonate, and these materials showed higher activity than commercial Nafion-silica composite for the esterification of long chain fatty acids with ethanol. Nakamura and coworkers have reported synthesizing Au-OMS via the reaction of thiol-functionalized OMS with $HAuCl_4$ in a mildly acidic solution [84].

Many works have investigated the properties of amines attached to OMS.

Different simple amine groups were covalently attached to OMS by bulk imprinting [18, 81, 85-93], co-condensation [20, 68, 94-96], or post-synthetic grafting methods [97-101]. Although propylamine-functionalized OMS was found to be useful as a catalyst, further studies focused on the immobilizations of a variety of amine-functionalized silicas [102]. Researchers have focused on two aspects in order to improve the reactivity and stability of amine-OMS catalysts. First, many investigations showed that the reactivity of hybrid catalysts is indeed dependent on the dispersion and accessibility of functional sites that can be influenced by the support structure [103-108], density or isolation of organic groups [81, 90, 92, 98, 109-112], and the immobilization procedure [22, 68, 94, 100, 111, 113-115]. The second was tuning the functionality based on the targeted reactions or designing multi-functional catalysts.

Consistent with the last point several labs have extended this work into the investigation of multiple different functional groups on OMS surfaces [85, 86, 88, 91, 116-120]. Brunel and co-workers [121] introduced a nonfunctional group of phenyl silane to attempt to dilute the density of the grafted aniline as the functional group. That works suggests that the activity of aniline groups is a linear function of their number density. Works from Davis's lab [86, 88, 89, 119] have reported materials containing sulfonic acid and amine groups as well as materials containing primary amine groups with carboxylic acid groups on SBA-15. Higher conversion in the aldol reaction was obtained when weaker acid components were combined in these base-acid catalysts. Katz [91] discussed the effects of the acidity from silanol groups on the different catalytic activity and product selectivity, as well as introduced thiol groups into amine-

functionalized silica, so that bifunctional surfaces with thiol-amine pairs were prepared [85]. The results demonstrated that the reaction mechanism and product selectivity in heterogeneous aminocatalysis are critically dependent on the surface environment, especially the acidity and the polarity. Lin's group synthesized acid-base functionalized mesoporous silica nanospheres. The results [94, 116, 117, 122] confirmed that the hydrophobic secondary groups (mercaptopropyl and alkyl functionalities) played a significant role in preferentially allowing the more hydrophobic reactants to penetrate into the mesopores and react with the amino propyl groups. Their results indicate the cooperativity of the electrophile and nucleophile enhanced the reaction rates of the Aldol and nitroaldol reactions [116, 117, 122, 123]. Some cooperative action of acid-base, acid-thiol, amine-ureaa in OMS materials, especially the effect of bifunctionality and the functional group spatial arrangement, have been summarized by Margelefsky and coworkers [87]. Zhao [38, 124] utilized the amphiphilic groups (hydrophilic Si-OH groups and hydrophobic Si-O-Si groups on the surface) attached SBA-15 to provide a triphasic catalysis nanoreactor based on the tuning of multiple functional groups. Mika Linden's group has reported the applications of amine functionalized OMS in drug delivery or cellular targeting [125-127].

1.2.3 Dendrimer Organic-OMS Catalysts

The fabrication of OMS hybrid materials with high densities of organic functional groups is difficult in the sense that the distribution of catalytically active sites often becomes heterogeneous. Feng and coworkers [128] has attached high loadings of

thiol groups into OMS by the post-synthetic method. Works by Jones' lab [98-100] and Katz's lab [85, 90, 92] have shown that surface patterning and molecular imprinting techniques to achieve higher densities of homogeneous organic functional groups can circumvent this issue. Another possible approach to obtain high organic group densities is the use of surface tethered dendrimers. Dendrimers are hyperbranched polymers that can provide more active sites in a uniform distribution [131]. Dendrimer structures can not only introduce uniformly high densities of functional groups, but also make it possible to prepare spatially arranging functional groups based on the hyperbranch pattering as well as incorporating multiple functional groups. Tethering different functionalities on the periphery can make them promising for applications in gene delivery, drug delivery, molecular recognition, analytical chemistry, and multifunctional heterogeneous catalysis [132].

Triazine based dendrimers supported on silicas are an important class of hyperbranched architectures. Simanek et al. [133] showed that triazine and its derivatives possess hydrogen bond donor site of NHR end and hydrogen bond acceptor site of N=C, which can make triazines recognize other molecules by the donation and acceptance of hydrogen bonds, metal chelation, and π-π interactions. The special structure enables the synthesis of various supramolecular structures based on these branches. Cyanuric chloride (CC) was extensively used for the triazine synthesis because of its chemoselective reactivity under different temperatures shown in Scheme 1.1 [134]. Dendrimers can be grown either by a divergent or convergent mean. The melamine-based dendrimers were introduced onto silica gel surface with convergent and divergent

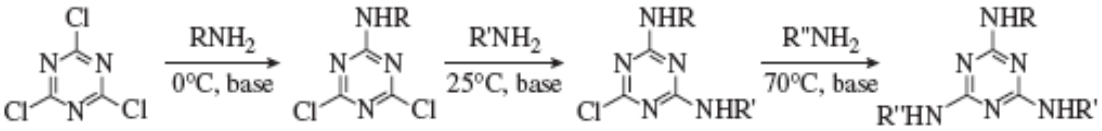

Scheme 1.1. Chemoselective reactivity of cyanuric chloride [133].

approaches [135]. As shown in the Scheme 1.2 [135], the convergent approach, which relies on the solution-phase synthesis of the dendrimer before attachment onto silica gel, can produce the dendrimer structure without apparent defects. Products made with the divergent approach show increasing percentages of organic material with each generation, but have structural defects including incomplete branching. However, the divergent strategy avoids complicated solution phase synthesis and purification steps while increasing the loading of dendritic architectures onto the silica gel surface. Our group has reported the immobilization of melamine-based dendrimers on the surfaces of amine-functionalized SBA-15 materials by the divergent process [136-138]. CC was chosen as the branching molecule, and different amines were used as the linkage molecules as well as the functionalities. The divergent strategy was chosen for the synthesis of different generations of dendrimers in the pore channels of SBA-15 [139]. Marsh et al. [139] has reported their efforts to prepare supported [1,3,5]-triazine dendritic molecules on different supports, such as Wang resin, PEGA resin, SynPhaseTM Lanterns, and silica gel, through direct desymmetrization of amine linkers like ethylenediamine.

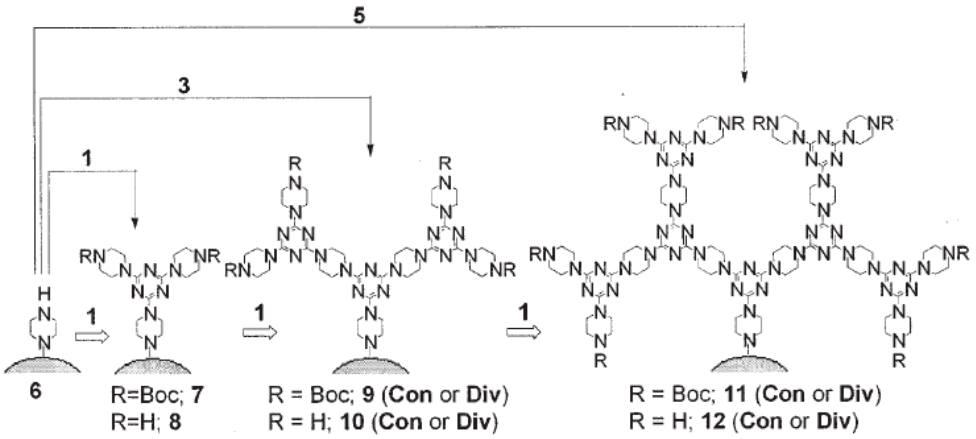

Scheme 1.2. Divergent (open arrow) and convergent (regular arrow) strategies to generate melamine-based dendrimers onto the silica gel surface [135].

Some other strategies have also been used to prepare hyperbranched architectures of amine functionality. Linden's and Jones' labs have reported ring-opening polymerization of aziridine groups to generate hyper branched polymers (as shown in the Scheme 1.3), although have yet to report their catalytic properties [140-143]. Linden's work reported preparing hyperbranched polyethylene imine (PEI) preferentially attached onto the outer surface of mesoporous silica before the extraction of the surfactant. Further, the PEI layer can be tailored with other functionalities, such as carboxylic acid groups [141].

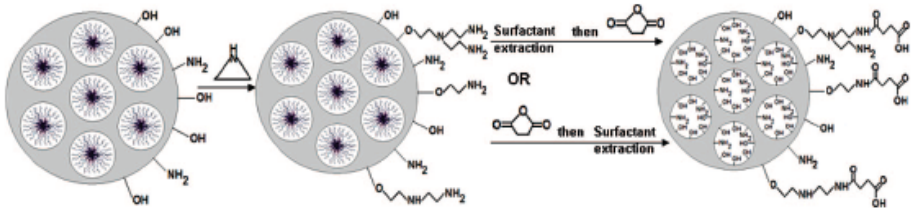

Scheme 1.3. Selective functionalization of SBA-15 with amino groups on the pore walls and carboxylic acid and amino groups on the outer surface of the particles [141].

Compared with the method of ring-opening polymerization used by Linden to tune the density of multifunctional groups, Regi et al. [144] reported their synthetic strategy for covalently bonding dendrimers to SBA-15 used for drug delivery. A spacer unit with a terminal T-silyl function was introduced to polypropyleneimine dendrimer precursors, and then the dendrimer structure was attached onto the silanol surface of SBA-15 inner channels by post-synthetic method. The degree of the dendrimer silylation by controlling the silyl functional groups in the first step determined the density of the peripheral amines.

Other dendrons were grown from silicas including OMS. Collaborative work between the Alper and Sayari labs reported investigations of polyamidoamine (PAMAM)-based dendrons in large pore MCM-41 materials 6.5 nm and 10.6 nm [145, 146]. In their synthesis, in the pore-expanded (10.6nm) MCM-41, PAMAM-based dendrimers can be loaded up to the fourth generation within the channels of silica. G1 and G2 PAMAM-SBA-15 composite were synthesized by Yan [147], and were found to be higher bonding with heavy metal ions, and selectively adsorb Pb^{2+}, Zn^{2+}, which can be used for decreasing the concentrations of Pb^{2+} and Zn^{2+} in drinking water. Juneja's group

[148, 149] reported their work of synthesis, characterization and catalytic properties of triazine based aromatic amine dendritic mesoporous silicas. The divergent method was also used here by stepwise functionalization of 2,4,6 tricholorotriazine and ethylene diamine. The new idea is that they compared the catalytic properties of triazine based aromatic amine dendrimers to those of aliphatic polyamidoamine dendrimers on mesoporous silicas in Knoevenagel condensation. The results indicated that aromatic amine catalyst couldn't be reused because of the π-π interaction between adsorbed reactant/product and the aromatic network. High density of tertiary amino groups were grown inside the channels of polyamidoamine dendritic mesoporous benzene-silicas with highly hydrophobic crystal-like pore wall structures by post-synthetic method. The results indicate that the hybrid materials are effective catalysts in Knoevenagel condensation, and the materials are also effective adsorbents for volatile organic compound removal. The hydrophobic character of the mesoporous dendritic materials and more available functional sites in the pore framework system contribute to an enhanced catalytic activity. Chaffee's group showed another important application of dendrimers on mesoporous silicas in the adsorption of CO_2. Not only PAMAM dendrimers on SBA-15 [150] can be used for the adsorption of CO_2, also melamine-type dendrons on mesocellular siliceous foam [151, 152] reported recently by Chaffee's group displayed interesting activity for this application. The results showed that the dendrimers up to generation four about 55 wt% were loaded onto the mesocellular siliceous foam with ultra large mesopores. The polyamines were branched through 2,4,6-trichlorotriazine and ethylenediamine. The hybrids possess high thermal stability, and

only primary amines are active for CO_2 chemisorption, which is also indicated by the research from Sayari's group about the interactions of CO_2 with amine-functionalized silica [153]. In a similar stepwise synthesis method, Bhagiyalakshmi et al. [154] have grafted tris(2-aminoethyl)amine(TREN) dendrimers on SBA-15 used for CO_2 adsorption as well. Recently, Shahbazi et al. [33, 155] has also reported their studies on the chemisorptions of Pb^{2+}, Cu^{2+}, and Cd^{2+} by melamine-based dendrimer amines functionalized SBA-15.

1.3 Catalytic Reactions Used for Testing Amine Functionalized OMS

Organic-inorganic hybrid materials have been used as base, acid and phase transfer catalysts [156-163]. Mesoporous silicas functionalized with amine groups have been found to be effective catalysts in base-catalyzed reactions, including the Aldol, Mannich, and Baylis-Hillman reactions [164-166]. Also, amino-OMS is useful as the intermediate for further functionalization.

The bulk of these works have investigated the reactivity of amines attached to OMS. While numerous reactions have been investigated, Aldol reactions have drawn the most attention [116, 117, 164-166]. Brunel and co-workers compared the catalytic activities of primary amino or tertiary amino groups attached MCM-41 in the Knoevenagel condensation [76]. Bigi et al. [108] indicated that the activity scale of supported amines strongly parallels that of the corresponding homogeneous counterparts, the order of amine activity being primary > secondary > tertiary in nitroaldol condensation at 90° C. Lin et al. showed that the base strength has positive

effects on the rate of the reaction [120, 167]. Kitayama and co-workers showed FSM-16 functionalized with secondary amines is more active for the aldol reaction [165, 166] than FSM-16 functionalized with primary amines. They have found that different amines have different catalytic activities for 1,4-conjugate addition of unmodified aldehydes to vinylketones: secondary > primary > tertiary > amine-free. Katz's lab [85, 90-93, 168] has prepared spatially distributed organic functional groups on silica surfaces, and by tethering different organic molecules before thermolytic deprotection they can control the positioning and the density of the amino groups. They discussed the effects of the spatial arrangement of active sites on catalytic activity and selectivity, and deduced that a cooperative effect between two proximal functional groups may be operating in these materials. The catalytic results conducted in base-catalyzed reactions, such as the Michael, Henry, and Knoevenagel reactions, indicated that acid-base cooperativity between surface silanols and primary amines also affects chemical reactivity and that the cooperativity favored the selectivity to unsaturated products. Asefa and co-workers [97] have shown the product selectivity in the Henry reaction changes if the reaction is catalyzed by secondary or tertiary amine groups attached MCM-41 [169]. Several groups have explained their results with respect to the catalytic mechanisms based on the physical and chemical properties of functional groups on OMS surface, such as the imine and ion-pair mechanisms (shown in Scheme 1.5 & 1.6) indicated by Katz [85, 91] based on different surface properties and Asefa [169, 170] dependent on the amine identity as well as nucleophile / elctrophile theory used by Brunel [77] and Lin [122].

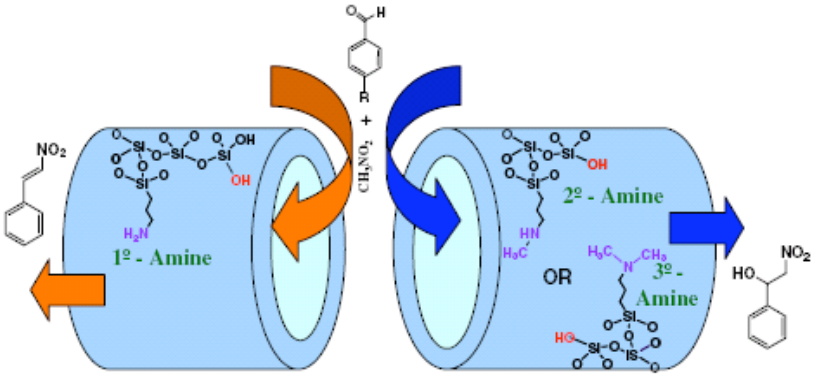

Scheme 1.5. Different products in the Henry reaction catalyzed by amines-OMS hybrids [170].

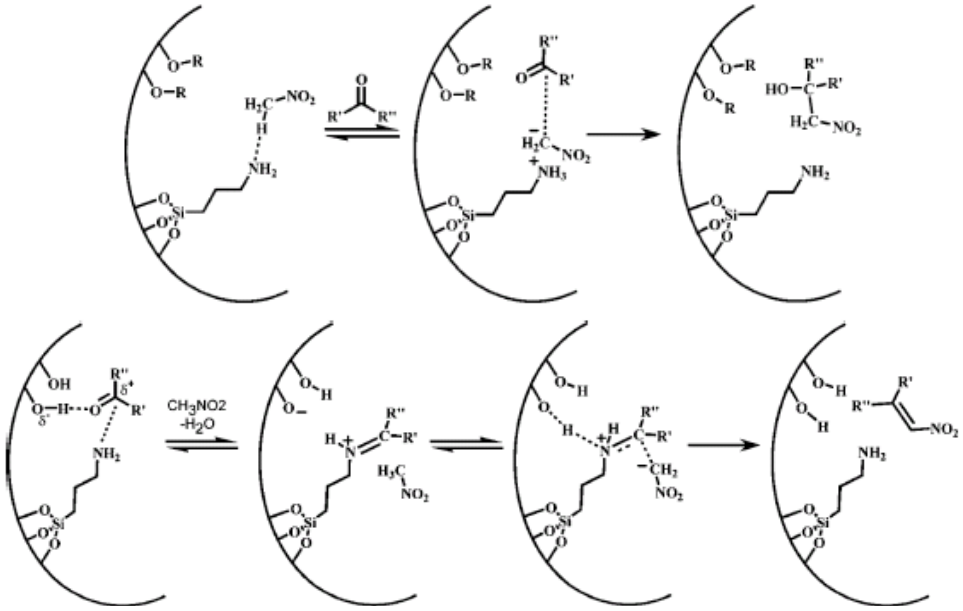

Scheme 1.6. Imine mechanism (up) for the dehydrated product, and Ion-pair mechanism (bottom) for the alcohol product in the Henry reaction [91].

1.4 Conformation of Tethered Organic Layers in OMS

In short these works have shown that not only are these materials excellent model systems for investigating supporting organic groups as heterogenized catalysts, but materials with interesting catalytic properties have been obtained. However, a basic description of the organic conformation at the surface interface is not well developed. The interface/conformation of the organic fragments covalently attached to the surface of OMS pore channels can show significant effects on the properties of the hybrid materials, especially their properties on the interface which influence their applications like using as catalysts. Dhar and Kim et al. [171, 172] have reported covalent anchoring of proline derivatives onto OMS for use as chiral catalysts, by modification of grafted chloropropyl species on MCM-41 and SBA-15. The surface hydrophobic / hydrophilic properties of the solid catalysts have great influence on their catalytic activity. They both used hexamethyldisiloxane (HMDS) to passivate the surface silanol groups to prevent sites for racemization to occur as well as tuning the organic spacer. The catalytic properties of these hybrids were tested in the asymmetric addition of diethylzinc to benzaldehyde. The effects of passivation of surface silanol groups have not been confirmed clearly, although the passivation slightly improved ee and yield %. The results indicated that the catalytic activity and selectivity of the organic groups covalently attached to OMS surface are affected by surface hydrophobicity, loading, and solvation. Recently, Lin [116] has demonstrated that the selectivity of bifunctionalized OMS originated from the variation of the physicochemical properties, like polarity and hydrophobicity. Their results confirmed that the hydrophobic secondary groups

(mercaptopropyl and allyl functionalities) played a significant role in preferentially allowing the more hydrophobic reactants to penetrate into the mesopores and react with the common propyl group. Bhaumik and Pena et al. [173, 174] found that silylated mesoporous titanosilicates, which are more hydrophobic compared with the unmodified silicas, can enhance the catalytic activity in olefin epoxidation. Zhao [174] utilized the amphiphilic groups (hydrophilic Si-OH groups and hydrophobic Si-O-Si groups on the surface) attached SBA-15 to provide a triphasic catalysis nanoreactor for the organic synthesis without any phase transfer reagent. Bass and co-workers have investigated the effects of surface hydrophobicity on the reactivity of primary amines attached OMS, and they purposed that the hydrophobicity changed the surface dielectric environment, leading to highly nucleophilic amine groups with respect to the solid surface [91].

NMR has been used to obtain information about molecular structure both in organic chemistry and inorganic materials. Some basic NMR methods (magic-angle spinning (MAS), direct polarization (DP) and cross-polarization (CP)-MAS) have been used to verify the identity and quantification of the organic group on the surface, along with FT-IR and raman spectroscopy. For example, ^{29}Si NMR has been widely used to describe the chemical shift of Si according to various coordinations of Si with OH or H. For example, the different chemical shifts of silicon sites of amine functionalized SBA-15 showed various areas of the peaks, Q^2 $[Si(OSi)_2(OX)_2]$ -92ppm, Q^3 $[Si(OSi)_3(OX)]$ -101ppm, Q^4 $[Si(OSi)_4]$ -112ppm, which can be used to analyze the active OH groups on the interface [102, 144]. Solid state NMR is also a powerful tool for quantifying dynamics over the time scale range of nanoseconds to milliseconds, and measuring the

dipolar coupling between different nuclei, resulting in a description of local structure on length scale of 1-10Å [175-177]. This information is currently lack and represents a significant contribution to the OMS catalysis community as well as the inorganic-organic hybrids community. However, few groups have investigated the dynamics of the group, such as the rotational freedom of the group, the time scale of these reorientations, and the conformation of the organic group with respect to the surface. Bluemel's group has investigated the surface immobilization of phosphines on silica via ^{31}P CP/MAS solid-state NMR [178, 179]. Their studies revealed the surface conformation of the functional groups on silica and identified side products formed on the surface. As a matter of fact, these local structural effects are the key to the catalytic activity of the organic-OMS hybrid. The dynamics of organic molecules confined in porous materials, especially in mesoporous silicas, have been extensively studied in the past twenty years. Some interesting discoveries by dielectric spectroscopy [180-182] have stimulated possible studies of the dynamics of surface covalently attached molecule in OMS surface.

1.5 Molecular Dynamics and Simulation

1.5.1 Molecular Dynamics and Previous Work

The molecular dynamics of organic molecules or polymers confined in porous materials, especially in mesoporous MCM materials have been studied in previous researches. Kremer's systematic research has displayed that the molecular and collective dynamics in confined space is determined by the counterbalance between two effects:

the surface effects and the confinement effects [180-182]. The surface effects mainly contain the interactions of the porous substrate and the attached molecules at their interface. The confinement is based on the pore size of the substrate on which the molecular fluctuations take place, the density of molecules tethered to the surface, and the length scale or flexibility of the fragments, which results in the interactions between the attached organic fragments. In the reviews, Kremer et al. [183] has summarized their studies and demonstrated that basically, the surface effects decrease the molecular dynamics while the confinement effects increase the dynamics with decreasing spatial dimensions of the confining space. The balance between the two effects decides the final molecular dynamics. Their broadband dielectric studies on the molecular dynamics of low molecular weight glass forming liquids in confined hosts, have shown that in glass-forming systems the counterbalance depends on the type of the fragmental molecules, on the properties of the pore inner surface (wettable, or nonwettable), and on the architecture of the molecules tethered to the walls (grafted, layered, or amorphous systems). The function of relaxation rate on the reciprocal temperature can show some information about the molecular dynamics and its activation energy. For example, Kremer et al. have shown three examples in order to indicate the discovery; first they compared the relaxation rates τ_{max}^{-1} for ethylene glycol (EG) confined in various zeolitic host systems. The results showed that the relaxation rates of EG in silicalite and sodalite with smaller pores are obviously higher than zeolite beta and $AlPO_4$-5. The research on propylene glycol (PG) confined in MCM-41 and MCM-48 [184] indicated that molecular relaxation in confined mesoporous environment has effects on the dynamic

glass transition. Also the comparisons of the molecular dynamics on the silanized MCM-41 or MCM-48 surface with those on the uncoated MCMs verified the effects of formation of surface hydrogen bonds on the dynamics.

Usually, in a multifunctionalized OMS catalyst, one common functional group served as a catalyst of a reaction, and the other functionality provided different noncovalent interactions to reactants and thereby controlled the reaction selectivity. However, researchers try to exploit various functional organic groups attached onto OMS to fulfill distinct goals with a trial research methodology owing to the lack of the fundamental information about the organic-inorganic interface. In short words, despite the species of the effective hybrid catalysts, how the organic layers deposited on an inorganic surface behave, how the amount of loading affects the activity, and how they modify the properties of the substrate, is not understood. The information may make it possible for us to rationally design organic-inorganic interfaces, especially attached a variety of homogeneous catalytic groups onto OMS for heterogeneous catalysts. Then a molecular picture of the rotational mobility and conformation of the organic groups with respect to the solid surface is significant. Many reports have shown that the loading of active groups makes effects on the reactivity of the hybrid catalysts. The dynamics and local structure of the functional groups on the surface influence the environment. However, obtaining the local structural effects poses a considerable challenge. There are few studies on these topics. Solid-state NMR methods offer one route to determine more details about the structure and dynamics of the organic-inorganic hybrid interface. ^{2}H NMR has been used to characterize molecular motions of isobutyric acid [185],

nitroaniline [186, 187], benzene [188] confined in mesoporous silicas. However, few researches have provided further information about the dynamics of organic groups covalently attached to the surface. Katz et al. [189] have reported their research on molecular motions of tethered carbamates on silica surface. The ^{2}H MAS NMR spectra displayed a simple two-site hopping model for the motion and proved that the bulk silica network confined the molecular mobility. In our work, we will use ^{2}H Solid-state NMR, ^{2}H MAS NMR, ^{2}H T_1 relaxation experiments, and spectra simulations to indicate the dynamics of functional layers tethered to OMS surface.

1.5.2 Molecular Dynamics and Simulation by Cerius2

Since it is not possible to get all the details or exact conformations of organic functional groups on OMS surface just dependent on the experimental data, molecular simulation is expected to provide useful insights to structure and dynamics at the organic-inorganic interface. In order to understand the data analyzed from the characterization measurements, like XRD, NMR, porosimetry, or IR, the computational modeling of the systems can give some information that can be compared with those from the experimental analysis.

Cerius2 is a molecular modeling and simulation package used for materials science and life science. It contains a broad range of application modules. Among which, diffraction module is a computational instrument for the simulation of X-ray, electron, and neutron diffraction patterns from crystalline or non-crystalline models. In the Minimizer module, the energy of molecular or periodic structures can be minimized

using molecular mechanics calculations. Also, we can perform molecular dynamics simulations to investigate time-dependant behavior of materials, like the relaxation time of the molecular motions, which can be compared with the NMR data.

1.6 Objectives and Research of Our Work

In the past decade, silica-bound organometallic materials have been investigated for using as heterogeneous catalysts. These heterogeneous catalysts offer potential advantages in organic synthesis, including simplification of reaction procedures, easy separation of products, repeated use, and unique reactivity in specific reactions. However, they generally show lower catalytic activity as compared to the corresponding homogeneous catalysts. Possible origins for the observed decrease in activity include (1) mass transfer resistances, (2) active site-surface interactions, (3) tethering the active site inhibits favorable conformations / orientations of the active site. Thus the current work is interested, from a global perspective, in understanding, at a basic level the dynamics and conformation of these tethered groups and how that impacts reactivity.

Recent research has shown that many aspects, such as the spatial arrangement, the functional series, the density, the electrochemical condition, will affect the catalytic activity and selectivity of these heterogeneous catalysts. The dynamics and local structure of the functional groups on the surface influence the environment. However, there are few studies on these topics. Solid-state NMR methods offer one route to determine more details about the structure and dynamics of the organic-inorganic hybrid interface. The principal goal of our work in the dissertation to understand how to design

organic functionality- OMS hybrid used as heterogeneous catalysts, to describe the organic-inorganic interface and interpret its effects on the catalytic properties.

CHAPTER II

EXPERIMENTAL METHODS

2.1 Introduction

This chapter summarizes the synthesis methods and analytical methods used in this dissertation. Given the prominence of NMR, the bulk of the analytical section will focus on NMR. After a basic theoretical background of NMR, the specific methods used will be described. Finally, a brief description of nitrogen adsorption/desorption isotherms will be given.

2.2 Nuclear Magnetic Resonance (NMR)

NMR spectroscopy is an indispensable method for chemical analysis, structure determination, and the study of dynamics in organic, inorganic, and biological systems [190]. With the development of new techniques, NMR spectroscopy can provide more complex information about the dynamics and three-dimensional structure of molecules in solution and the solid state.

2.2.1 Basic Theory of NMR Spectroscopy

For a nuclei to be observable in NMR spectroscopy, it most have a nuclear spin $I > 0$. In this case nuclei with spin (I) ≥ ½ have a magnetic dipole moment (μ), which in the presence of an external field (B_o) have different energy states whether or not the nuclear spin is aligned 'with' or 'against' the magnetic field. This leads to a transition

between the energy states of ΔE corresponding to the energy difference given by (shown in Equation 2-1 and Figure 2.1) [191].

$$\Delta E=\gamma \hbar B_0 \qquad (2\text{-}1)$$

γ is the magnetogyric ratio, which is a constant for each nucleus, $\hbar = h/2\pi$, h is Planck's constant, B_0 is magnetic field.

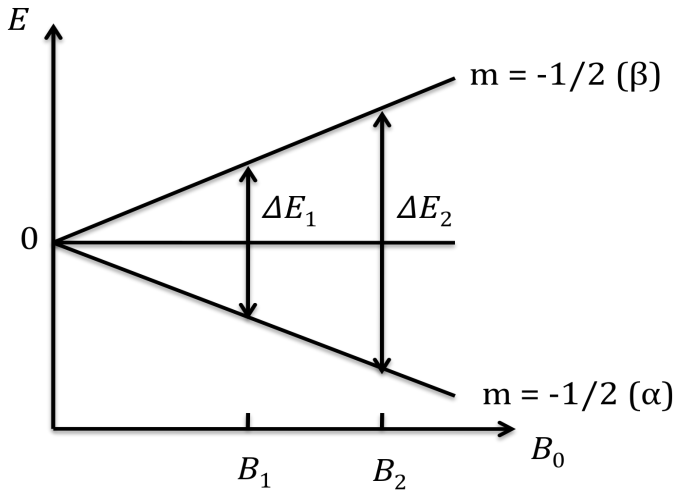

Figure 2.1. The energy difference ΔE between two split energy levels as a function of the magnetic field B_0.

In the semiclassical and simple quantum-mechanical descriptions, the spins are only treated under the Zeeman interaction. The Zeeman interaction dominates the behavior of the spin system, but contains no relevant structural information [192]. However, in the NMR spectroscopy, the local fields that the spins experienced are important, and the local fields are affected by many interactions, in solids, such as dipolar couplings between spins, shielding of the magnetic field by the electrons, and interactions

of quadrupole moments with electric field gradients. In the following, several significant interactions will be discussed.

2.2.2 Important NMR Interactions and Their Hamiltonians

2.2.2.1 Chemical Shift

The total magnetic field experienced by a nucleus includes local magnetic fields. The local field is affected by the magnetic shielding from currents of electrons in the molecular orbitals. Mainly the electron cloud determines the magnetic shielding of a nucleus, which is written as shielding constant σ, $\sigma = \sigma_{dia} + \sigma_{para}$. Additional terms from the effects of neighboring groups in the molecules and the intermolecular contributions must be combined in the interactions, such as the contribution from the magnetic anisotropy of neighboring groups σ_N, the ring current effect in arenes σ_R, the electric field effect σ_e, effects of intermolecular interactions σ_i, e.g. hydrogen bonding and solvent effects [192]. Nuclei that are not chemically equivalent will resonant at different frequencies, and the frequency difference of the signals from the reference substance divided by the frequency of the reference is referred as chemical shift δ. It is usually expressed in parts per million (ppm) by frequency. For example, tetramethylsilane (TMS) is often used as a reference component for ^{1}H and ^{13}C. The chemical shift is one of the most important parameters in NMR spectra for determining molecule structures as different chemical groups have different and well-defined chemical shift ranges. The characteristic signal positions make the spectra useful to determine the different chemical groups in a molecule. Equation 2-2 shows the Hamiltonian of chemical shifts for a given spin [192]:

$$\hat{\mathrm{H}}_{cs} = \left\{ \sigma_{\mathrm{iso}} \gamma B_o + \frac{1}{2} \delta_{cs} \left[3\cos^2\theta - 1 - \eta_{cs} \sin^2\theta \cos(2\phi) \right] \right\} \hat{I}_z \qquad (2\text{-}2)$$

In which, σ_{iso} is the isotropic chemical shift, δ_{cs} is the anisotropy parameter of chemical shift, η_{cs} is asymmetry parameter, θ and ϕ are the Euler angles.

2.2.2.2 Quadropolar Interaction

Nuclei with a spin > ½ possesses a non spherical charge distribution and thus also possess a quadrupole moment. The quadrupole moment results in an electric field gradient (EFG) around the nuclei, and the nuclear quadrupole moment interacts with the EFG. Except the Zeeman interaction, the quadrupolar interaction is the largest interaction. The first-order quadrupolar coupling can be shown in the Hamiltonian as Equation 2-3:

$$\hat{\mathrm{H}}_{Q} = \frac{eQeq}{2I(2I-1)\hbar} \frac{1}{2} \left[3\cos^2\theta - 1 - \eta_{Q} \sin^2\theta \cos(2\phi) \right] \frac{1}{2} \left[3\hat{I}_z^{\,2} - I(I+1) \right] \qquad (2\text{-}3)$$

^{2}H is an integral spin quadrupolar nucleus (I = 1); nitrogen is another relatively common investigate spin I = 1 nuclei. Some half-integer nuclei such as ^{27}Al (I = 5/2), ^{23}Na (I = 3/2) have also attracted much interest. More details about ^{2}H NMR will be given later because it is a critical topic in this dissertation.

2.2.2.3 Dipole Interaction

Magnetic dipole-dipole interaction, also called dipolar coupling, is the direct interaction between two dipoles. If the nuclei which have dipole moments are close enough, they can couple together. Equation 2-4 and Equation 2-5 display the

Hamiltonians of the interactions for the two nuclear spins, homonuclear pair or heteronuclear pair, respectively.

Homonuclear dipolar pair coupling:

$$\widehat{\mathrm{H}}_D^{//} = -\frac{\mu_o}{4\pi}\hbar\frac{\gamma^2}{r^3}\frac{1}{2}\left(3\cos^2\theta - 1\right)\left(3\hat{I}_z\hat{\mathrm{J}}_z - \hat{\vec{\mathrm{I}}}\hat{\vec{J}}\right) \qquad (2\text{-}4)$$

Heteronuclear dipolar pair coupling:

$$\widehat{\mathrm{H}}_D^{SI} = -\frac{\mu_o}{4\pi}\hbar\frac{\gamma'\gamma^S}{r^3}\frac{1}{2}\left(3\cos^2\theta - 1\right)2\hat{I}_z\hat{S}_z \qquad (2\text{-}5)$$

γ^I and γ^S are gyromagnetic ratios of the two spins, and r is the distance of the two spins. As shown in the equations, the magnitude of the interaction is dependent on the spin species, the internuclear distance, and the orientations of the two spins with respect to the external magnetic field B_0. Nuclei with high gyromagnetic ratios have stronger dipolar coupling, and the dipolar strength strongly depends on the distance ($1/r^3$). The direct dipolar coupling contains structural information and is useful for molecular structural studies. However, in solution NMR, the dipolar coupling is averaged to zero because the molecular reorientational time is fast with respect to the experiment and all angles relative to B_0 are sampled. In solid state NMR, if determining the dipolar coupling is not of interest, it is possible to eliminate or reduced them through HPDEC and MAS. However, sometimes, solid-state NMR is also used to measure the dipolar coupling between nuclei, which is related to the distance between two spins by the dipolar coupling constant D ($D = \gamma^I\gamma^S h\mu/4\pi^2 r^3$). The distance gives significant information about the molecule structures. For example, the effect of dipolar coupling on nuclear spin relaxation makes nuclear overhauser effects measurable.

2.2.2.4 J-Coupling

J-coupling, also called indirect dipole-dipole coupling, is the coupled magnetic moments from the bonding electrons of the two nuclei. The J-coupling results in the peak broken down into a complex peak, such as doublet, triplet, multiplet, and the spacing between these peaks has a fixed value (Hz). J-coupling constant is independent of magnetic field amplitude. Usually, based on the types of two spins, the coupling constants, such as J (H, H) of couplings between protons, J (H, D) of that between protons and deuterons, and J (C, C) from couplings between carbons, have attracted much interest. Higher order couplings for the spins, such as ^{2}J a geminal coupling, and ^{3}J a vicinal coupling, are also important spectral parameters for chemical structure assignment in organic chemistry. The coupling constants can be influenced by some factors based on the chemical structure, including the hybridization of the atoms involved in the coupling, bond angles and torsional angles, bond lengths, the presence of neighboring π-bonds, the effects of neighboring electron lone-pairs, and the substituent effects. J-coupling is vital in solution NMR, and depends on the spins nearby similar to the dipolar coupling. Its scalar part is very useful for group identifications in organic chemistry. However, J-coupling is not so relevant in solid-state NMR because the J-coupling values are much smaller than the other interactions discussed above.

2.2.3 Solid State NMR Versus Solution NMR

Molecules in solution with rapid reorientation due to Brownian motion, which effectively averages out the chemical shift anisotropy, quadrupole interaction, and dipolar coupling. Therefore, one often acquires narrow peaks and averaged signal positions in the

spectra. Solid-state NMR spectroscopy can provide the same information about the chemical identification as that from solution NMR. The NMR peaks observed for solids in solid-state NMR are quite different, and usually show broader lines in the spectra typically in width of many kilohertz. Solid-state NMR can also provide some information about the local structures and molecular dynamics, which cannot be determined from solution NMR. A significant but not the only factor for the broadening spectra is the anisotropic interactions. The advantage of solid-state NMR with broad line shape is that the anisotropy observed in the spectra can often directly indicate some structural/dynamic features of the solids. For example, the line shape of ^{2}H NMR spectra is solely determined by the quadrupolar interaction. The REDOR (Rotational Echo Double Resonance NMR) technique in solid-state NMR spectroscopy can tell us the distance between two spins by measuring the dipolar coupling in solids between nuclei.

Theoretically, from the Hamiltonians, the anisotropic effects are averaged to zero if the solid sample is rotated at a very high frequency about an axis inclined at 54.7° to the direction of the external field B_0. This angle of 54.7° is called the “magic angle”, and the technique is widely used as magic angle spinning (MAS). This method yields narrow signals in solid-state NMR spectra, aided by the fact that the anisotropic chemical shift and dipole-dipole couplings between the nuclei are averaged to zero, or at least reduced, by MAS. In solution NMR, the samples uniformly distribute in all the directions as well as the isotropic motion, which makes the anisotropic couplings averaged to zero. Usually, the sample tube is still often rotated around its long axis at a frequency of about 10 Hz, which can average out the motions of the nuclear spin interactions due to the spatial inhomogeneities in the magnetic field.

2.2.3.1 Solid-state ^2H NMR

Solid-state ^{2}H NMR [177] is a powerful tool for studying molecular motion, because the ^{2}H NMR line shape is a sensitive probe to the rate and geometry of the molecules confined in solids. The basic theory of ^{2}H NMR is well-documented [192-195], and here briefly summarized. Deuterium is a quadrupolar nucleus, with a nuclear spin I = 1. The static quadrupole coupling constant is between 150 and 200 kHz. Deuterium is an experimentally convenient quadupolar nuclei because the quadrupolar interaction determines the line shape [192, 196] and the quadrupolar interaction is small enough that the whole powder spectrum can be observed with high-power pulsed NMR methods. Static deuterons show a line shape of Pake doublet, and for the most general case the frequencies of the horns of the Pake doublet are given by

$$\nu = \pm\frac{3}{8}\left(\frac{2\pi e^2 qQ}{h}\right)\left(3\cos^2\beta - 1 - \eta\sin^2\beta\cos 2\gamma\right)$$
$$\eta = \frac{V_{xx} - V_{yy}}{V_{zz}} \qquad (2\text{-}6)$$

where $\left(\frac{2\pi e^2 qQ}{h}\right)$ is the static quadrupole coupling constant (~ 2π x 170 kHz), h is Planck's constant, Q is the nuclear quadrupole moment, $eq = V_{zz}$ is the principal component of the electric field gradient tensor, and β is the angle between the rotation axis and the magnetic field in the laboratory frame. The width of resonance is determined by the quadrupole coupling, which is an experimentally measurable quantity and quadrupole coupling constant (QCC = $e^2Qq/(h/2\pi)$) shows its strength. The QCC is determined by the rate and geometry of molecular motion. Motions with different rates,

axis symmetry, and molecular geometry, display distinct line shape and line width. Figure 2.2 [197] shows several kinds of simulated ^{2}H NMR spectra for different motions.

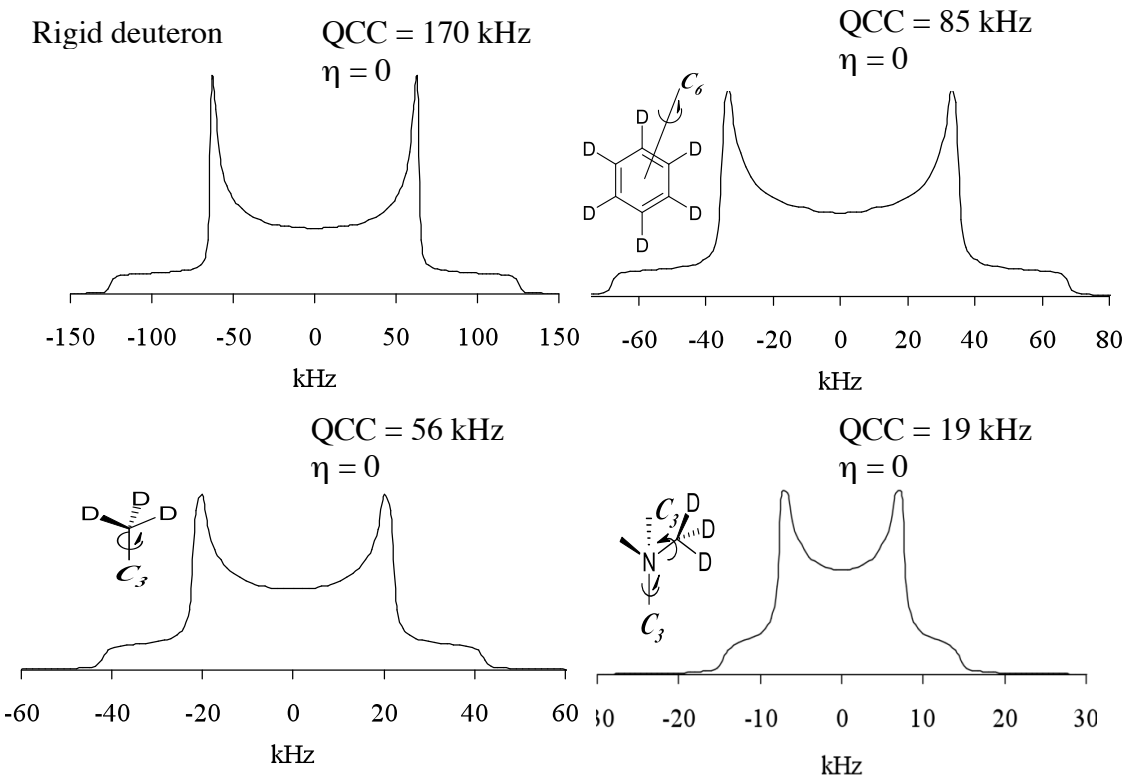

Figure 2.2. Simulated ^{2}H NMR line shapes for different motions [197].

Static deuterons have QCCs' value of approximate 170 kHz, the width of the horn is about 120 kHz, thus the NMR time scale (τ_c) is 1/(170 kHz). Fast motions on the NMR time scale ($\tau < \tau_c$) lead to line narrowing, and slow motions on the NMR time scale ($\tau > \tau_c$) do not lead to obvious line narrowing.

Although ^{2}H solid state NMR can be very useful for studying molecular dynamics, the natural abundance of ^{2}H in molecules is low which limits the sensitivity of the NMR signals. In our work, the samples are experimentally enriched in the deuterium content by grafting isotopically labeled organic fragments. Also, as shown in the

following, magic angle spinning (MAS) is extensively used in order to increase the sensitivity of the signals.

2.2.3.2 CP/MAS

Since molecules in solution NMR measurement can average out the anisotropic tensors by the reorientation from the molecular motion, the line of the spectra are narrowed down. In solid-state NMR measurement, as shown in the Hamiltonian of the interactions, the anisotropic part of chemical shift, the total dipolar coupling containing homonuclear pair and heteronuclear pair, and part of the quadrupolar interaction can be averaged to zero or the "isotropic" value by spinning the sample at a special angle, 'magic angle' of 54.74° (the null point of $(3 \cos^2 \theta - 1)$). This is called Magic Angle Spinning (MAS). The sample is placed in the measurement tube with the angle between the axis of the interaction tensor and the magnetic field B_0 to the magic angle. This operation can eliminate the anisotropic interactions, allow to obtain high-resolution spectra in solid-state NMR, which benefits the analysis of the structural information contained in the isotropic chemical shifts. The sideband intensities contain information on the anisotropic chemical shift.

Cross polarization (CP)-MAS [198-201] uses the dipolar coupling between nuclei to increase the signal of the dilute nuclei (e.g. ^{13}C) by transferring magnetization to it from abundant nuclei (^{1}H). The dipolar coupling is strong dependent on the internuclear distance, so that magnetization transfer is also dependent on the internuclear distance and magnetization should be transferred preferentially to the closest spins.

2.2.3.3 Spin-Lattice Relaxation T_1

The spin-lattice relaxation times T_1 determines the rate at which the equilibrium condition $M_z = M_0$ reasserts itself, as shown in Equation 2-7 [191]:

$$\frac{dM_z}{dt} = -\frac{M_z - M_0}{T_1} \qquad (2\text{-}7)$$

Spin-lattice relaxation arises from energy change in the spin system, as the energy absorbed from the rf pulse must be released. It is transferred to the surroundings, the lattice, increasing the thermal energy of the system. Theoretically, it has been noticed that spin-lattice relaxation times obtained in solids contain information about molecular reorientation or motion, as similar to the T_1 values measured in the solution [202]. Experimentally, T_1 is determined by the inversion recovery experiment, and the pulse sequence and the vector diagrams are shown in Figure 2.3 [191]. In this measurement method, the π pulse inverts the macroscopic magnetization, and a series of variable interpulse delay τ were used. Motions that are fast on the ^{2}H NMR time scale can be quantified using spin-lattice (T_1) relaxation experiments in conjunction with NMR line shape simulations. Performing ^{2}H spin-lattice (T_1) relaxation experiments and fitting the line shape as a function of correlation time (τ_1) using different motion models, the rates of the dynamic motion and the symmetry of rotation can be determined. Performing these experiments under different temperatures, one can determine a set of motion rates, and then from the rates as a function of 1/T, activation energies of the motion can be calculated. Thus ^{2}H NMR is a promising method for investigating local dynamics of surface tethered groups.

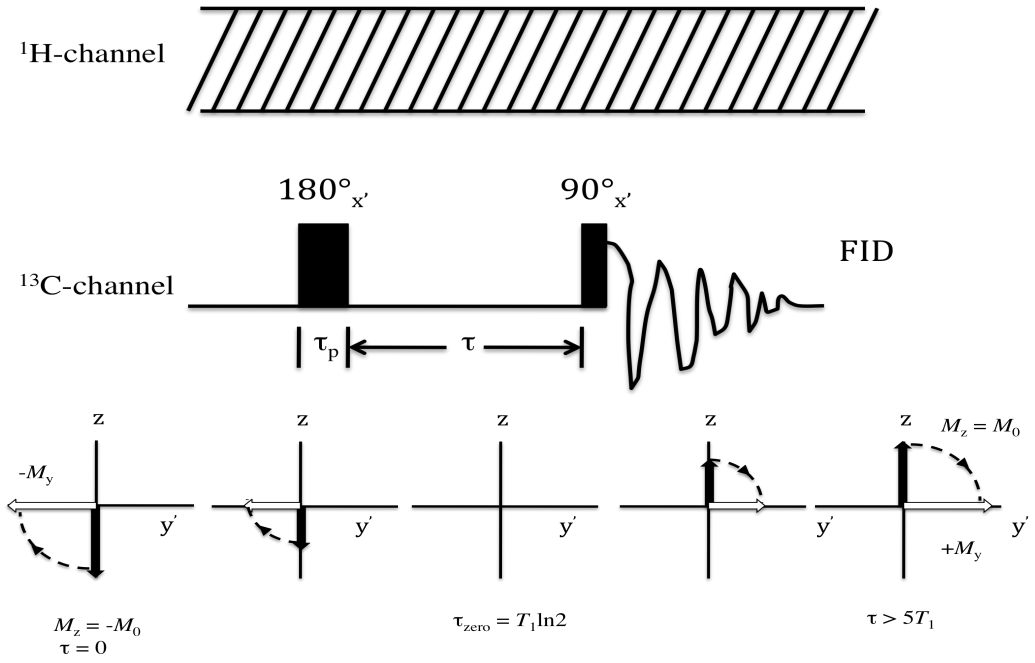

Figure 2.3. The inversion recovery pulse and the vector diagrams for five different values of τ.

2.3 N_2 Adsorption Isotherms (Porosimetry)

Porosimetry experiments can provide useful information about the pore size distribution, pore volume, and surface area of the mesoporous materials or those hybrids with organic functionality. In these measurements, nitrogen (77 K) was used as the analysis gas, and the process is physisorption that is due to van der Waals forces rather than chemical bongding, and it is reversible. The isotherm shape depends on the porous solid structure. As shown in Figure 2.4 [203], these are six IUPAC classifications of physisorption isotherms that originate from different porous structures. Among the classifictions, Type I isotherms are indicative of a microporous structure, showing

relatively small external surface area. Materials such as molecular sieve zeolites, or metal organic frameworks display Type I isotherms. Type II is the isotherm of a non-porous solid and macroporous adsorbents, and the point B is indicative of monolayer coverage and the beginning of multilayer adsorption. Type IV isotherms are characteristic of mesopores having the hysteresis loop due to capillary condensation in the mesopores. This type of isotherms from mesoporous silicas will be discussed in this thesis. Type III and V isotherms show relatively weak adsorbate-adsorbent interactions, and are not common. Type VI isotherms indicate a uniform nonporous surface.

Nitrogen adsorption-desorption isotherms are one of the most common methods to determine the porosity of porous materials. From the measured isotherms of nitrogen at 77 K, the mesopore volumes and surface area can be determined using many methods, including the α_s-method [203-205]. The mesoporous size distributions were calculated from the adsorption branch of the isotherms using the Barret-Joyner-Halenda (BJH) method with a modified equation for the statistical film thickness [206].

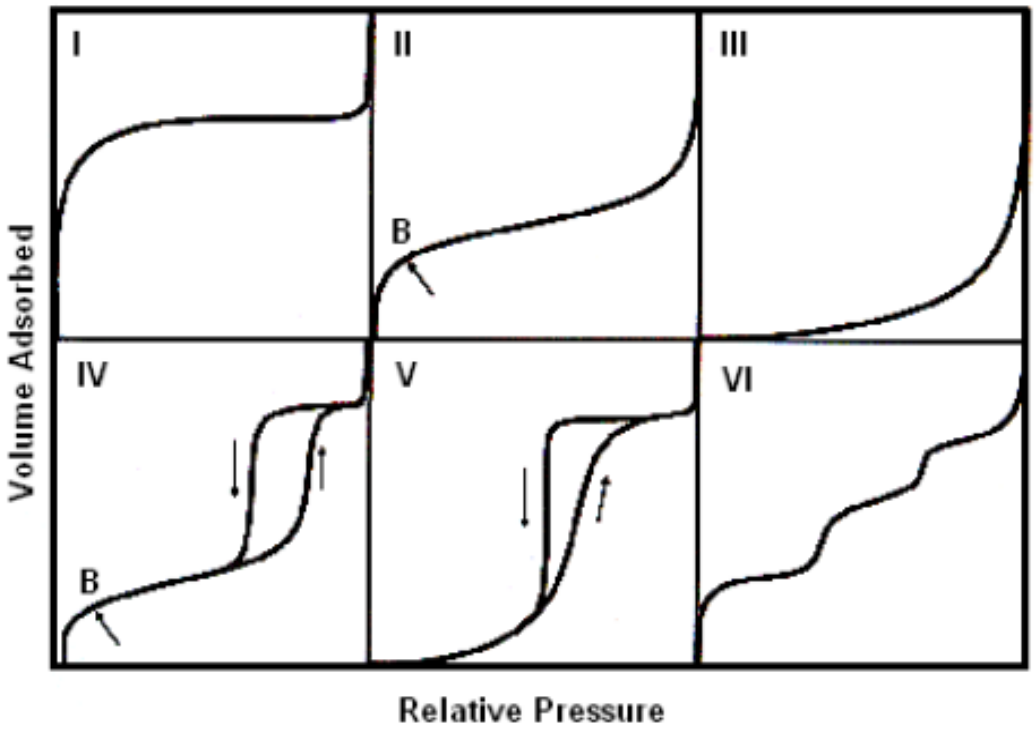

Figure 2.4. The six IUPAC adsorption isotherm types [203].

2.4 Experimental Section: Synthesis

2.4.1 Materials

Sodium silicate (PQ Brand N, SiO_2 28.7%, SiO_2/Na_2O = 3.22), cetyltrimethylammonium bromide (CTAB, Fisher Chemical, high purity grade), sulfuric acid (H_2SO_4, Sigma-Aldrich, 95-98% A.C.S reagent), sodium hydroxide (NaOH, Mallinckrodt Chemicals, pellet), methanol (Fisher Chemical, 99%), tetraethoxysilane (TEOS, ⩾99%, Fluka), Pluronic P123 ($EO_{20}PO_{70}EO_{20}$, MW = 5800, BASF), and hydrochloric acid (HCl, Sigma-Aldrich, reagent grade, 37%) were used as received. The following compounds, also used as received, were used in the post-synthetic grafting: 3-(Aminopropyl)triethoxysilane (APTES, 99%, Sigma-Aldrich),

chloropropyltriethoxysilane (TCI America, ⩾ 97% (GC)), benzyl bromide (TCI America, ⩾98% (GC)), methylamine hydrochloride (Alfa Aesar, ⩾ 98%), piperazine (Fluka, ⩾ 98%), diisopropylethylamine (DIPEA, 99%, Alfa Aesar), and hexamethyldisilazane (HMDS, Fluka, ⩾98% (GC)). Hexane (EMD Chemicals Inc., ⩾ 95%), toluene (Sigma-Aldrich, ⩾ 99.5%), and tetrahydrofuran (THF, Sigma-Aldrich, ⩾ 99%) were dried using an MBraun solvent purification system. Methanol and dichloromethane (DCM) (ACS solvent grade) and were purchased from EMD and used as received. Nitromethane (Acros, reagent ACS) and nitrobenzaldehyde (Fluka, ⩾99%, HPLC) were used as received for the Henry reaction. Glyceryl tributyrate (99%) was obtained from Sigma-Aldrich and was used as received in the transesterification reaction. 5-(hydroxymethyl)furfural (HMF) (99%, Sigma-Aldrich) was used as received in the condensation reaction with acetone. Deuterated chloroform ($CDCl_3$, D, 99.8%+1%V/V TMS, CIL Inc.) was used as the solvent for the ^{1}H NMR measurements.

The following deuterated compounds were used as received for the syntheses of deuterated methylpropylamine, benzylpropylamine, piperazine functionalized MCM-41, and deuterated trimethylsilyl functionalized MCM-41 and SBA-15: benzyl-2,3,4,5,6-d_5 chloride (ISOTEC INC., 98 % D), methyl-d_3-amine hydrochloride (ISOTEC INC., 99% D), piperazine-2,2,3,3,5,5,6,6-d_8-dihydrochloride (ISOTEC INC., 98% D), d_{18}-HMDS (Cambridge Isotopes, ⩾98% D).

2.4.2 Syntheses of Amine-MCM-41 Hybrids (Chapter IV)

2.4.2.1 OMS Synthesis

MCM-41 was synthesized using the reported procedure of Edler and White [207]. SBA-15 samples were synthesized using the method reported by Zhao and coworkers [15]. As an example for the synthesis of MCM-41, 7.9 g of sodium silicate solution were mixed with 45.4 mL deionized water. 0.27 g of NaOH were added to the solution and then 7.8 mL of 1 M H_2SO_4 were added. 7.29 g of CTAB were added to this solution and the resulting mixture stirred for 15 minutes at room temperature. The mixture was then placed in an oven at 100 °C for 24 hours under static conditions. After 24 hours the sample was removed from the oven, allowed to cool sufficiently that it could be easily handled and titrated to pH = 10 using 1 M H_2SO_4. The sample was then placed back in the oven at 100 °C. The titration step was performed two additional times in regular 24-hour intervals. The total heating period was 96 hours. For the SBA-15 synthesis 4.0 g of Pluronic P123 were dissolved in 60 mL of 4 M HCl and 85 mL of deionized water by stirring for 5 hours at room temperature. Then, 8.5 g of TEOS were added to that solution and stirred for 24 hours at 35 °C. The mixture was then aged at 80 °C for 24 hours without stirring. After the synthesis period the solid products were filtered, washed with deionized water, and air-dried overnight. The solid products were calcined to remove CTAB or Pluronic. The calcination procedure was as follows: the air-dried samples were heated from room temperature to 100 °C at a rate of 1 °C/min; held at 100 °C for 2 hours; increased from 100 to 500 °C at a rate of 1 °C/min; and then held at 500 °C for 8 hours.

2.4.2.2 Functionalization of OMS

The syntheses for generating the functionalized OMS materials are shown in Scheme 2.1. To generate the amine- and chloro-functionalized OMS materials, one gram of calcined MCM-41 was placed in a round bottom flask and dried at 100 °C under vacuum for one hour. Upon cooling 100 mL of anhydrous toluene under nitrogen was added into the flask. An aliquot of APTES (46 μL (0.2 mmol), 92 μL (0.4 mmol), 184 μL (0.8 mmol)) or chloropropyltriethoxysilane (48 μL (0.2 mmol), 96 μL (0.4 mmol), 192 μL (0.8 mmol)) was added to the solution under argon. This mixture was stirred overnight at room temperature. The product was collected by filtration, washed with 50 mL of toluene, 50 mL of methanol, and 500 mL of deionized water sequentially and then air dried. *N*-Methylpropylamine (**2**) and *N,N*-dimethylpropylamine (**5**) functionalized MCM-41 were prepared by adding *N*-(methylaminopropyl)trimethoxysilane (154 μL (0.8 mmol)) or *N,N*-(dimethylaminopropyl)trimethoxysilane (175 μL (0.8 mmol)) to substitute APTES in the procedure. Piperazine and piperidine functionalized MCM-41 were prepared from chloro functionalized MCM-41. *1-propyl piperazine MCM-41* (**3**) and *1-propyl piperidine MCM-41* (**6**). 43 mg of piperazine (0.5 mmol) or 40 μL (0.4 mmol) of piperidine and 1 mL of DIPEA (6 mmol) were added in 100 mL of THF, and stirred for 15 minutes. One gram of chloro-functionalized MCM-41 (0.8 mmol/g loading) was added into the solution. The mixture was stirred for 24 hours at room temperature. The solid product was filtered, rinsed with 50 mL of THF, 200 mL of hexane, and 200 mL of methanol and air-dried. *N-propyl-N-benzylamine MCM-41* (**4**). For the synthesis of benzylpropylamine functionalized MCM-41 one gram of amine-functionalized MCM-41 (0.8 mmol/g loading) was added into a flask with 100 mL of hexane with 175 μL (1

mmol) of DIPEA, and 119 μL (1 mmol) of benzyl bromide was added to the solution. The mixture was refluxed for 24 hours. After the reaction, the sample was filtered, rinsed with 200 mL of hexane and 200 mL of ethanol and air dried.

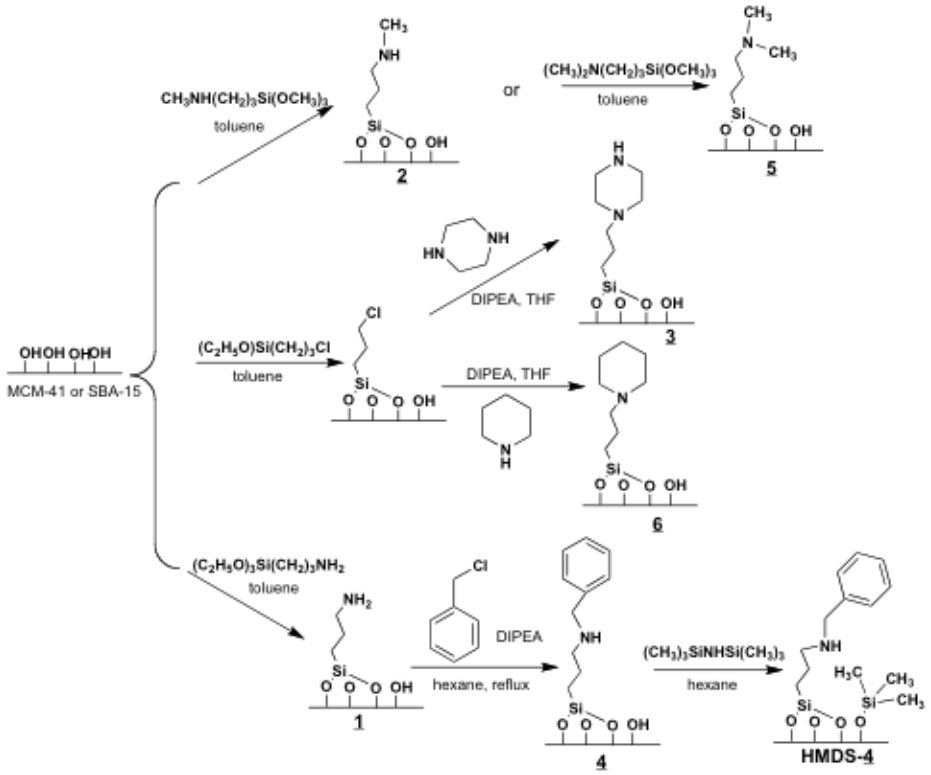

Scheme 2.1. Synthesis of functionalized MCM-41 and SBA-15.

2.4.2.3 HMDS Capping of the Functionalized MCM-41 and SBA-15

Samples were also made where the remaining silanols groups on the OMS surface were capped with hexamethyldisilazane (HMDS). A tube with one gram of functionalized OMS was evacuated on the Schlenk line under vacuum with heating for one hour. 50 mL of dry hexane were added to the sample under nitrogen. One gram (6.2 mmol) of HMDS was added into the tube under argon environment. The mixture in the

closed container was stirred overnight. The product was filtered, rinsed with 200 mL of hexane and 200 mL of methanol and then air-dried. HMDS treated-samples are denoted as HMDS-**X**, where **X** refers to the number indicated in Scheme 2.1.

2.4.3 Functionalized MCM-41 and SBA-15 with Deuterated Groups (Chapter III)

The syntheses of MCM-41 and SBA-15 follow the same procedures as shown above (sublevel 2.4.2.1). The synthesis scheme for generating the functionalized OMS materials used in Chapter III is shown in Scheme 2.2. The propylamine- and *N-propyl-N-benzylamine MCM-41* (**4**) were described in sublevel 2.2.4.2. *N*-Methylpropylamine and piperazine functionalized MCM-41 were prepared from chloro functionalized MCM-41. To generate the chloro-functionalized OMS materials, one gram of calcined MCM-41 was placed in a round bottom flask, and dried at 100 °C under vacuum for one hour. 100 mL of anhydrous toluene under nitrogen were added to the flask. An aliquot of or chloropropyltriethoxysilane (48 μL (0.2 mmol), 96 μL (0.4 mmol), 192 μL (0.8 mmol)), depending on the desired silane loading, was added to the solution under argon. This mixture was stirred overnight in the closed flask at room temperature. The product was collected by filtration, washed with 50 mL of toluene, 50 mL of methanol, and 500 mL of deionized water sequentially and then air-dried. 135 mg of *N*-methylamine hydrochloride salt (2 mmol) or 354 mg of piperazine dihydrochloride (2 mmol) and 1 mL of DIPEA (6 mmol) were added in 100 mL of THF, and stirred for 15 minutes. Then 1 g of chloro-functionalized MCM-41 (0.8 mmol/g loading) was added into the solution. The mixture was stirred for 24 hours at room temperature. The solid product was filtered, rinsed with 50 mL of THF, 200 mL of hexane, and 200 mL of methanol and then air-dried. Samples

with deuterated groups were prepared the same way as above using isotopically labeled reagents (Scheme 2.3). The designated numbers for the prepared samples referred in Chapter III are shown in Scheme 2.2. The chemical isotope labeled deuterated groups (shown in Scheme 2.3) of these three functionalities were prepared via the same process just substituting the methyl-d_3-amine hydrochloride (ISOTEC INC., 99% D), benzyl-2,3,4,5,6-d_5 chloride (ISOTEC INC., 98 % D), piperazine-2,2,3,3,5,5,6,6-d_8-dihydrochloride (ISOTEC INC., 98% D).

Deuterated trimethylsilyl groups were attached to the parent MCM-41 and SBA-15 by using d_{18}-HMDS (Cambridge Isotopes, $\geqslant$ 98% D) instead of HMDS in sublevel 2.4.2.3. The residue silanol groups on the surface of the deuterated amine functionalized MCM-41 were grafted by trimethylsilyl groups, and the samples were denoted as HMDS-**X**, where refers to the number indicated above and in Scheme 2.2. Scheme 2.3 shows the deuterated functional groups discussed in Chapter III.

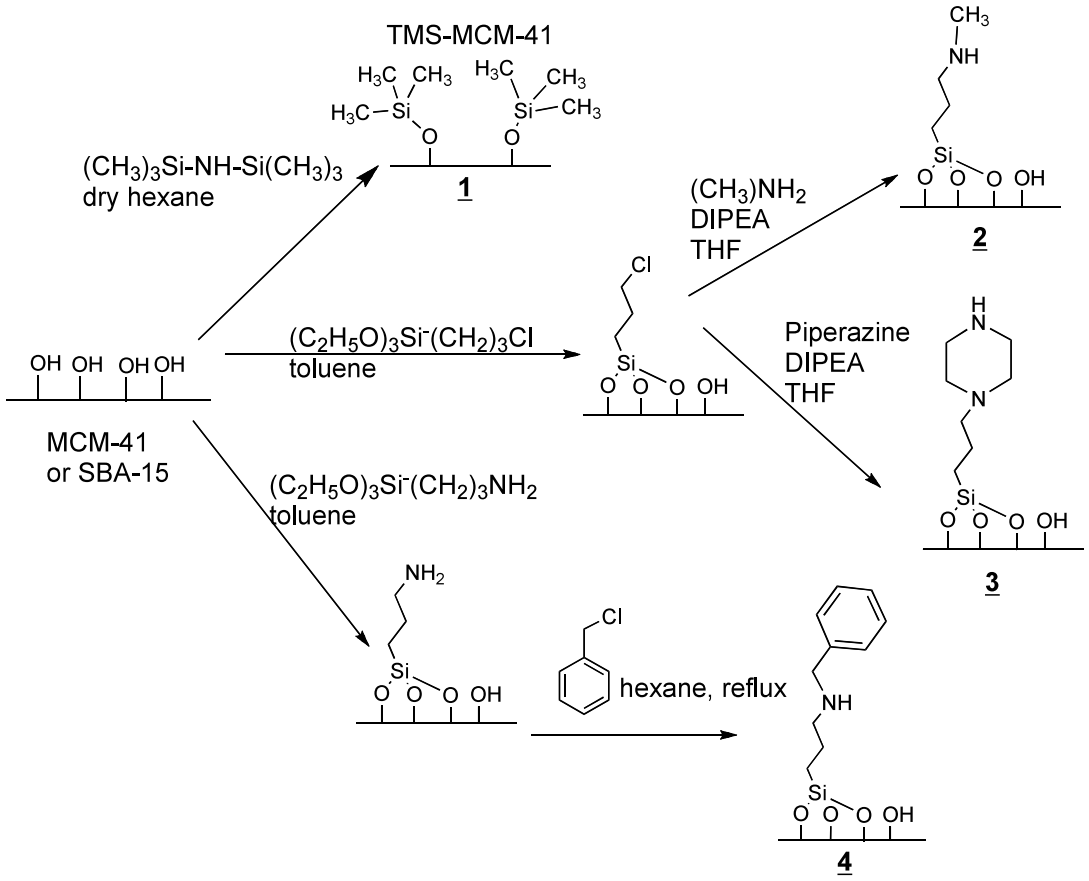

Scheme 2.2. Synthesis of OMS hybrids.

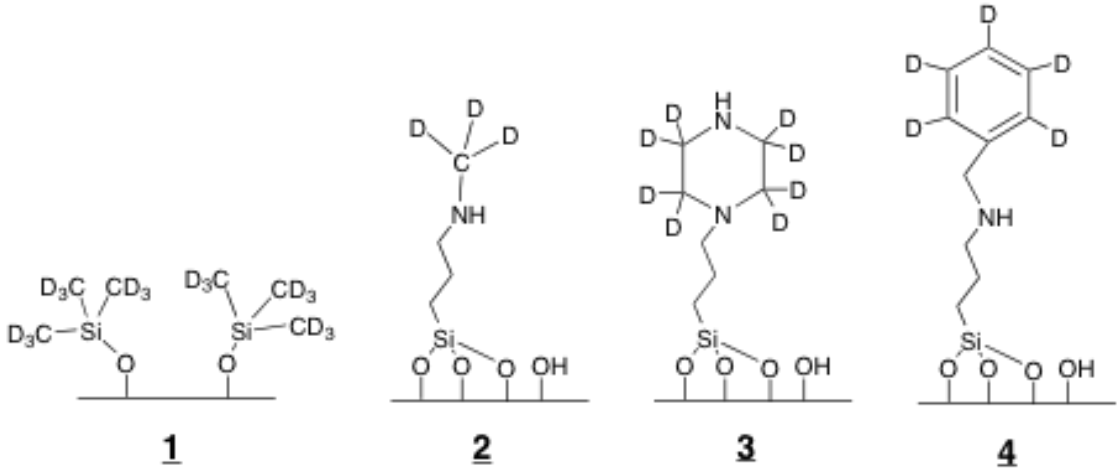

Scheme 2.3. Schematic of ligands prepared with isotopic labels.

2.4.4 Synthesis of MCM-41/SBA-15—Dendron Hybrids (Chapter V)

The syntheses of MCM-41 and SBA-15 follow the same procedures as shown above (sublevel 2.4.2.1). The synthesis method for generating the functionalized OMS materials is shown in Scheme 2.4. The amine-functionalized MCM-41 and SBA-15 samples were prepared using post-synthetic grafting. Unless noted otherwise the target loading of organic is 0.2 mmequiv/g SiO_2. One gram of calcined MCM-41 or SBA-15 was placed in a round bottom flask, and dried at 100 °C under vacuum for one hour. Then, 100 mL of anhydrous toluene was added into the flask under nitrogen. An aliquot of APTES 46 mL (0.2 mmol) was added to the solution under nitrogen. This mixture was stirred overnight in a closed flask at room temperature. The product was collected by filtration, washed sequentially with 50 mL of toluene, 50 mL of methanol, and 500 mL of deionized water, and air-dried. The synthesis of the dendron—SBA-15/MCM-41 composites was performed as reported previously by our lab [136, 137]. As an example

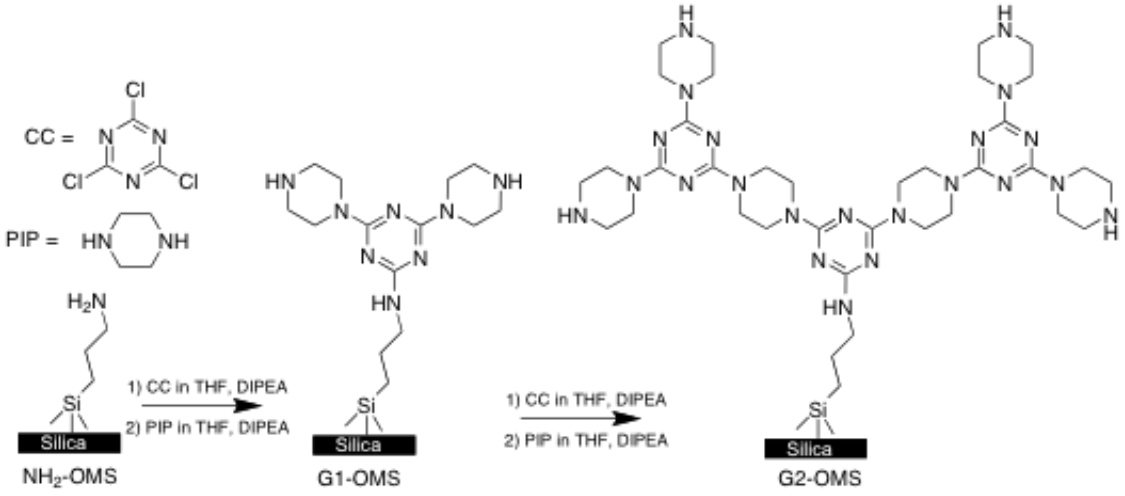

Scheme 2.4. Dendron synthesis from OMS surface illustrated with PIP.

for the case of the dendrons containing 4-(aminomethyl)piperidine as the linkers (i.e. AMP dendrons), a 0.3 M cyanuric chloride (CC) solution was prepared by adding 1.25 g of CC and 2.5 mL of diisopropylethylamine (DIPEA) (8 mmol) to 25 mL of THF. A 0.4 M 4-(aminomethyl)piperidine (AMP) solution was prepared by adding 1.25 g of AMP to 25 mL of THF. One gram of amine-functionalized MCM-41 or SBA-15 was placed in a 30 mL vial, and 25 mL of the prepared CC solution was added. The vial was shaken for 24 hours at room temperature. The solution was filtered, rinsed with 50 mL portions of methanol, dichloromethane, and THF sequentially. The silica was transferred back to a clean vial, and 25 mL of the linker molecule solution (AMP or PIP) was added, and the vial was again shaken for 24 hours. The material was filtered and rinsed as described above. This process was repeated to increase the dendron generation. Note that in all the results shown for a series of samples of different dendron generation, they are all derived from the same parent sample. For clarity, samples with dendrons made using 4-(aminomethyl)piperidine as the diamine linker are denoted as G**x** AMP dendrons, and samples with dendrons made using piperazine as the diamines linker are denoted as G**x** PIP dendrons where **x** is the dendron generation. In Scheme 2.4, piperazine (PIP) was chosen for the linker molecule as well as the functional tail, another series of samples are prepared by changing piperazine to 4-(aminomethyl)piperidine (AMP) in the scheme.

2.4.5 Synthesis of d_3-Methylpropylamine Functionalized MCM-41—Dendron Hybrids (Chapter VI)

The synthesis method for generating the functionalized OMS materials is shown in Scheme 2.5. MCM-41 was synthesized and calcined as described in Chapter II, sublevel 2.4.2.1, and amine-functionalized MCM-41 with the target loading of organic

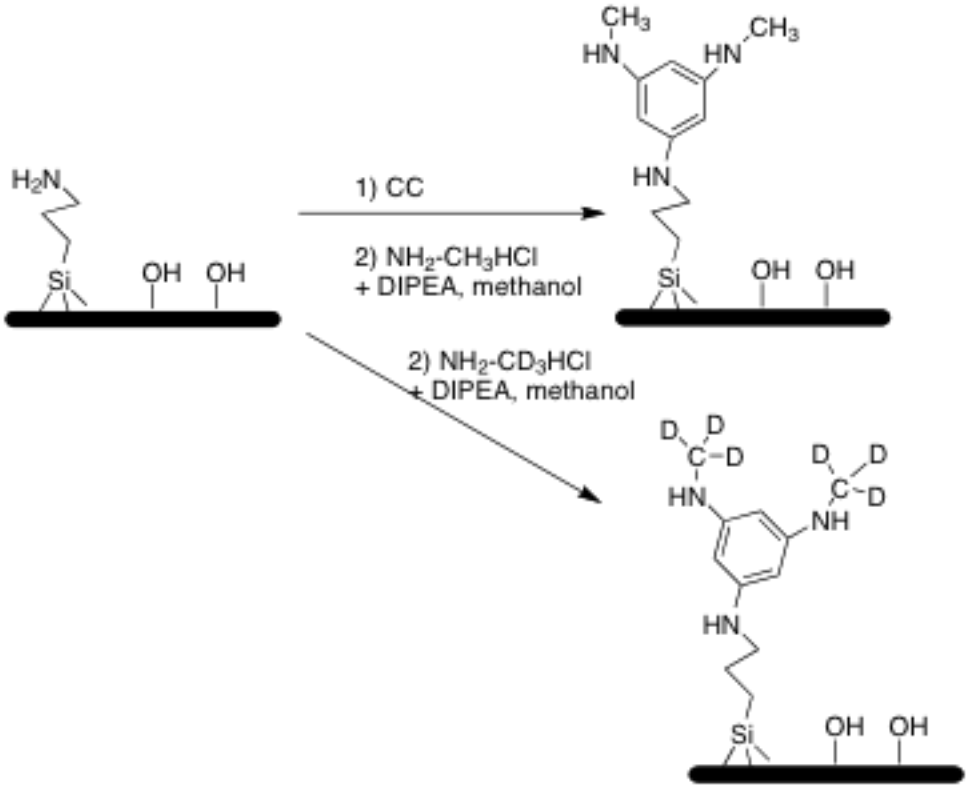

Scheme 2.5. Dendron methylpropylamine functionalized MCM-41 and its isotope labeled samples.

is 0.2 mequiv/g SiO_2 was prepared as shown in sublevel 2.4.4.2. One gram of propylamine functionalized MCM-41 was introduced into a vial that contains a 0.3 M cyanuric chloride (CC) solution, which was prepared by adding 1.25 g of CC and 2.5 mL of diisopropylethylamine (DIPEA) (8 mmol) to 25 mL of THF. The vial was shaken for

24 hours at room temperature. The solution was filtered, rinsed with 50 mL portions of methanol, dichloromethane, and THF sequentially. The silica was transferred back to a ground bottom flask (S1) with a stir bar, and 0.2 gram of methylamine hydrochloride or methyl-d_3-amine hydrochloride (ISOTEC INC., 99% D) was added into another ground bottom flask (S2) with a stir bar. Assemble the two flasks onto the Schlenk line, connect them using U-tube glass, and vacuum them. 1 M NaOH solution was prepared. The flask S1 was cooled down by liquid nitrogen. First, the two flasks were disconnected. Then, 1 M NaOH solution was dropwisely added into the flask S2 under stirring. Then the two flasks were connected, and the CD_3NH_2 molecules were introduced into S1. 25 mL of methanol was added into the flask S1, and then the flask was sealed and stirred at room temperature for 24 hours. The material was filtered and rinsed as described above.

2.5 Experimental Section: Analytical

2.5.1 Simple Amines Functionalized OMS (Chapters III and IV)

2.5.1.1 General Characterization

Powder X-ray diffraction (PXRD) measurements were performed using a Bruker-AXS D8 powder diffractometer with Cu Ka radiation over a range of 0.8-10°2θ. Thermal gravimetric analyses (TGA) were performed using a TG 209C Iris instrument from Netzsch over a temperature range of 25-500 °C using oxygen and nitrogen as carrier gases and a temperature ramping rate of 2 °C min^{-1}. Nitrogen adsorption experiments were performed on a Micromeritics ASAP 2010 micropore system using approximately 0.06 g of sample. The samples were degassed under vacuum at room temperature for 2 hours and then at 100 °C for 24 hours before analysis. The mesopore volumes were

determined using the α_s-method. The mesopore size distributions were calculated from the adsorption branch of the isotherms using the Barret-Joyner-Halenda (BJH) method with a modified equation for the statistical film thickness [206]. Elemental analysis was performed by Galbraith labs.

2.5.1.2 Solid-state NMR (Chapter III and Chapter VI)

Solid-state NMR experiments were performed at 9.4 T on a Bruker Avance. ^{1}H MAS spectra were obtained at 400.1 MHz using a 4 mm probe with ZrO_2 rotors and a spinning rate of 10 kHz. The 90°pulse length was 2.5 μs and a 5 s recycle delay was used. Adamantane was used as the chemical shift reference. ^{13}C{^{1}H} CP-MAS were performed at 100.61 MHz using a 4 mm probe with ZrO_2 rotors, a spinning rate of 9 kHz, a 2 ms contact time, a ^{1}H 90°pulse length of 2.5 μs, and a 5 s recycle delay. Chemical shifts were referenced to tetramethylsilane. *^{2}H NMR*. All ^{2}H spectra were acquired at 61.4 MHz. Static ^{2}H spectra were measured on d_9-**1**-MCM-41 and d_9-**1**-SBA-15 samples using a static probe (H6301/0014 Wideline probe, 7 mm, H7689 Coil, and HZ03348 Insert). All the ^{2}H static NMR spectra were measured using the solid echo pulse sequence [90°$_y$-τ-90°$_x$-τ-acquire] (shown in Figure 2.2) with an echo delay of 16 μs and a 90° degree pulse of 2.75 μs. The recycle delay was varied as function of the measurement temperature over the range of 1 s to 5 s. Liquid nitrogen and/or the heating system were used to control the temperature range of 295 K to 155 K in T_1 relaxation measurements for these two samples. Spin-lattice relaxation (T_1) measurements were performed using the inversion recovery pulse sequence [180°-τ-90°-acquire] (shown in Figure 2.2) with a 90° degree pulse of 2.75 μs and a 180° degree pulse of 5.5 μs. The normal inversion

recovery sequence was used given the small QCC values and resulting line widths. The value of τ ranged between 1 ms to 7 s depending on the temperature. ^{2}H MAS NMR measurements were used to measure the spectra of the functionalized OMS samples due to their low deuterium content. All ^{2}H MAS spectra were acquired at 61.4 MHz in the 4 mm MAS probe with spinning rates of either 5 or 10 kHz. All the ^{2}H MAS spectra were recorded by using a 30° pulse of 1 μs. The recycle delay was set according to different functional groups attachments: 2 s for **4** and HMDS-**4** and 1 s for **2**, **3** and HMDS-**2** and HMDS-**3**. Fitting of the ^{2}H NMR spectra was performed using Dmfit [208] and simulations of spectra were performed using SIMPSON [209].

Figure 2.2. Solid echo pulse sequence (left) [90°$_y$-τ-90°$_x$-τ-acquire] (left); inversion recovery pulse sequence (right) [180°-τ-90°-acquire] (right).

2.5.1.3 Catalytic Testing (Chapter IV)

The nitroaldol reaction (Henry reaction) was performed as follows. 100 mg of catalyst was loaded into a 10 mL Schlenk tube and heated in an oven 100 °C overnight. Upon cooling 0.38 g (2.5 mmol) of nitrobenzaldehyde and 1.35 mL (25 mmol) of nitromethane were introduced into the tube. The mixture in the tube was kept at 40 °C while stirring. After different time intervals, 100 mL of the solution was transferred into a small glass tube, 1 mL of deuterated chloroform was added to the tube, and then the solid was removed from the solution using a centrifuge. The separated liquid was analyzed

using solution ^{1}H NMR on a Mercury 300 spectrometer with a 30° pulse of 2 μs and a 3 second relaxation delay. The conversions and product selectivities were calculated by the intensity ratios of the peak (δ 5.58-5.64 ppm, ^{1}H) due to the alcohol product 1-(4-nitrophenyl)-2-nitroethanol, the peak (δ 7.6 ppm ^{1}H) due to the unsaturated product, and the peak (δ 9.9-10.1 ppm, ^{1}H) due to nitrobenzaldehyde. For the recycle studies, the solid was recovered by filtration, washed with nitromethane (2 ml, one time) and methanol (10 ml, 4 times), and dried at 100° C for one day. Note that results are reported as mmol aldehyde consumed per mmol N per g silica. Given the variable amine loading employed and the fixed amount of aldehyde added in all reactions the positions where these plots would plateau (corresponding to 100% conversion) is equal to 2.5 divided by the amine loading in mmol/g SiO_2. On the basis of this plot and other comparable experiments on multiple samples we believe the error on these measurements is +/- 5%.

2.5.2 Dendrimer Amines Functionalized OMS (Chapter V)

2.5.2.1 General Characterization

Powder X-ray diffraction (PXRD) measurements, FTIR, TGA, nitrogen-adsorption experiments were performed as shown in sublevel 2.5.1.1. Solid-state NMR experiments were performed at 9.4 T on a Bruker Avance. $^{13}C\{^{1}H\}$ CP-MAS were performed at 100.61 MHz using a 4 mm probe with ZrO_2 rotors, a spinning rate of 9 kHz, a 2 ms contact time, a ^{1}H 90° pulse length of 2.5 μs, and a 5 s recycle delay. Chemical shifts were referenced to tetramethylsilane. Elemental analysis (Si, C, H, and N analysis) was performed by the Galbraith labs.

2.5.2.2 Catalytic Testing

Scheme 2.6 shows the three reactions investigated in the work discussed in Chapter V.

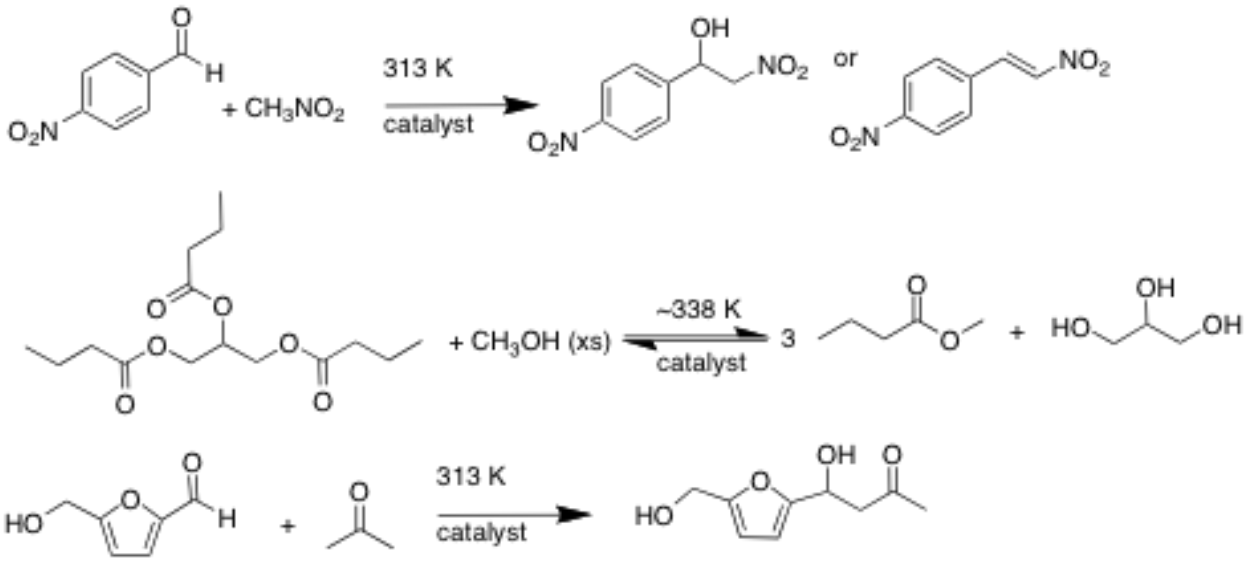

Scheme 2.6. Reactions investigated in the current work. From top to bottom: Henry reaction, methyl ester synthesis from triglycerides, and Aldol condensation of 5-(hydroxymethyl)furfural (HMF) with acetone.

The Nitroaldol reaction (Henry reaction) was performed as the procedure in sublevel 2.5.1.3.

The transesterification reaction of glyceryl tributyrate with methanol was performed as follows: to a 50 ml flask equipped with a stir bar and condenser, glyceryl tributyrate (GTB) and methanol were added in a 1:10 weight ratio (0.5g GTB: 5 g MeOH). 0.175 g of catalyst were then added. All reactions were run at reflux (~65 °C) for 6 hours. At the end of the reaction period the flask was placed in an ice bath to quench the reaction, and the solids were separated by centrifugation and the liquid phase isolated.

For kinetics measurements of conversion versus time aliquots were taken out at the time intervals noted. The conversion of the glyceryl tributyrate to methyl ester was determined from the relative intensities of the methyl ester protons (δ = 3.6 ppm, group A in Scheme 2.7)) and methylene protons adjacent to the ester group (δ = 2.2 ppm, group 3 and group B in Scheme 2.7) as has been done previously [210]. For the recycle studies the recovered catalyst was rinsed with 20 ml of methanol three times, dried overnight at 40 °C and the testing repeated.

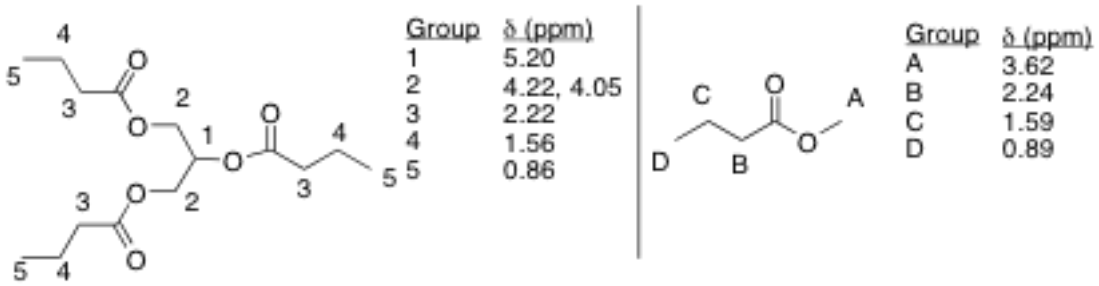

Scheme 2.7. Molecular structures of GTB and the methyl ester product, and chemical shifts of the different protons as determined by 1H NMR.

The Aldol condensation of 5-hydroxymethylfurfural (HMF) with acetone was also investigated. 100 mg of the catalyst was placed in a 10 mL Schlenk tube with a small stir bar, and heated in an oven at 100 °C overnight. Upon cooling 0.32 g of HMF (2.5 mmol) and 1.83 mL of acetone (25 mmol) were introduced into the tube. The mixture in the tube was kept at 40 °C under stirring. At different time intervals 100 μL of the solution was transferred into a small glass tube, 1 mL of deuterated chloroform was added to the tube, and then the solid was removed from the solution using a centrifuge. The liquid was analyzed by ^{1}H NMR. The conversion was calculated from the relative intensity of the furfural (δ 9.6 ppm, 1H) and the product peak (δ 4.5-4.6 ppm, 2H).

The catalytic data presented for the Henry reaction and transesterification reaction is presented as both absolute conversion of reactant and amount of substrate consumer (or product formed) per mmol of nitrogen per gram of silica. The latter is an attempt to normalize the reactivity data to an effective mmol of amine basis, as the different samples have different amine contents.

CHAPTER III

^{2}H NMR STUDIES OF SIMPLE ORGANIC GROUPS COVALENTLY ATTACHED TO ORDERED MESOPOROUS SILICA*

3.1 Introduction

Silica-bound organic-inorganic hybrid materials have attracted a great deal of interest not only from the vantage of catalysis but also adsorption, etc. In contrast to the number of works performed in the synthesis, characterization, and catalytic properties of these hybrid materials, an intellectual problem with potential relevance to all of these applications is the conformation and dynamics of these functional groups, and how that changes with loading, grafting protocol, etc. While a few works have investigated the diffusion/mobility of adsorbates in MCM-41 [185, 188, 211], we are not aware of any works where the dynamics of surface tethered groups in OMS have been investigated by ^{2}H. A few notable studies have investigated these materials via probe molecule binding to assess issues such as site interactions, steric effects, etc. [85, 90, 91, 98-100] Defreese and coworkers[189] have reported on the dynamics of tethered carbamates on imprinted silica surfaces. The ^{2}H MAS NMR results were consistent with a simple two-site dynamic model, and indicated that the bulk silica network confined the molecular mobility.

---

* Reprinted with permission from "2H NMR Studies of Simple Organic Groups Covalently Attached to Ordered Mesoporous Silica" by Q. Wang, E. Jordan, and D. F. Shantz, J. Phys. Chem. C 113 (2009) 18142-18151.

This chapter described our studies on the dynamics of several chemically simple organic functional groups covalently attached to ordered mesoporous silica (OMS) using solid-state ^{2}H NMR spectroscopy, in the hope that this will provide complementary information to the catalytic investigations and probe molecule-binding studies that have been performed by others. Trimethylsilyl groups, methylpropylamine, benzylpropylamine, and piperazine are introduced to the surface of OMS by post-synthetic grafting, and the materials were characterized by XRD, nitrogen adsorption isoterms, and TGA. The work of this chapter will focus on the results from solid-state ^{2}H NMR measurements, which can provide information about the dynamics of the covalently attached functional groups. The dynamics of different secondary amine groups were compared. Their catalytic properties are discussed based on their application in the nitroaldol (Henry) reaction in Chapter IV.

3.2. Experimental

MCM-41 and SBA-15 were synthesized and calcined as described above. Amine-functionalized MCM-41 samples were prepared using post-synthetic grafting. Different secondary amines including methylpropylamine, benzylpropylamine and piperazine were covalently grafted on the surface of MCM-41 pore channels based on the propylamine-functionalized or propylcholor-functionalized MCM-41. Trimethylsilyl groups were attached to the pure OMS surface in order to substitute the silanol groups. Deuterated

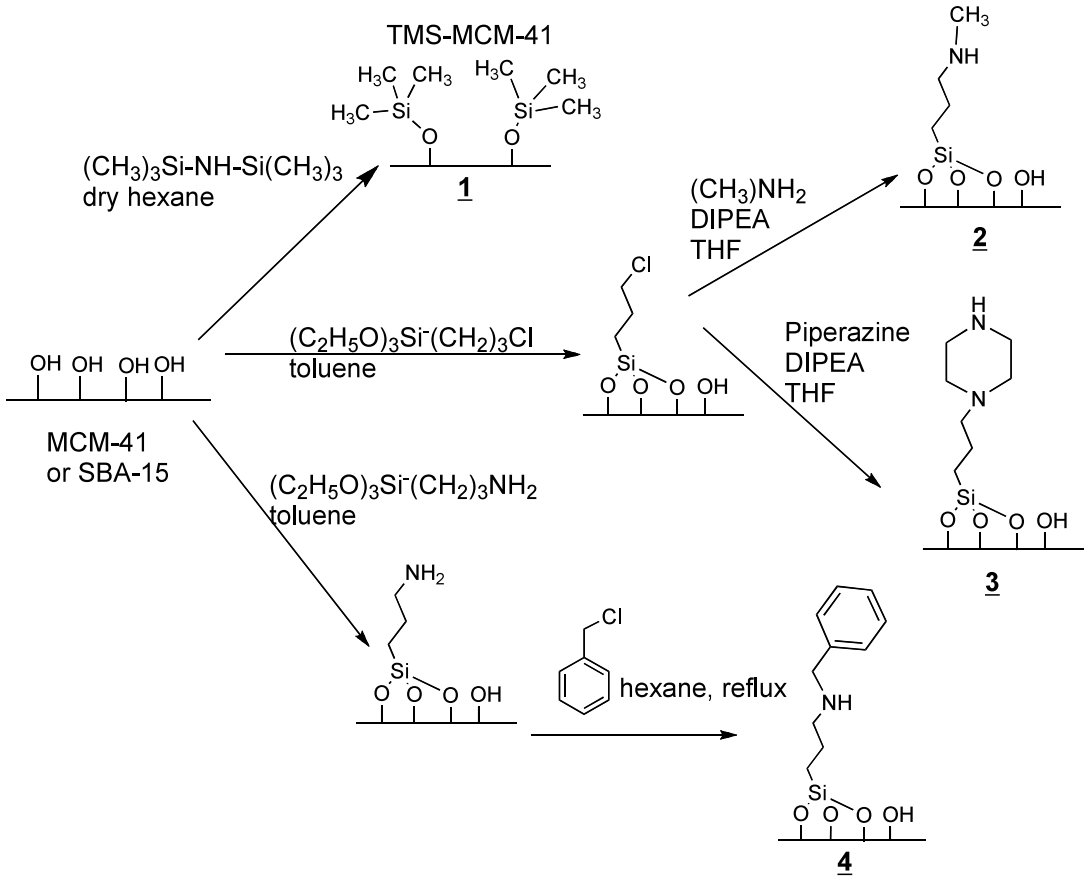

Scheme 2.2. Synthesis of OMS hybrids.

trimethylsilyl groups, methylpropylamine, benzylpropylamine, and piperazine are introduced to the surface of OMS in the same way as their normal groups in order to improve the sensitivity of the ^{2}H signal/noise ratios. More details about the synthesis, the isotope chemistry, and the designated numbers for the samples can be found in Chapter II, and the scheme 2.2 and 2.3 are shown again as follows.

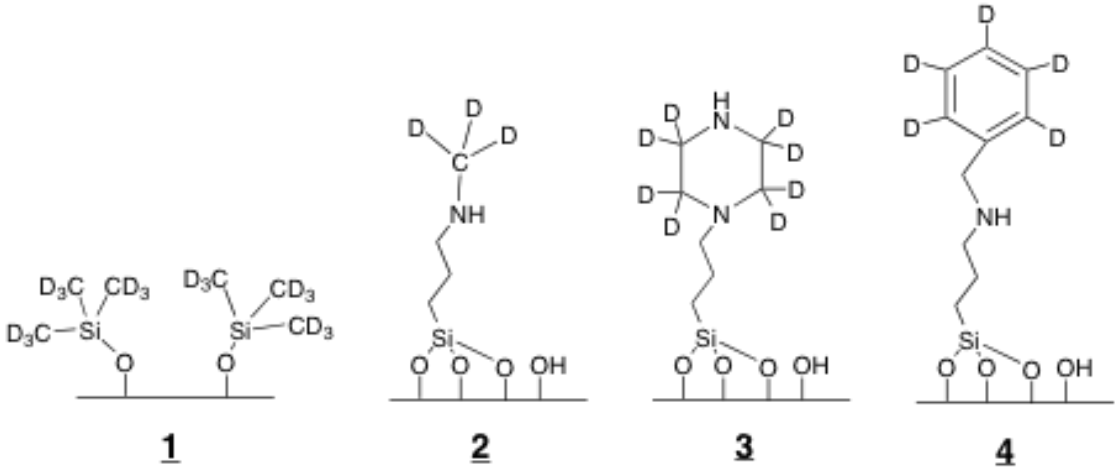

Scheme 2.3. Schematic of ligands prepared with isotopic labels.

3.3 Results and Discussion

3.3.1 General Characterization

Figure 3.1 shows the powder X-ray diffraction pattern and the nitrogen adsorption isotherm of a representative MCM-41 sample. The sample is highly ordered based on the observation of four Bragg reflections in the PXRD pattern, consistent with previous work by Edler and White [207]. The nitrogen adsorption isotherm is consistent with previous reports, and analysis of it using the α_s method gives a surface area of 940 m^2/g and a pore volume of 0.77 cm^3/g. The BJH analysis of the isotherm gives a nominal pore size of 37 Å, in line with previous reports.

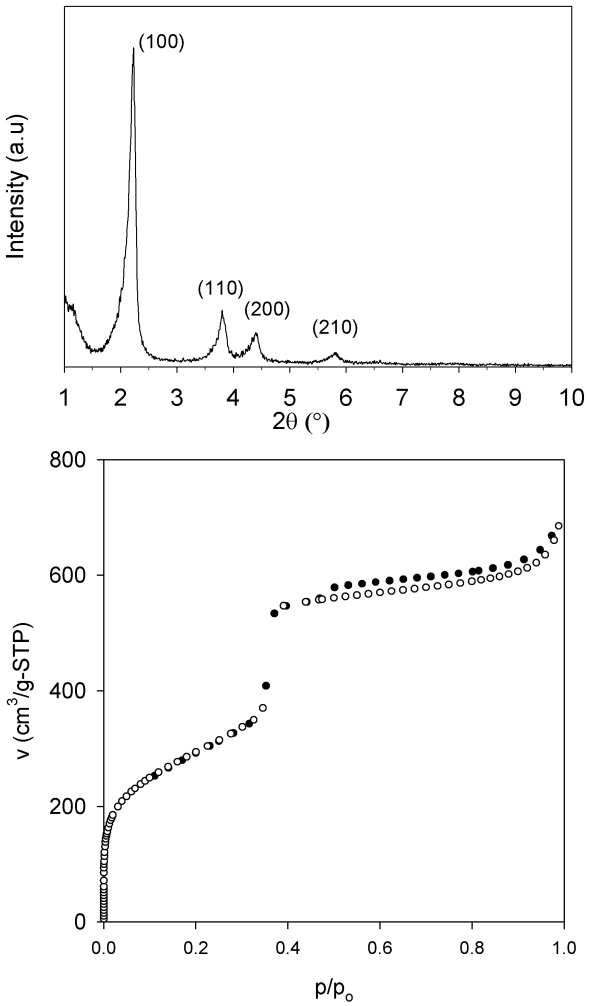

Figure 3.1. Powder X-ray diffraction (top) and nitrogen adsorption isotherm (bottom) of a representative MCM-41 sample before functionalization. In the isotherm open and filled circles represent the adsorption and desorption branches respectively.

Figure 3.2 shows selected nitrogen adsorption isotherms of the OMS-composite materials. The data for all the samples investigated are summarized in Table 3.1. The pore volume and pore size decrease systematically with organic loading and size of the organic group, as the relative pressure at which capillary condensation occurs decreases as the organic content increases. Based on BJH analysis, the pore diameter changes most

significantly upon HMDS capping, with a decrease on the order of 1 nm as compared to the parent MCM-41.

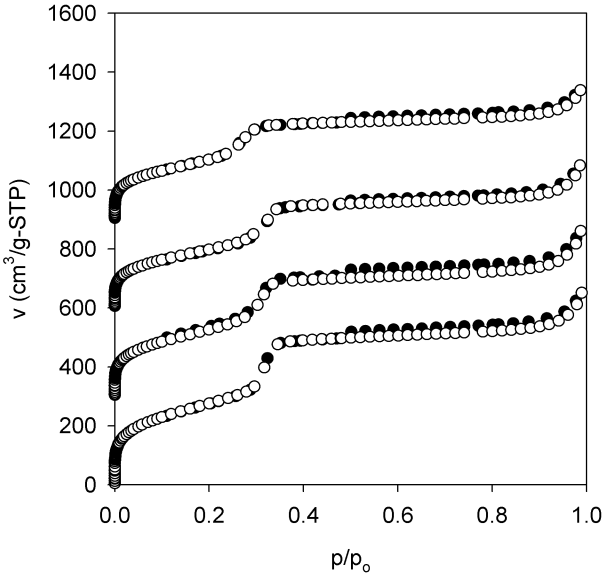

Figure 3.2. Nitrogen adsorption isotherms for (from top to bottom) **4**, **2**, **3**, and NH_2-MCM-41, all at 0.8 mmol/g target loading. Isotherms are shifted by 300, 600, and 900 cm^3/g-STP, respectively.

Table 3.1. Summary of adsorption data for the samples reported in the current work, 0.8 mmol/g loading.

Sample	$S_{\alpha\text{-}s}$ (m^2/g)	$v_{meso,\alpha-s}$ (cm^3/g)	v_{total} (cm^3/g)	Pore size (nm)
MCM-41	916	0.74	0.94	3.8
NH_2-MCM-41	948	0.69	0.86	3.5
2	705	0.48	0.63	3.4
3	812	0.55	0.72	3.4
4	699	0.46	0.59	3.2
HMDS-**4**	594	0.25	0.36	2.9

The organic content was determined using thermal gravimetric analysis (TGA) in combination with elemental analysis. The TGA results indicate the loading of organic groups is close to the anticipated values. As an example, the samples of **4** with target loadings of 0.2, 0.4, 0.8 mmol/g silica have loadings of 0.34, 0.41, 0.66 mmol/g as determined by TGA results. The results show that the higher loading sample had lower grafting efficiency. Elemental analysis was also performed on selected samples to corroborate the TGA data. The Table 3.2 and 3.3 contain the TGA and elemental analysis data, respectively. These results show that the actual organic content at low loadings (0.2 mmol/g) is very similar to the target values (1.87 wt% of C to 1.68 wt% of C in the sample of **3**). It is systematically observed that the actual organic content at higher target loadings is lower than anticipated. The results from the elemental analysis are consistent with the TGA results. The TGA analysis also provides estimates of the loading of HMDS groups. Taking **4** and HMDS-**4** as examples, the estimated loading of HMDS groups

Table 3.2. TGA summary

Samples	Initial weight (mg)	%wt change	Mass of organic (mg)	MW of fragment (g/mol)	Loading (mmol organic/g MCM-41
NH_2-M-0.8	6.00	3.9	0.21	58	0.70
4-0.8	8.04	8.9	0.67	148	0.66
HMDS-**4**-0.8	11.94	12.88	1.49	148+45(TMS)	0.66+1.02(TMS)
4-0.4	7.98	5.7	0.41	148	0.41
4-0.2	10.6	4.76	0.50	148	0.34
3-0.8	6.21	8.78	0.515	126.5	0.76

Table 3.3. Elemental analysis summary

Samples	C content (theor. value) / wt%	N content (theor. value) / wt%	Si content (theor. value) / wt%
3-0.8	4.07 (6.72)	< 0.5 (2.24)	37.4 (47)
3-0.2	1.87 (1.68)	< 0.5 (0.56)	31.9 (47)
4-0.8	6.95 (9.6)	0.76 (1.12)	36.0 (47)
4-0.2	3.30 (2.4)	< 0.5 (0.28)	37.2 (47)

based on TGA for HMDS-**4**-0.8 is 1.02 mmol/g (determined by difference between **4** and HMDS-**4**). While we do not know if all the silanol groups are terminated via capping, FTIR spectra of **4** and HMDS-**4** (Figure A1) show that the peak at 3400 cm^{-1} for the O-H stretch almost disappears after HMDS capping. Previous literature is varied in terms of estimates of the silanol group density on MCM-41 with values reported between 1 and 4 mmol/g [212-214]. However, qualitatively based on the IR and TGA results, we can state

that the number of silanol groups present after HMDS capping is significantly reduced. This is relevant to the analysis of the ^{2}H NMR results below.

Evidence of organic group incorporation is also obtained from $^{13}C\{^{1}H\}$ CP-MAS NMR. Figure 3.3 shows the spectra of **3** and HMDS-**3** materials as representative examples. There are three resonances at 6.5 ppm, 23 ppm, and 42 ppm for both **3** and HMDS-**3**. These signals correspond to the three carbons of propyl groups, among which the signal at approximately 6.5 ppm is the carbon directly attached to the silicon center.

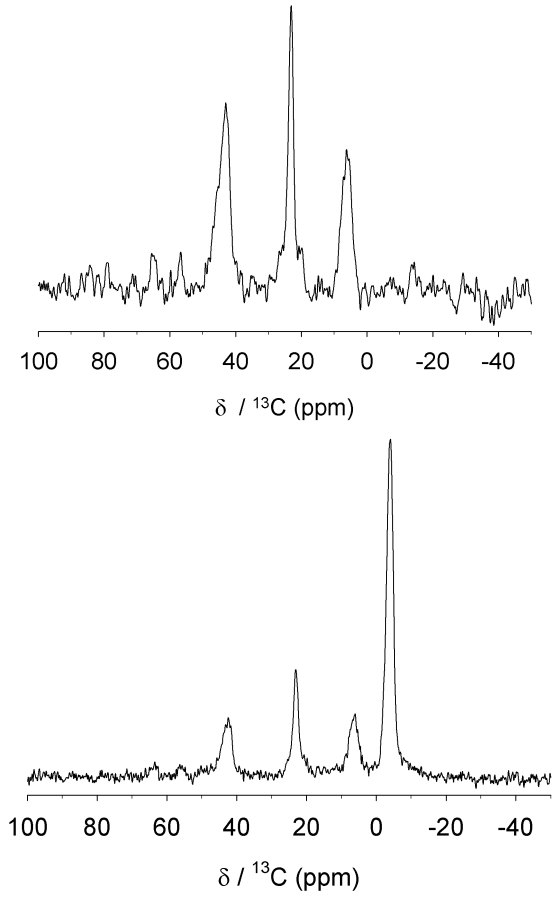

Figure 3.3. $^{13}C\{^{1}H\}$ CP-MAS spectra of (top) **3** and (bottom) HMDS-**3**. Target loading for both samples is 0.8 mequiv/g.

The resonance at 45 ppm in both spectra is due to the aliphatic carbons of the piperazine group. In the spectrum of HMDS-**3** in addition to these resonances there is a line at -3.3 ppm attributable to the trimethylsilyl group. These results above indicate that these amine-OMS materials are well characterized and there is reasonable evidence that the organic groups are at or near their target loadings and that the desired groups are present intact on the surface. The remainder of the chapter will focus on the dynamics of these functional groups.

3.3.2 Solid-state ^{2}H NMR

3.3.2.1 Static ^{2}H NMR and Spin-lattice Relaxation Spectra of Trimethylsilyl Groups Attached MCM-41 or SBA-15

While innumerable studies of grafted OMS materials have appeared in the literature, there is a dearth of works reporting the rotational dynamics of these groups. Thus as a starting point the dynamics of the trimethylsilyl groups formed during HMDS capping of SBA-15 and MCM-41 were investigated. Figures 3.4 and 3.5 shows the static ^{2}H NMR spectra and fits of d_9-**1**-MCM-41 and d_9-**1**-SBA-15 measured at room temperature and low (< 200 K) temperature.

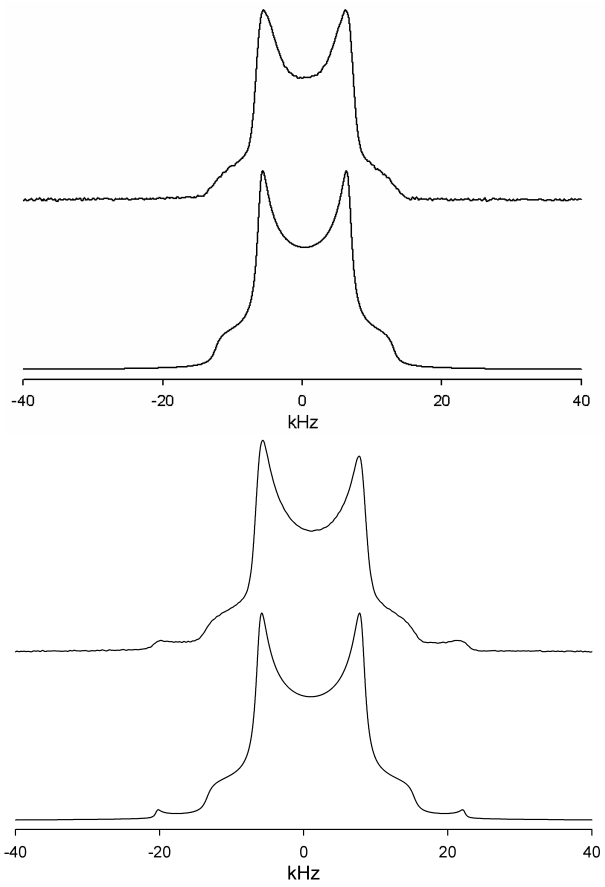

Figure 3.4. Static ^{2}H NMR spectra (top trace) and fits (bottom trace) of d_9-**1**-SBA-15 at 295 K (top) and 175 K (bottom).

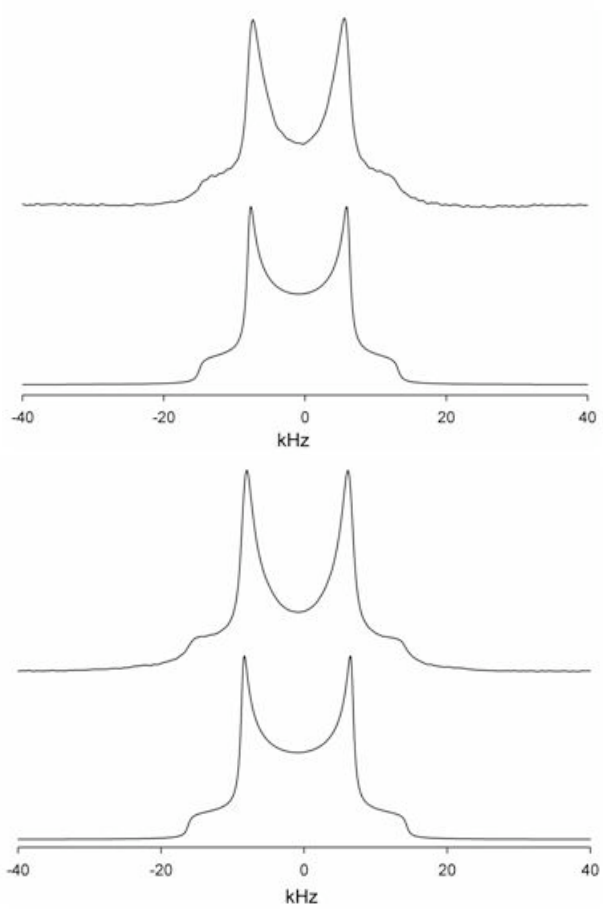

Figure 3.5. Static ^{2}H NMR spectra (top trace) and fits (bottom trace) of d_9-**1**-MCM-41 at 283 K (top) and 173 K (bottom).

Fitting the spectra gives QCC parameters of 18.8 kHz and 20.3 kHz for the MCM-41 sample at 283 and 173 K, respectively, and 19.3 kHz at both temperatures for the SBA-15 sample. For all spectra the asymmetry parameter η is small (i.e. less than 0.05). The line shape can be well described by two rotations, one about the methyl groups' C_3 axes and another about the trimethylsilyl group's C_3 axis (see Scheme 3.1). Both of these rotations are fast on the NMR time scale as the averaged QCC values (18-20 kHz) are much smaller than the expected value for the QCC in the absence of motion (~170 kHz).

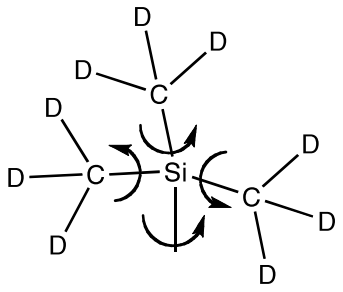

Scheme 3.1. Trimethylsilyl fragment, with C3 symmetry axes denoted.

Also noteworthy for the spectrum of SBA-15 at 175 K is the appearance of a broader feature. This is a Pake doublet with features located at approximately ±20 kHz. This corresponds to a QCC value of 57 kHz. This contribution to the line shape is assigned to a fraction of the trimethylsilyl groups wherein the rotation about the Si-O bond axis is slow on the microsecond time scale. Deconvolution and integration of the fit indicates that the broad component is approximately 10% of the total spectral intensity. One possible explanation for this broad feature is due to TMS groups in the microporoes of the SBA-15 materials as it is not observed in MCM-41. The second component is only observed at temperatures of 175 K and lower.

To probe the dynamic behavior of the materials in more detail, inversion-recovery measurements as a function of temperature were performed on both samples. Figure 3.6 shows a plot of $\ln(1/T_1)$ versus $1/T$ for both samples. More information is given in the Figure A2 and A3 in Appendix A.

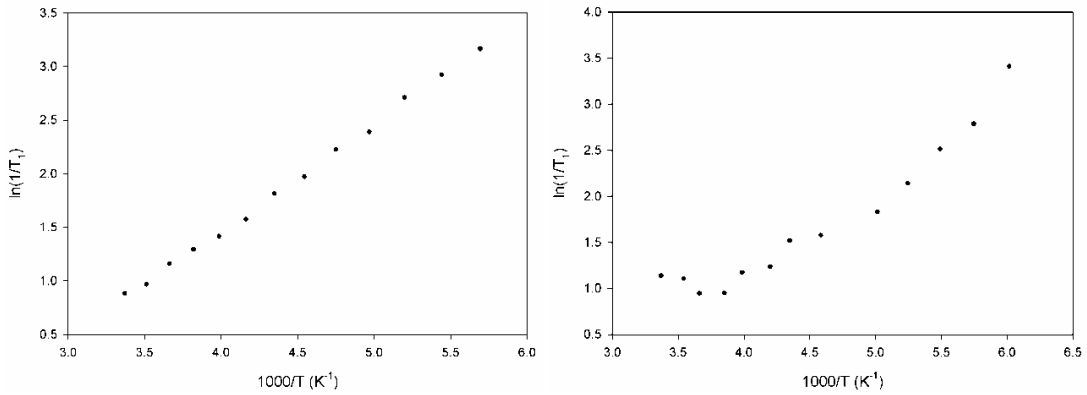

Figure 3.6. Plots of ln($1/T_1$) versus 1000/T for (left) **1**-MCM-41 and (right) **1**-SBA-15.

Using BPP theory from the plot, one can obtain an apparent activation energy for the motions leading to line narrowing [215]. The analysis of the inversion-recovery data is performed using a simple monoexponential decay based on analysis of the data using

$$M(t) = M_o\left(1 - 2e^{\frac{-\tau}{T_1}}\right)$$

multiple complex models (i.e. monoexponential versus biexponential decay), it was concluded no real benefit was obtained from using a more complicated model for describing the inversion-recovery data. From BPP theory the apparent activation energy is related to the slope in the plots above as E_A/R. Based on this analysis, the apparent activation energies for **1**-MCM-41 and **1**-SBA-15 are 6.8 kJ/mol and 8.3 kJ/mol, respectively. For comparison the activation energy of a methyl rotor in trimethylamine in the solid state is approximately 12 kJ/mol [216]. The higher apparent activation energy for SBA-15 sample could be due to TMS groups in the micropores that experience more steric constraint. This is consistent with the low temperature spectrum shown in Figure 3.4, which shows two different groups of deuterons in the SBA-15 sample. The T_1

measurements show subtle, yet real differences between the MCM-41 and SBA-15 samples likely owing to their different pore structures.

3.3.2.2 Magic Angle Spinning (MAS) ^2H NMR of Amine Groups Attached MCM-41

To investigate the dynamics of the tethered amines ^2H magic-angle spinning (MAS) measurements were used instead of the static measurements to improve the signal-to-noise ratio (S/N) of the spectra. Figure 3.7 shows the room temperature static spectrum of **2** at 0.2 mequiv/g loading. First, as can be seen the S/N of the static spectrum is very poor. This motivated the use MAS measurements and higher ligand loading. However, the static spectrum can be fit to a Pake doublet with a QCC value of 58.9 kHz (Figure 3.7) and an asymmetry parameter of $\eta \sim 0$. The line width and shape are qualitatively consistent with the methyl rotor rapidly spinning about its 3-fold symmetry axis.

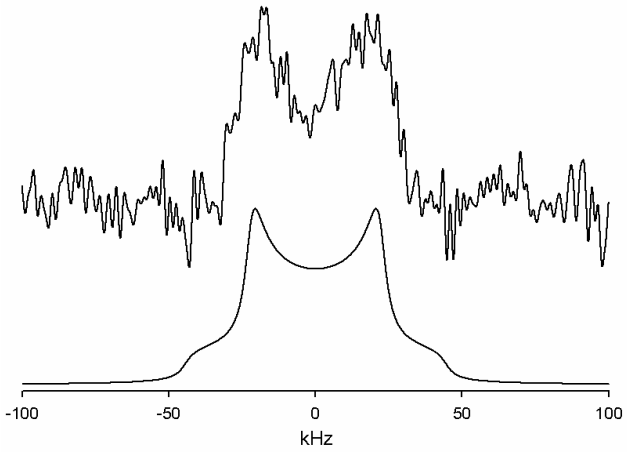

Figure 3.7. Static ^2H NMR spectrum (top) and fit (bottom) of **2** at a loading of 0.2 meq/g.

Figure 3.8 shows the MAS spectra of **2** at a loading of 0.8 meq/g and spin rates of 2, 5, and 10 kHz. Several points are noteworthy. In all three of the spectra the line width is narrower than at the 0.2 meq/g loading. The line narrowing points to an additional motion, which given the differences between Figures 3.7 and 3.8 appears to depend on amine loading. Even in the slow MAS limit (2 kHz) a clear Pake doublet is not observed, but rather an ill-defined envelope of spinning sidebands. Attempts to fit this spectrum lead to a QCC of 31 kHz and a large asymmetry parameter of $\eta = 0.8$. Comparable values were obtained in fitting the spectra at higher spin rates; however, the fit at the lowest spin rate should be the most reliable. Figure 3.9 shows simulated spectra as a function of spinning rate for a QCC of 31 kHz with an asymmetry parameter of 0.8. As can be seen, the simulated spectra at least qualitatively capture the line width and shape. There are some differences in the relative intensities of the spinning sidebands in the center of the spectrum (i.e., ±10kHz range). This could be either due to phasing difficulties (there are nearly 25 sidebands) or that there are multiple components to the line shape which the fitting in Figure 3.8 and simulations shown in Figure 3.9 do not capture.

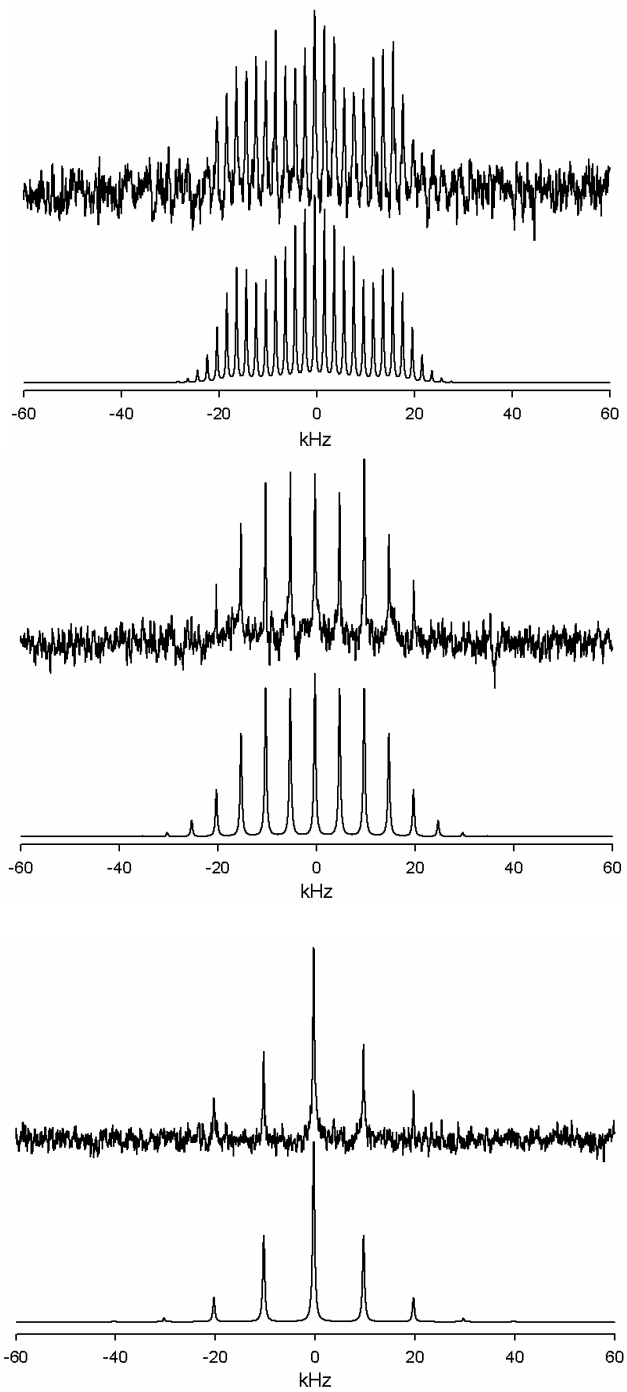

Figure 3.8. (From top to bottom) Static and ^{2}H MAS NMR spectra and fits of **2** at a loading of 0.8 mequiv/g with spinning rates of 2 kHz, 5 kHz, and 10 kHz. In each figure, the upper trace is the spectrum and the lower trace is the fit.

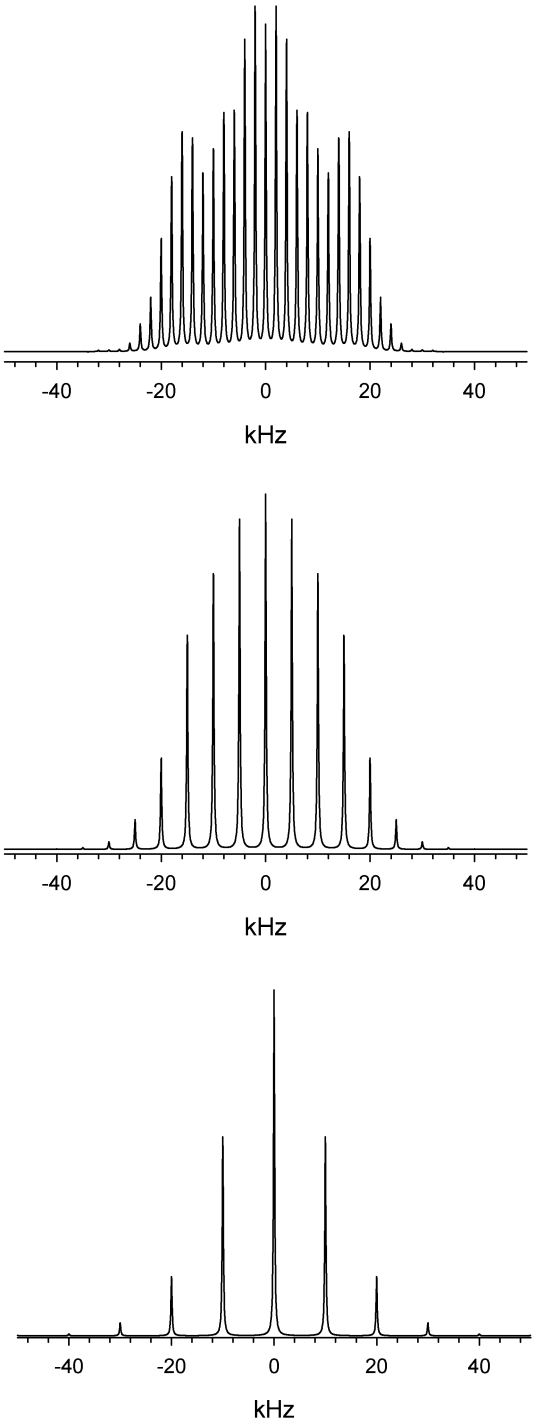

Figure 3.9. Simulated ^{2}H MAS spectra for a QCC value of 31 kHz and an asymmetry parameter of 0.8 as a function of spin rates (from top to bottom, 2 kHz, 5 kHz, 10 kHz).

One possibility to explain the line narrowing could be a slow bending motion (see Scheme 3.2) of the propyl group. This is qualitatively consistent with the line narrowing observed and the asymmetry in the line shape. A physical reason for this could be that the methylamine group is hydrogen bonding with the surface silanols. Consistent with this possibility, spectra of HMDS-**2** (Figure 3.10) show no change in the line shape but a significant increase in the signal-to-noise ratio, indicating that more of the deuterons are contributing to the spectrum for the HMDS treated sample. Finally, it should also be noted that in all MAS measurements the signal-to-noise ratio is poor. For instance, the spectrum shown in Figure 3.8 at a spin rate of 2 kHz is the sum of 400 000 FIDs.

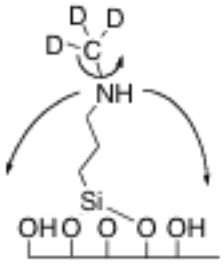

Scheme 3.2. Possible bending mode to explain line narrowing in the presence of MAS.

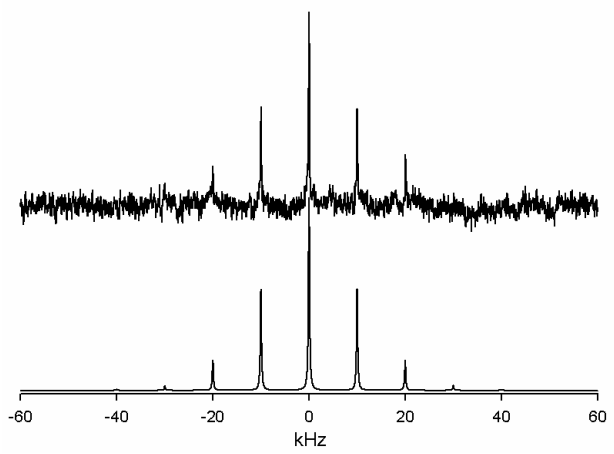

Figure 3.10. The spectrum (upper) and fit (lower) of HMDS-**2**-0.8, and 10 kHz spin rate.

Figure 3.11 (top) shows the ^{2}H MAS NMR spectrum and fit of **3**. In contrast to the *N*-methylpropylamine samples shown above, the spectra are indicative of rigid deuterons. The QCC value determined from the fitting is 160 kHz with a value of zero for the asymmetry parameter, very similar to the expected value for a completely rigid deuteron (QCC ≅ 170 kHz). The QCC value is insensitive to HMDS capping, and the spectrum at a spin rate of 5 kHz is essentially identical to that at 10 kHz (Figure 3.11 (bottom)). The piperazine group is rigid on the microsecond time scale in contrast to the other groups investigated. A way to explain this difference is that the tertiary amine is unable to hydrogen bond with surface silanols, and the piperazine secondary amine cannot interact with the surface due to conformational constraints. This is in contrast the methylamine and benzylamine samples (*vide infra*), where the it seems likely that the secondary amine group interacts with surface silanol groups.

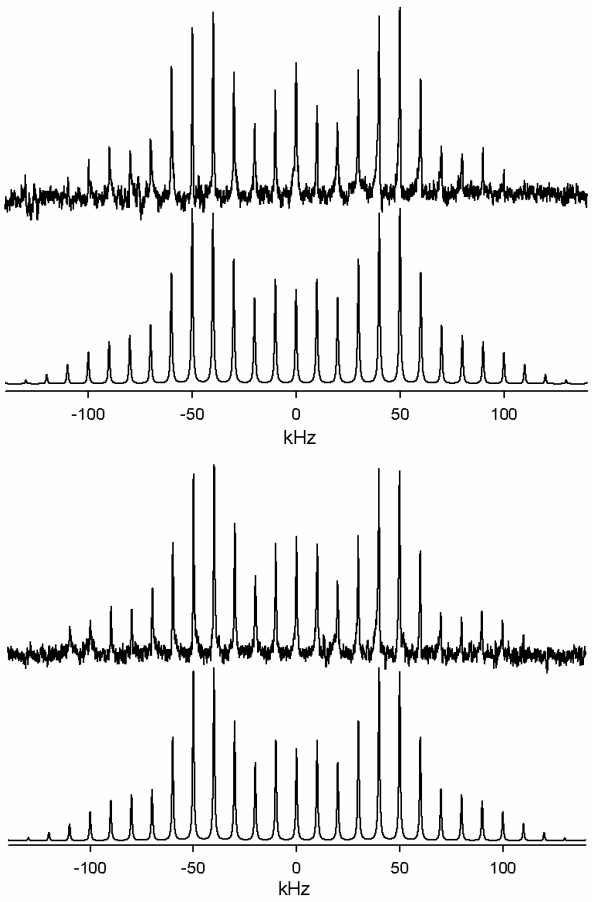

Figure 3.11. ^{2}H MAS NMR spectra (upper trace) and fits (lower trace) of **3** (top) and HMDS-**3**-0.8 (bottom). Spin rate 10 kHz.

Figure 3.12 shows the ^{2}H MAS NMR spectra and fits of **4** at two different spin rates. As can be observed, the manifold of spinning sidebands is much broader in these samples as compared to the methylamine sample **2** shown in Figure 3.7. The spectra of **4** with a spin rate of 5 kHz can be fit with a QCC of approximately 97 kHz and an asymmetry parameter of 0.75. The line shape is triangular in nature; this is likely due to a distribution of motions as is discussed in more detail below. The fitting of the spectrum at a spin rate of 10 kHz gives a QCC value of 88 kHz and an asymmetry parameter of 0.7. These parameters show some variation with the spin rate, but are qualitatively consistent

with fairly rigid deuterons on the microsecond time scale. The line shapes, though narrower, are similar in appearance to a phenyl ring undergoing π-flips, the simulated spectra of which are shown in Figure 3.13. It seems likely that this type of motion is present given the qualitative agreement with the line shape observed experimentally. However, the more triangular nature of the line shape and the additional narrowing observed indicate that additional motions, likely not uniform in nature, are present.

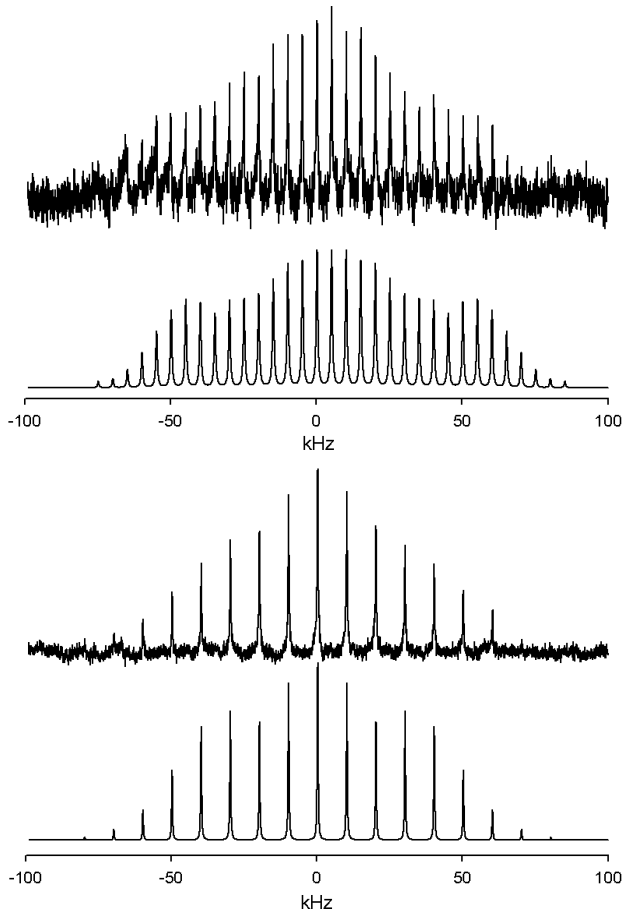

Figure 3.12. ^{2}H MAS NMR spectra (upper traces) and fits (lower traces) of **4** at spin rates of 5 kHz (top) and 10 kHz (bottom).

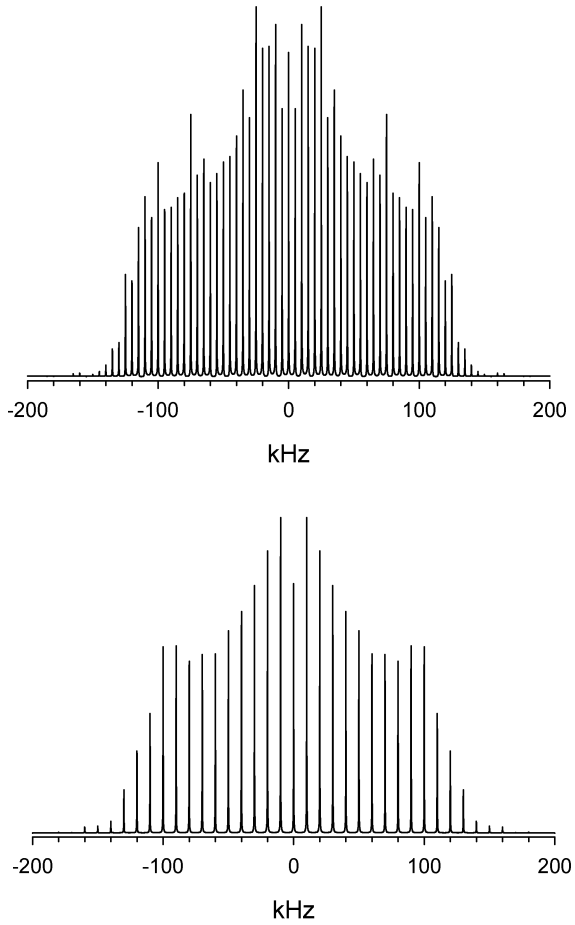

Figure 3.13. Simulated ^{2}H MAS spectra of a deuterated aromatic ring undergoing π-flips about its C_2 symmetry axis with spin rates of (top) 5 kHz and (bottom) 10 kHz.

Upon capping with HMDS (HMDS-**4**) the line width decreases slightly; however, the line shape becomes even more triangular in nature and a pronounced increase in the spectral intensity is observed (Figure 3.14). The fits for these spectra yield QCC values of 65-67 kHz and large asymmetry parameters, 0.6 for the spectrum measured at a spin rate of 5 kHz and 0.7 for the spectrum measured at a spin rate of 10 kHz. A few additional points should be noted. First, the fit of the spectrum measured at 10 kHz is very insensitive to the asymmetry parameter value; i.e., the fit does not change appreciably if the value ranges between 0.7 and 0.9. Further, the fits seemed to indicate that a second

line shape component was needed to adequately reproduce the observed spectrum. We do not believe introducing additional lines with different QCC and η values was warranted given the ambiguous nature of the line shape.

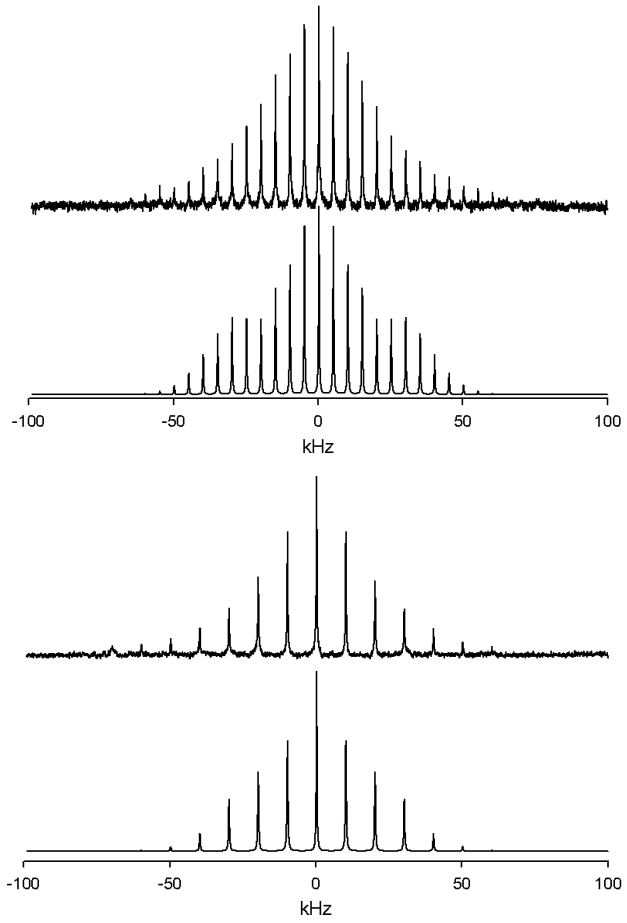

Figure 3.14. ^{2}H MAS NMR spectra (upper traces) and fits (lower traces) of **4**-HMDS at spin rates of 5 kHz (top) and 10 kHz (bottom).

The change in the signal-to-noise ratio for the HMDS capped samples is approximately 4-fold and merits some discussion. One explanation for this change in intensity is that in sample **4** a fraction of the benzylamine groups are engaged in hydrogen bonding with residual surface silanols groups. This could change the rates of

rotation of these fragments: if the motion is on the time scale of the NMR measurement, the signal will be significantly attenuated [217]. Capping the silanols with HMDS should reduce the possibility for the amine hydrogen bonding with the surface. Consistent with that, upon HMDS capping the signal-to-noise ratio (S/N) increases significantly. From at least a qualitative description the spectra are consistent with the phenyl groups undergoing π-flips about their C_2-axis and HMDS capping (i.e., removing the possibility of hydrogen bonding) changes the rates of these motions and the number of deuterons that effectively contribute to the observed spectrum as based on the improvement in the S/N upon capping.

3.4 Conclusions

This chapter describes the rotational dynamics of several simple functional groups on the surface of MCM-41 and SBA-15. The trimethylsilyl groups resulting from HMDS capping rotate rapidly at both room temperature and reduced temperatreus. Interestingly, clear differences at low temperatures can be observed as the TMS groups likely in the SBA-15 micropores exhibit more rotational restraint. The piperazine groups covalently attached to MCM-41 appear rigid on the microsecond time scale, whereas the methylamine and benzylamine groups display some level of rotational mobility. For the latter two samples the dynamics do appear dependent on the presence of surface silanol groups, as the signal intensity increases when the majority of the silanol groups are capped with HMDS. This implies that these amines interact with the surface silanol groups, likely via hydrogen bonding. This is physically reasonable, and this type of

cooperativity has in fact been invoked to explain the observed catalytic properties of amines attached to OMS [85, 91].

CHAPTER IV

NITROALDOL REACTIONS CATALYZED BY AMINE-MCM-41 HYBRIDS *

4.1 Introduction

In this chapter, the catalytic properties of materials described in Chapter III are reported. In details, the effects of amine type (primary, secondary, tertiary amines), loading, surface hydrophobicity, and solid supports on the structure, porosity, and catalytic properties of these hybrid materials are reported. The materials were characterized by X-ray diffraction, nitrogen adsorption isotherms, thermogravimetric analysis. Their catalytic properties are discussed based on their application in the nitroaldol (Henry) reaction.

4.2 Experimental

MCM-41 and SBA-15 were synthesized and calcined as described above. Amine-functionalized MCM-41 samples were prepared using post-synthetic grafting. Three different loadings were used: 0.2, 0.4, 0.8 mmol amine per gram SiO_2. *N*-(methylaminopropyl)trimethoxysilane, *N,N*-(dimethylaminopropyl)trimethoxysilane,

---

* Reprinted with permission from "Nitroaldol reactions catalyzed by amine-MCM-41 hybrids" by Q. Wang, D. F. Shantz, J. Catal. 271 (2010) 170-177. © 2010 Elsevier Inc.

APTES, or chloropropyltriethoxysilane were used as silane sources with functional amine groups to prepare *N*-Methylpropylamine (**2**), *N,N*-dimethylpropylamine (**5**), propylamine, and chloro- functionalized MCM-41, respectively. *1-propyl piperazine MCM-41* (**3**) and *1-propyl piperidine MCM-41* (**6**) were synthesized based on the reaction of piperazine or piperidine with chloro-functionalized MCM-41. *N-propyl-N-benzylamine MCM-41* (**4**) was obtained from the reaction of propylamine-functionalized MCM-41 with benzyl bromide. Amine functionalized SBA-15 was prepared to compare the effects of the substrate on the catalytic properties with those based on MCM-41. Trimethylsilyl groups were introduced to the amine-functionalized OMS surface in order to cap the residue silanol groups. This was done to assure the effects of the silanol groups on their reactivity in the Nitroaldol reaction. Detailed synthesis procedures and the designated numbers for these samples can be found in Chapter II. Scheme 4.1 includes the schematic procedures of synthesis with all ligands used here. This chapter will mainly present the results and discussions.

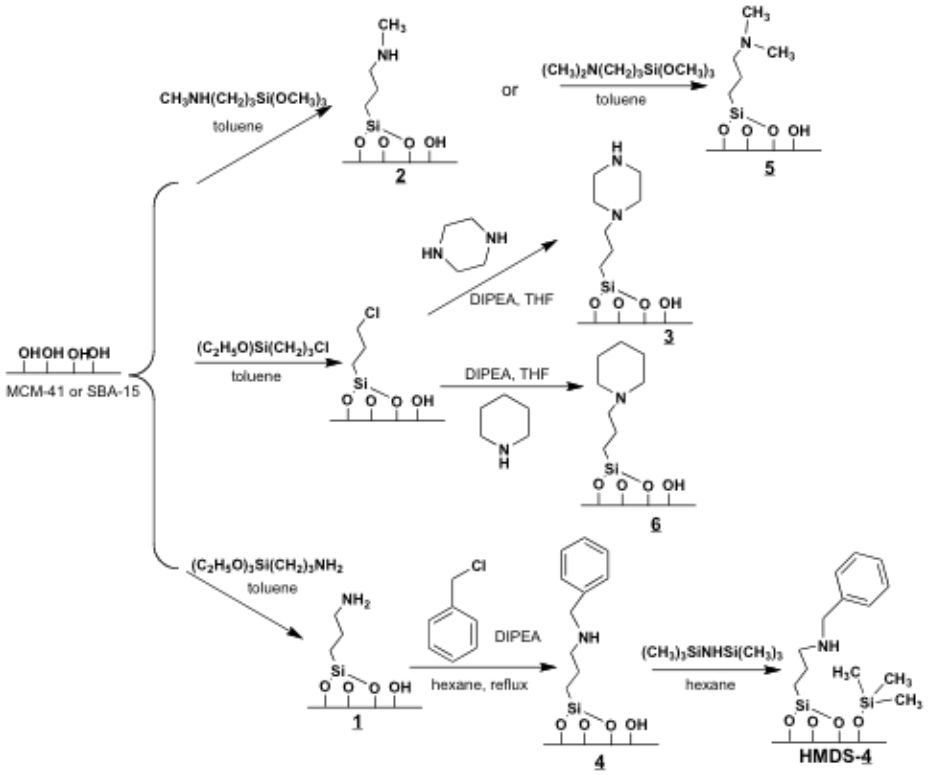

Scheme 4.1. Synthesis of functionalized MCM-41 and SBA-15.

4.3 Results

4.3.1 General Characterization

Figure 4.1 shows the powder X-ray diffraction patterns, adsorption isotherms, and BJH pore size distributions for MCM-41, **1**-MCM-41, **4**-MCM-41 (0.8 mmol/g loading), and HMDS- **4**-MCM-41. The XRD results are consistent with literature results and indicate the target OMS phase is obtained. The parent MCM-41 as prepared shows well ordered structure and the pore channel is hexagonal phase. With the loadings of organic amines on the surface, the XRD patterns display that the structures of amine functionalized MCM-41 without obvious changes. The nitrogen adsorption isotherms

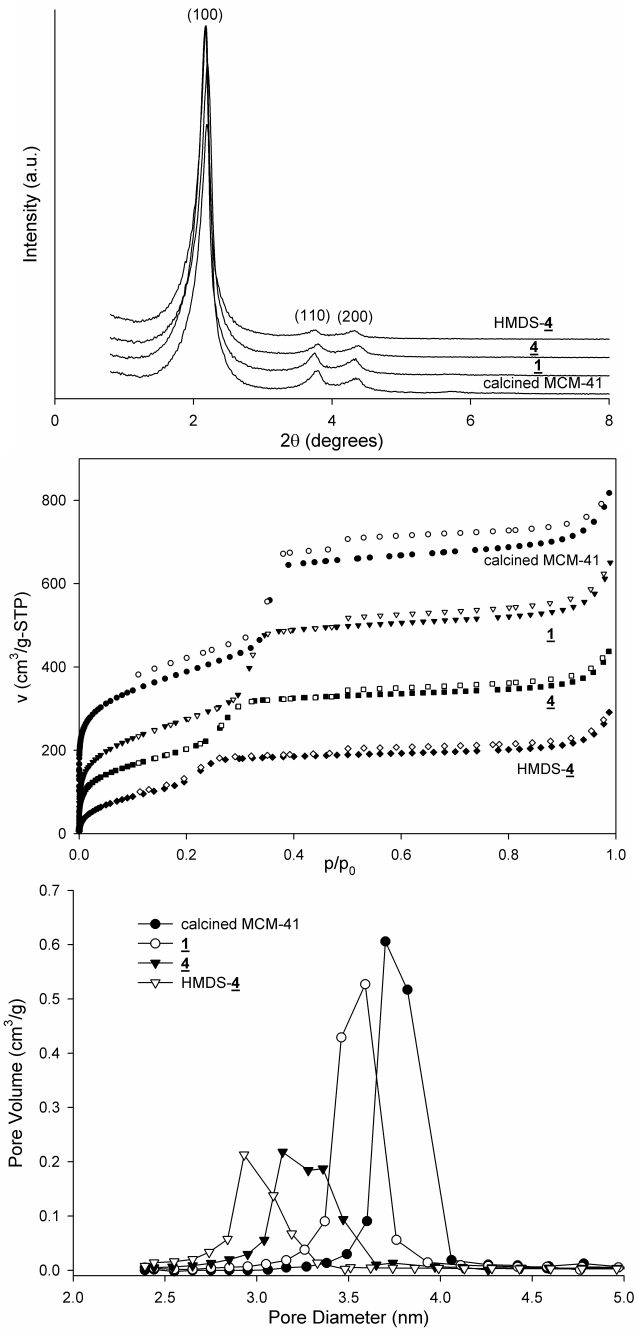

Figure 4.1. (From top to bottom) Powder X-ray diffraction patterns, nitrogen adsorption isotherms, and BJH pore size distributions for MCM-41, **1**-MCM-41, **4**-MCM-41, and HMDS-**4**-MCM-41. The isotherm of MCM-41 has been shifted 100 cm^3/g-STP.

show that the mesopore volume and effective pore size decrease gradually with the increase of organic group loading. The isotherms of the other samples can be found in

Chapter III. Table 4.1 shows the organic content as determined from thermal gravimetric analysis (TGA) and elemental analysis.

Table 4.1. Percent conversions at one hour and two hours, product selectivities, actual amine loadings (determined by TGA) and TOF values. Amine loadings in mmol/g.

Sample ID	time (h)	*X(%)*	S_{OH}	$S_{=}$	*Amine loading*	*TOF* (h^{-1})
1-MCM-41-0.8	1	22	0.31	0.69	0.70	7.7
	2	45	0.31	0.69		
1-MCM-41-0.4	1	13	0.23	0.77	0.49	4.3
	2	22	0.38	0.62		
2-MCM-41-0.8	1	97	0.98	0.02	0.88	74.0
2-MCM-41-0.2	1	54	0.9	0.1	0.31	50.3
3-MCM-41-0.8	1	36	0.99	0.01	0.76	12.4
	2	56	0.98	0.02		
3-MCM-41-0.4	1	24	0.93	0.07	0.50	12.3
	2	37	0.92	0.08		
3-MCM-41-0.2	1	26	0.94	0.06	0.38	17.7
	2	41	0.94	0.06		
4-MCM-41-0.8	1	62	0.90	0.10	0.66	24.4
	2	89	0.85	0.15		
4-MCM-41-0.4	1	25	0.83	0.17	0.41	14.7
	2	44	0.80	0.20		
4-MCM-41-0.2	1	15	0.85	0.15	0.34	10.9
	2	31	0.82	0.18		
5-MCM-41-0.8	1	95	0.99	0.01	0.74	55.4
	2	98	0.99	0.01		
6-MCM-41-0.2	1	68	0.91	0.09	0.32	64
	2	86	0.93	0.07		

4.3.2 Catalytic Testing

4.3.2.1 Effect of Amine Loading and Identity

All samples were investigated for the ability to catalyze the nitroaldol reaction, as shown in Scheme 4.2. The parent (i.e. amine-free) MCM-41 silica is completely inert and thus the catalytic activity observed is due to the amines attached on the OMS surface.

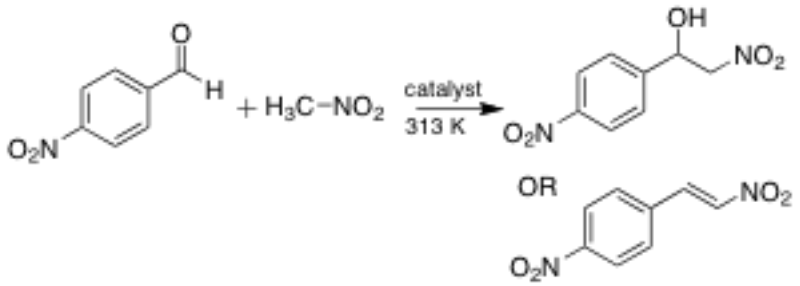

Scheme 4.2. Nitroaldol reaction (Henry reaction) at 313 K.

Table 4.1 summarizes the catalytic data, including the percent total conversion of the nitrobenzaldehyde, product selectivities and the turnover frequency (initial number of reaction events h^{-1} amine $site^{-1}$) where the number of amines was estimated by elemental analysis and TGA. From Table 4.1, some general conclusions can be drawn. The propyl amine sample (**1**) is the least active. That the secondary amines are more active is consistent with previous work [165, 166]. Also consistent with previous literature the product selectivity is dependent on the nature of the amine (i.e. primary versus secondary, tertiary). The primary amine sample (**1**) appears to follow the imine formation mechanism which favors the nitrostyrene product, consistent with the reports by Bass and coworkers lab.[91] In contrast the samples containing secondary amines give very high selectivities, between 0.8 and 0.9, to the nitroalcohol product. Also noteworthy is that the selectivity to the nitroalcohol product increases with increasing amine loading. Finally, the selectivities also show differences that can likely be attributed to the structures of the different secondary amines, as will be discussed in detail in the following paragraphs. It is also important to note that the Supplementary material contains plots of the selectivities versus time for all samples. We do not observe any significant interconversion of alcohol to alkene via dehydration or hydrolysis of alkene to alcohol.

This conclusion is based on the observation that the selectivities are essentially constant during the reactions.

4.3.2.2 Effect of the Amine Identity

Figure 4.2 shows the conversions and yields of the Henry reaction catalyzed by propyl amine functionalized MCM-41, **1**-MCM-41 sample. This is the one sample where

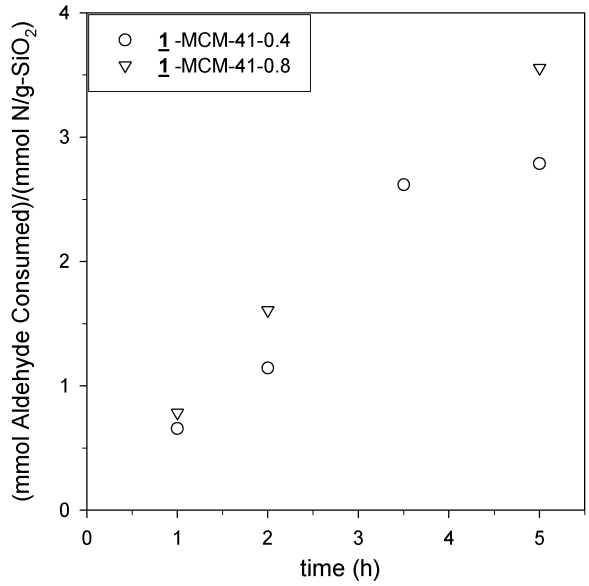

Figure 4.2. Nitrobenzaldehyde consumption normalized by the mmol of nitrogen per gram of silica versus reaction time for **1**-MCM-41 as a function of amine loading.

the alkene product is dominant; the selectivity to the alcohol product is low (0.3). The TOF is low (7 h^{-1}) relative to the other materials investigated. Previous literature reports of similar materials in the Henry reaction [91, 169] at comparable reaction conditions give TOFs of 12 h^{-1} with selectivity to the alcohol product of 20%.

The results for **2**-MCM-41 are shown in Figure 4.3. The differences between these samples and the simple propylamine-functionalized MCM-41 are striking. Both the activity and selectivity of this material are different. The conversions are much higher than for the samples of **1** and the selectivity is very high (> 0.9) to the nitroalcohol product. The samples with target loadings of 0.8 mmol/g and 0.2 mmol/g give conversions of 97% and 57%, respectively after one hour. Note that the data shown in Figure 4.3 for the high loading sample used an initial amount of 7.5 mmol of benzaldehyde. The other data were collected by the reactions of 2.5 mmol of benzaldehyde as shown in Chapter II. The selectivity to alcohol product is over 90%. In order to calculate the initial TOF of the 0.8 mmol/g sample, three times the reactant described in the experimental section (i.e. 7.5 mmol of aldehyde) was used to measure conversions at short times. The TOFs (50 h^{-1} and 74 h^{-1} for 0.2 mmol/g and 0.8 mmol/g loading samples, respectively) shown in Table 4.1 indicate the **2**-MCM-41 samples have the largest reaction rate among the three secondary amine functionalized MCM-41 samples. One explanation is that the methylpropyl amine group facilitates the formation of an ion-pair, another that the least sterically hindered secondary amine should be the most active.

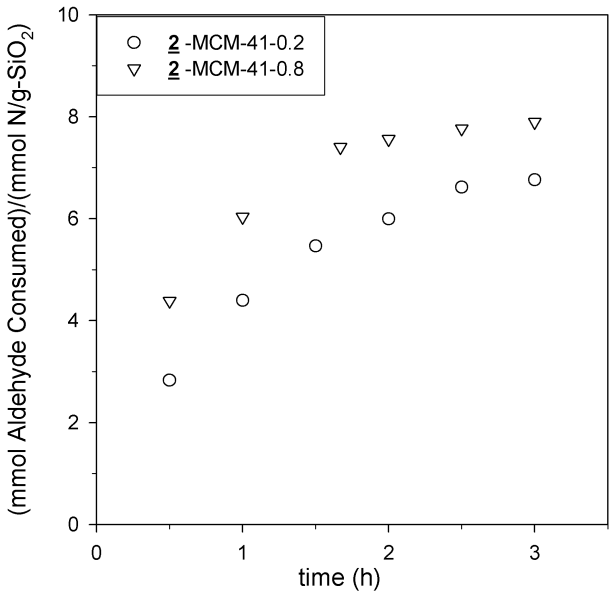

Figure 4.3. Nitrobenzaldehyde consumption normalized by the mmol of nitrogen per gram of silica versus reaction time for **2**-MCM-41 as a function of amine loading.

This result led us to explore other more sterically hindered secondary amines. Piperazine functionalized MCM-41 samples (**3**-MCM-41) were also investigated. These materials (Figure 4.4) displayed an even higher selectivity to the alcohol, above 0.9 in all cases. It is also observed that with increased amine loading, the amount of nitroalkene formed decreases, going to essentially zero for the highest loading samples. In contrast to the previous two samples, here we clearly see that the lowest loading sample appears to have the highest activity on a per site basis. Consistent with that the TOF is largest for the lowest loading sample and the values are 17.7, 12.3, and 12.4 h^{-1} for 0.38 mmol/g (0.2 target), 0.5 mmol/g (0.4 target), and 0.76 mmol/g (0.8 target) loading samples, respectively. One difference between this and the previous samples is that the steric bulk of this ligand is much larger. Related to this, the fact that the amine is in a more rigid cyclic structure may negatively impact its activity. Also, it is possible that at higher

loading, there are more ligand-ligand interactions that lead to reduced activity. Clearly, the absolute activity of these samples is much lower than the *N*-methylamine samples (**2**). Initially, it was anticipated that the tertiary amine in the piperazine ring does not contribute to the observed activity due to steric effects. This was assessed directly based on ligand **6** discussed later. We believe one explanation for the low amount of alkene formed is that the piperazine secondary amine is far enough from the surface that there are likely minimal interactions between it and the surface silanol groups. The low amount of alkene formed is also consistent with work from Asefa's laboratory [169].

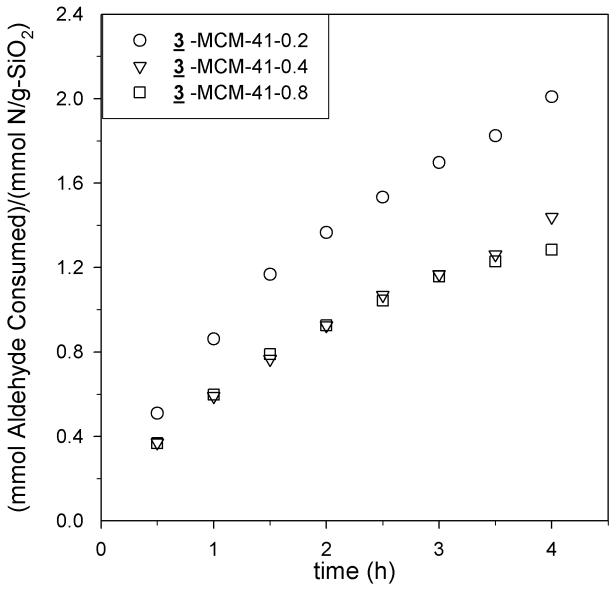

Figure 4.4. Nitrobenzaldehyde consumption normalized by the mmol of nitrogen per gram of silica versus reaction time for **3**-MCM-41 as a function of amine loading.

Figure 4.5 shows the conversions and product yields for the **4**-MCM-41 samples as a function of reaction time. As can be seen from Table 4.1, the nitroalcohol is the major product and the alcohol selectivity ranges from 0.7 to 0.9. Also, the conversion is seen to increase with increasing amine loading. At thirty minutes, the respective

conversions are 7%, 13%, and 40% for **4** at loadings of 0.2, 0.4, and 0.8 meq/g, respectively. The 0.8 meq/g sample shows an approximately threefold increase in conversion compared to the 0.4 meq/g sample. For the **4**-MCM-41 samples, the TOF decreases from 24 h^{-1} for 0.8 mmol/g, 15 h^{-1} for 0.4 mmol/g, and 11 h^{-1} for 0.2 mmol/g. That the TOF (initial number of reaction events h^{-1} amine $site^{-1}$) is strongly dependent on the amine loading shows these do not behave as site-isolated materials. One explanation for the observed behavior is that there is cooperativity between the amines and/or silanol groups. In contrast to the other secondary amines more alkene product is observed in this

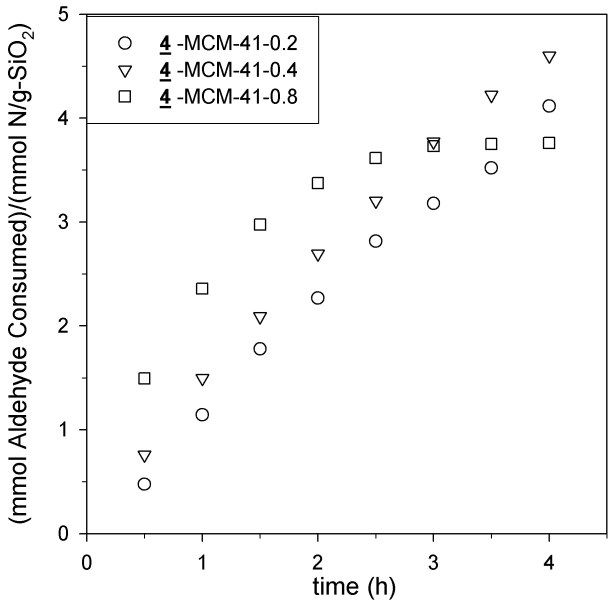

Figure 4.5. Nitrobenzaldehyde consumption normalized by the mmol of nitrogen per gram of silica versus reaction time for **4**-MCM-41 as a function of amine loading.

system. Also the amount of alkene appears to increase slightly as the reaction proceeds, in contrast to the other two secondary amines investigated. This could be either due to stronger amine – surface silanol interactions in this system, or because the pK of thebenzylamine should be lower than that of the methylamine and piperazine due to the substituent aromatic group.

Figure 4.6 shows the consumption of nitro-benzaldehyde catalyzed by tertiary amine-functionalized MCM-41 samples. The **5**-MCM-41 sample (dimethylamine) shows similar conversions and product selectivities to that of **2**-MCM-41. After one hour the conversion is 96% and the selectivity to alcohol product is 0.99. The **6**-MCM-41 sample with 0.2 meq/g loading displays 65% conversion after one hour, higher than that of the **3**-MCM-41 sample. The results indicate that the catalytic activity is dependent on the basic strength of the functional amine groups attached on MCM-41 as well as the steric structures surrounding the amines.

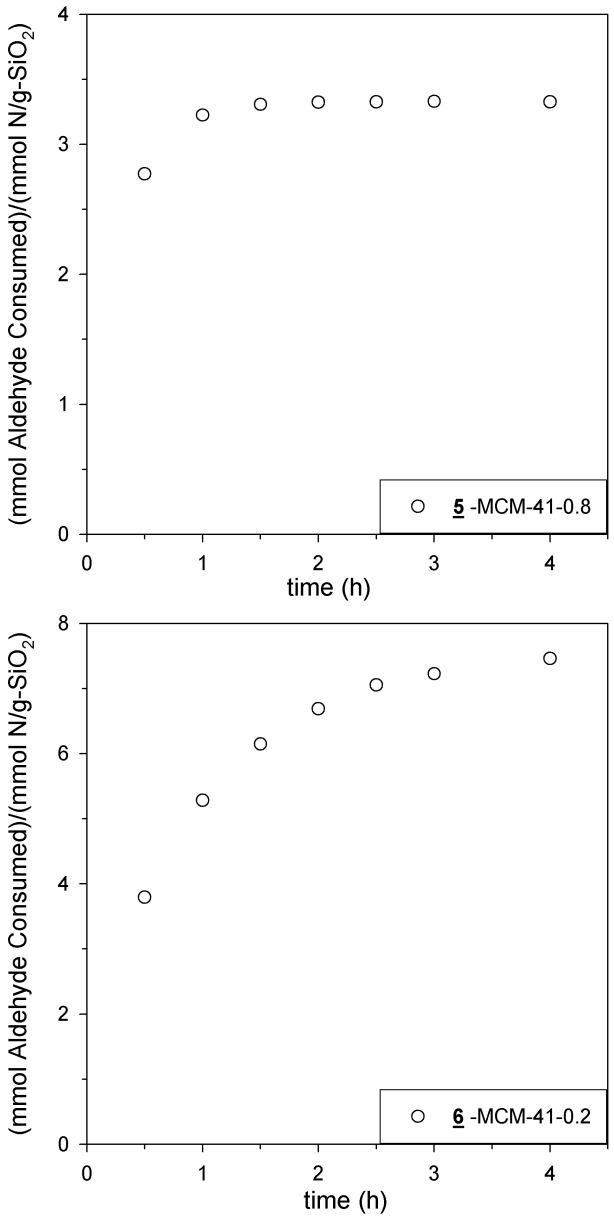

Figure 4.6. Nitrobenzaldehyde consumption normalized by the mmol of nitrogen per gram of silica for **5**-MCM-41 with 0.8 meq/g loading (top) and **6**-MCM-41 with 0.2 meq/g loading (bottom).

Based on the above-mentioned results, it would seem two key features affect the reactivity of the supported amines. The first is that non-cyclic amines appear to be more active than the cyclic amines. This is based on comparing the reactivity of the benzylamine and piperazine-functionalized silanes with the methyl and dimethylamine-functionalized silanes. It also appears that moving the amine farther from the surface has a negative effect on reactivity based on comparing the piperidine and piperazine substituted silanes.

4.3.2.3 Effect of Hexamethyldisilazane Capping

Previous work by Bass and co-workers [91, 218] has shown that cooperativity by hydrogen bonding between the amine and silanol groups is possible in these materials. The above-mentioned work has also shown very clear differences in reactivity amongst several different secondary amines. To attempt to understand how the silanols affect the activity observed the samples discussed earlier were treated with hexamethyldisilazane (HMDS) to convert the surface silanol groups into trimethylsilyl moieties [219]. Figure 4.7 shows the aldehyde consumption versus time for these materials. With the exception of the samples of **2**-0.8 capped with HMDS, all samples show a dramatic reduction in activity, with conversions at 6 hours below 20% in all cases. There are three ways this result can be interpreted. The first is that the high catalytic efficiency depends on the cooperative activation of reactants by the amines and the silanols. The second is that the bulk of the TMS fragment reduces access to the amine and thus suppresses reactivity. To probe this a sample of **4** was treated with methyltrimethoxysilane, which should react with the silanol groups yet is much smaller. As can be seen in Figure 4.8, the reaction rate

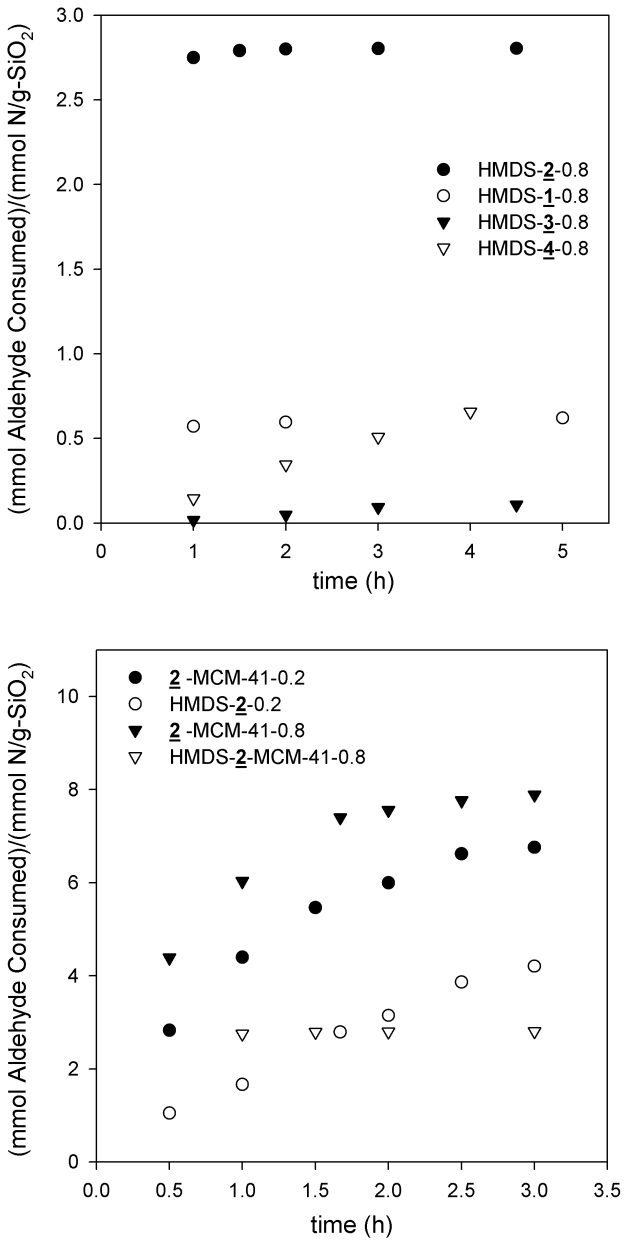

Figure 4.7. Nitrobenzaldehyde consumption normalized by the mmol of nitrogen per gram of silica for several HMDS-capped samples.

is much lower upon capping with methyltrimethoxysilane and the conversion is linear with time. The calculated TOF decreases from 24.2 h^{-1} to 6.3 h^{-1}. This result is certainly consistent with the first point above (cooperativity between silanols and amines). The

third possibility is that capping the surface silanols made the materials so hydrophobic that the reagents would not adsorb into the material. This seems unlikely as the powders after HMDS capping still wet readily. One possible explanation for the high activity of **2**-0.8 capped with HMDS sample is that the silane chemistry is relatively incomplete. In order to check if that is the case, a sample of **2** with a lower amine loading (0.2 mmol/g) was capped with HMDS. After HMDS treatment, the conversion did decrease significantly, although the sample is still much more active than the other HMDS-capped samples. A simple conclusion is that the presence of silanols are not as essential for the methylamine groups to perform this chemistry as it is the most active ligand investigated.

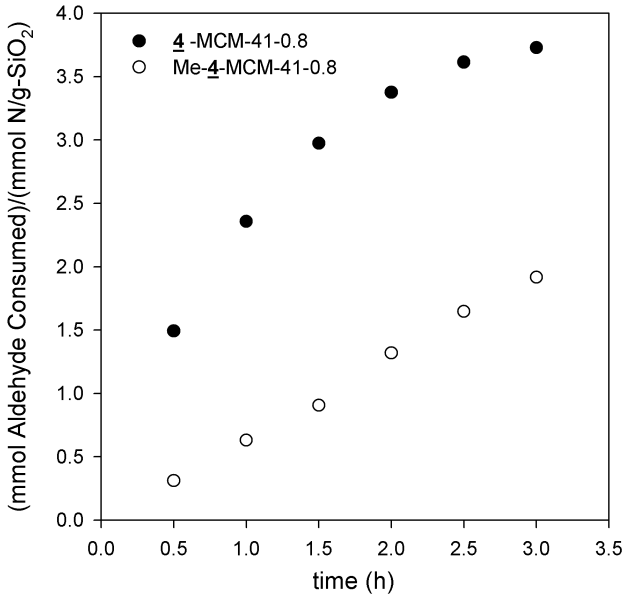

Figure 4.8. Nitrobenzaldehyde consumption normalized by the mmol of nitrogen per gram of silica for **4**-MCM-41 and a sample of **4**-MCM-41 treated with methyltrimethoxysilane.

4.3.2.4 Catalyst Stability

In order to check the stability of the materials, samples of **4** were recycled and the data are shown in Figure 4.9. The reaction rate decreases for the 2nd testing cycle, but appears stable in subsequent recycle measurements. The conversion after two hours is still higher than 50% and a similar selectivity to nitroalcohol product was observed as in the initial run. The decrease in conversion is possibly due to the incomplete removal of absorbed species from the active sites by nitromethane and methanol. Ongoing work is investigating this issue in more detail. As a whole, the benzylamine-MCM-41 displayed relatively stable catalytic activity and selectivity.

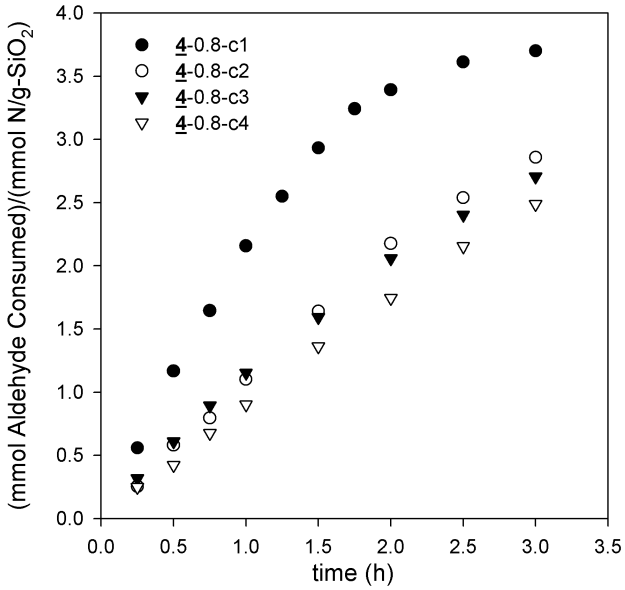

Figure 4.9. Recycle data for **4**-MCM-41 (0.8 meq/g).

4.3.2.5 Effect of Substrate

Figure 4.10 shows the conversion of nitrobenzaldehyde catalyzed by 0.8 mmol/g **4** attached on SBA-15. The total conversion is much lower than that catalyzed by *N*-

benzylpropylamine functionalized MCM-41. There are several possible explanations for the observed behavior. First, the smaller pore size of MCM-41 (3.8 nm) could lead to stronger adsorption of the reactants and perhaps lead to enhanced reaction rates. We have no direct evidence for this beyond the marked decrease in activity for the ligand supported on SBA-15 (7.8 nm). Another possibility is that due to the micropores in SBA-15 some of the grafted amines preferentially attach in / near the micropores and are thus inaccessible. This could explain some, but likely not all the decrease in activity observed. The TGA data does show a lower amine loading on SBA-15 (0.46 mmol/g silica) than expected. Finally, given the lower surface area of SBA-15 there will be statistically fewer silanol groups at a given amine loading. While we cannot eliminate one over any other, all three of these possibilities could contribute to the reduced activity observed.

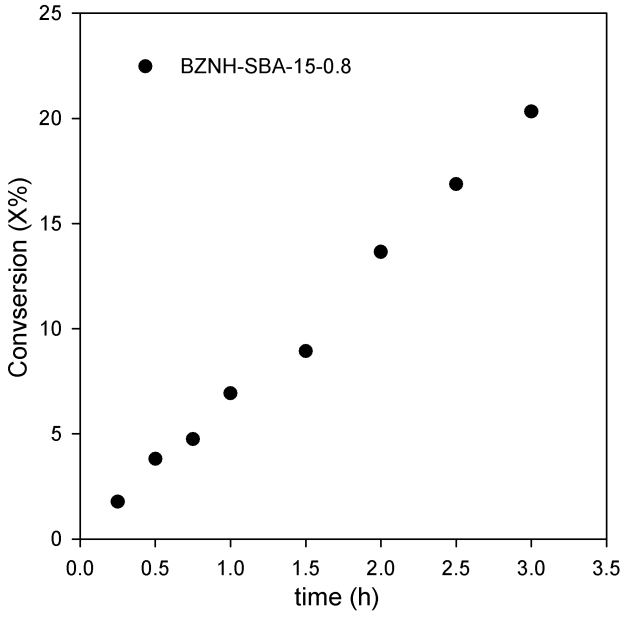

Figure 4.10. Nitrobenzaldehyde conversion of silica for **4**-SBA-15.

4.4 Conclusions

The effects of amine identity, structure, loading, presence of surface silanols, and the substrate topology on the Henry reaction have been investigated. Consistent with previous results, primary amines favor the formation of the alkene product, while secondary and tertiary amines favor the formation of the alcohol products. Among the secondary amines, the least sterically hindered amine (*N*-methylamine) was the most active. In nearly all samples, the capping of the silanol groups with hexamethyldisilazane dramatically decreased the activity of the materials, implying the need for cooperativity between the surface amine and silanol groups. There are also clear support effects as the benzylamine ligand was much more active when grafted to MCM-41 when compared to SBA-15.

CHAPTER V

CATALYTIC PROPERTIES OF DENDRON-OMS HYBRIDS*

5.1 Introduction

The fabrication of OMS hybrid materials with high densities of organic functional groups is difficult in the sense that the distribution of catalytically active sites often becomes heterogeneous. Our group has reported the immobilization of melamine-based dendrimers on the surfaces of amine-functionalized SBA-15 materials [136-138]. The current investigation in this chapter, building off our previous reports [136-138], describes the synthesis and catalytic testing of these materials in the Henry (nitroaldol) reaction, the synthesis of methyl esters from triglycerides, and the cross aldol reaction between acetone and 5-hydroxymethylfurfural.

5.2 Experimental

MCM-41 and SBA-15 were synthesized and calcined as described above, and used as the solid supports for post-synthetic grafting of two kinds of polyamine dendrons. Cyanuric chloride (CC) was used as the branching molecule, and piperazine (PIP) or 4 (Aminomethyl)piperidine (AMP) was used as the diamine. For clarity, samples with dendrons made using 4-(aminomethyl)piperidine as the diamine linker are denoted as G**x**

---

* Reprinted with permission from "Catalytic properties of dendron-OMS hybrids" by Q. Wang, V. V. Guerrero, A. Ghosh, S. Yeu, J. D. Lunn, D. F. Shantz, J. Catal. 269 (2010) 15-25.

AMP dendrons, and samples with dendrons made using piperazine as the diamines linker are denoted as G**x** PIP dendrons where **x** is the dendron generation. Scheme 5.1 shows the procedure of dendron synthesis from OMS surface illustrated with PIP, by repeating step 1) and 2), up to three generations of dendrons were grafted on the OMS pore channels. The hybrid materials were used as base catalysts in three kinds of catalytic reactions, the nitroaldol reaction of nitrobenzaldehyde and nitromethane, the transesterification reaction of glyceryl tributyrate with methanol, and the aldol condensation of 5-hydroxymethylfurfural (HMF) with acetone. The scheme of the reactions and the proton chemical shifts of the product were introduced in Scheme 5.2 and 5.3. Detailed synthesis procedures and the scheme of the reactions can be found in Chapter II.

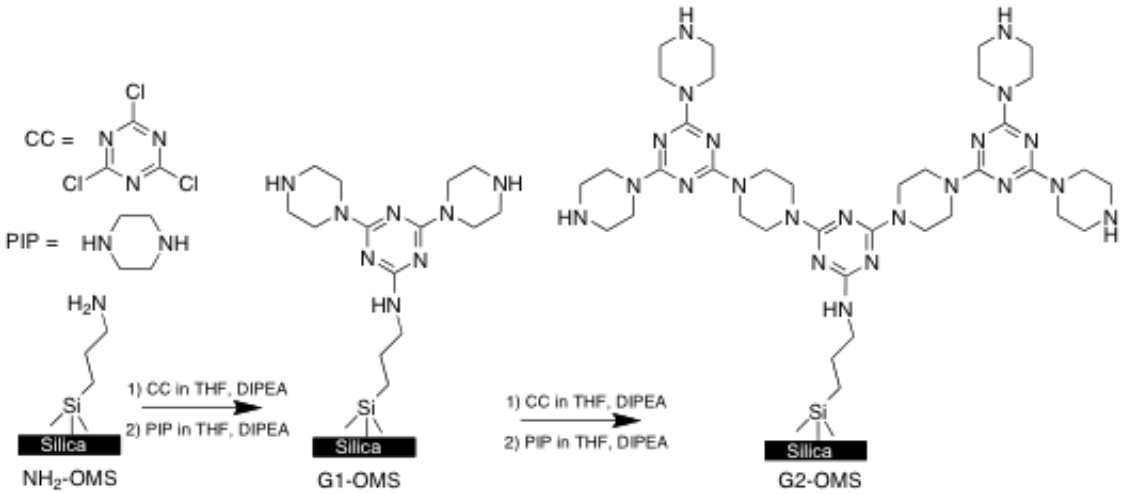

Scheme 5.1. Dendron synthesis from OMS surface illustrated with PIP.

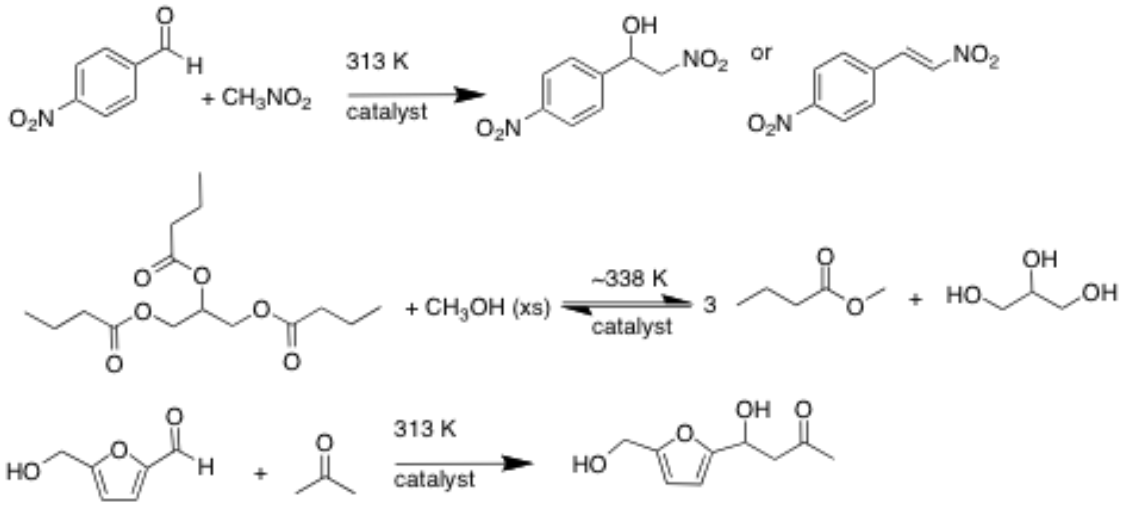

Scheme 5.2. Reactions investigated in the current work. From top to bottom: Henry reaction, methyl ester synthesis from triglycerides, and Aldol condensation of 5-(hydroxymethyl)furfural (HMF) with acetone.

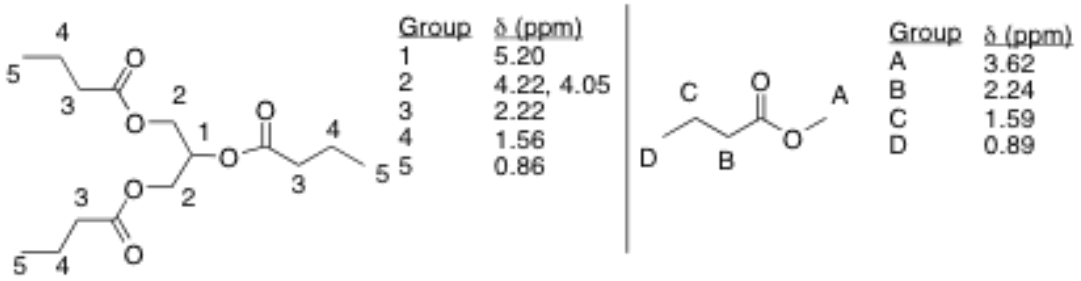

Group	δ (ppm)
1	5.20
2	4.22, 4.05
3	2.22
4	1.56
5	0.86

Group	δ (ppm)
A	3.62
B	2.24
C	1.59
D	0.89

Scheme 5.3. Molecular structures of GTB and the methyl ester product, and chemical shifts of the different protons as determined by ^{1}H NMR.

The catalytic data presented for the Henry reaction and transesterification reaction are presented as both absolute conversion of reactant and amount of substrate consumer (or product formed) per mmol of nitrogen per gram of silica. The latter is an attempt to normalize the reactivity data to an effective mmol of amine basis, as the different samples have different amine contents.

5.3 Results and Discussions

5.3.1 Hybrid Characterization

Figure 5.1 shows the powder XRD patterns of representative parent MCM-41 and SBA-15 materials used in all subsequent work. As can be observed the syntheses lead to highly ordered OMS materials. In the case of the MCM-41 samples four reflections are clearly observed and the fifth is weakly visible. For the SBA-15 materials there are three reflections. The PXRD patterns of all samples are included in Figure 5.2. Consistent with previous work the higher order reflections become weaker as the organic content of the hyrbid material increases and no appreciable change in the peak positions is observed. The PXRD results show the parent materials are well-defined MCM-41 and SBA-15 materials.

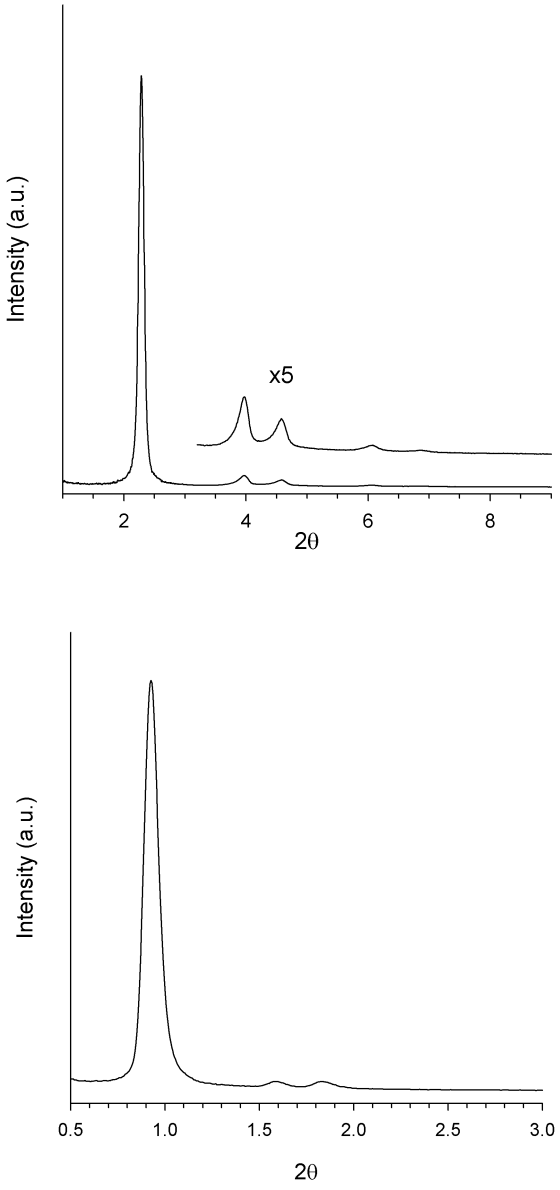

Figure 5.1. PXRD patterns of (top) MCM-41 and (bottom) SBA-15.

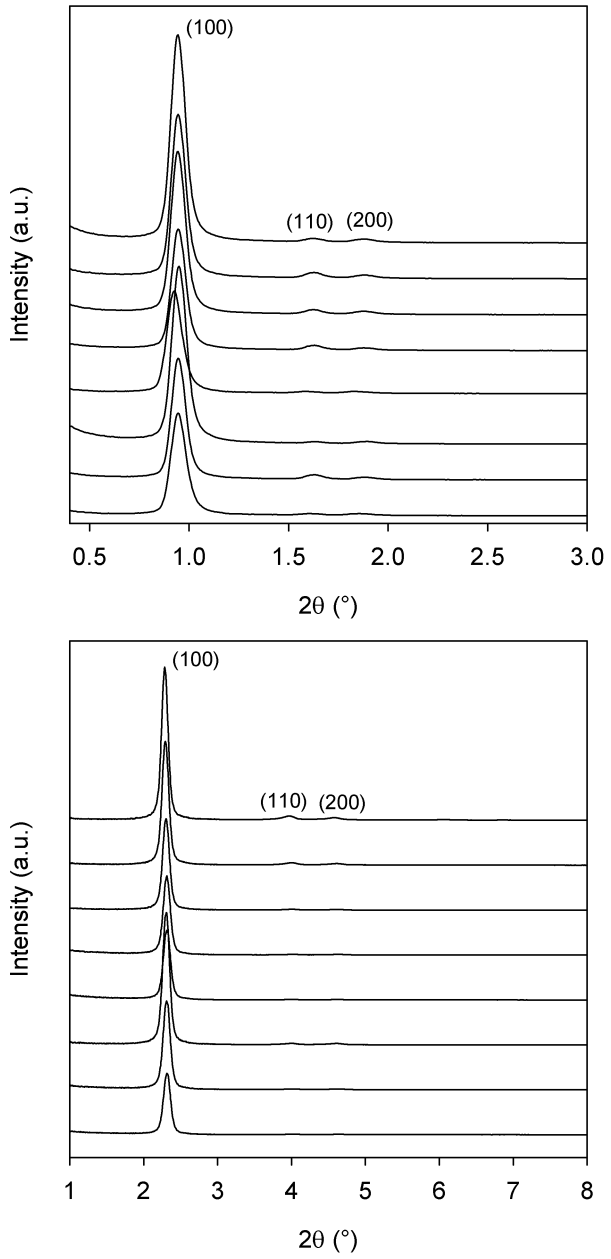

Figure 5.2. Powder diffraction patterns: (top) (from top to bottom) of SBA-15, amine-SBA-15, G1-AMP SBA-15, G1-PIP SBA-15, G2-AMP SBA-15, G2-PIP SBA-15, G3-AMP SBA-15, G3-PIP SBA-15; (bottom) (from top to bottom) of MCM-41, amine-MCM-41, G1-AMP MCM-41, G1-PIP MCM-41, G2-AMP MCM-41, G2-PIP MCM-41, G3-AMP MCM-41, G3-PIP MCM-41.

Nitrogen adsorption was used to quantify the change in porosity of all samples. The adsorption isotherms of the parent OMS materials are shown in Figure 5.3 and data for all of the samples are summarized in Table 5.1. The nominal pore sizes of the parent MCM-41 and SBA-15 are 3.5 and 7.8 nm, respectively. Several observations can be made from the data summarized in Table 5.1. First, in the case of the AMP-MCM-41 samples it appears that for both dendrons investigated that the resulting G2 and G3 hybrids are non-porous, at least based on nitrogen porosimetry. Given the relatively small (3.5 nm) pore size of MCM-41 this does not seem entirely unreasonable. The G1-PIP dendron should be modestly smaller as this sample appears to have both a slightly higher surface area and pore volume (~10% larger) than the AMP sample. Also note that while the G2-PIP sample has some porosity based on nitrogen adsorption, the G3 sample does not. The SBA-15 samples on the whole show similar trends to the materials reported previously by our laboratory at low amine loading. However, in contrast to the previous work with a nominal amine loading of 0.5 mmequiv/g [136-138], here we observe a systematic decrease in pore volume from amine functionalized SBA-15 to G1 to G2 samples. The pore sizes, as manifested by the position and width of the capillary condensation hysteresis loop, do not change appreciably. The change in pore volumes from G2 to G3 is smaller than would be expected for both samples; this will be discussed in more detail below in the context of the TGA and EA data. One possible explanation of this is pore mouth blockage/preferential formation of dendrimers at the pore mouth due to preferential attachment of the silane at the pore mouth opening. At the most cautious level, the adsorption data clearly shows that a significant portion of the organic content

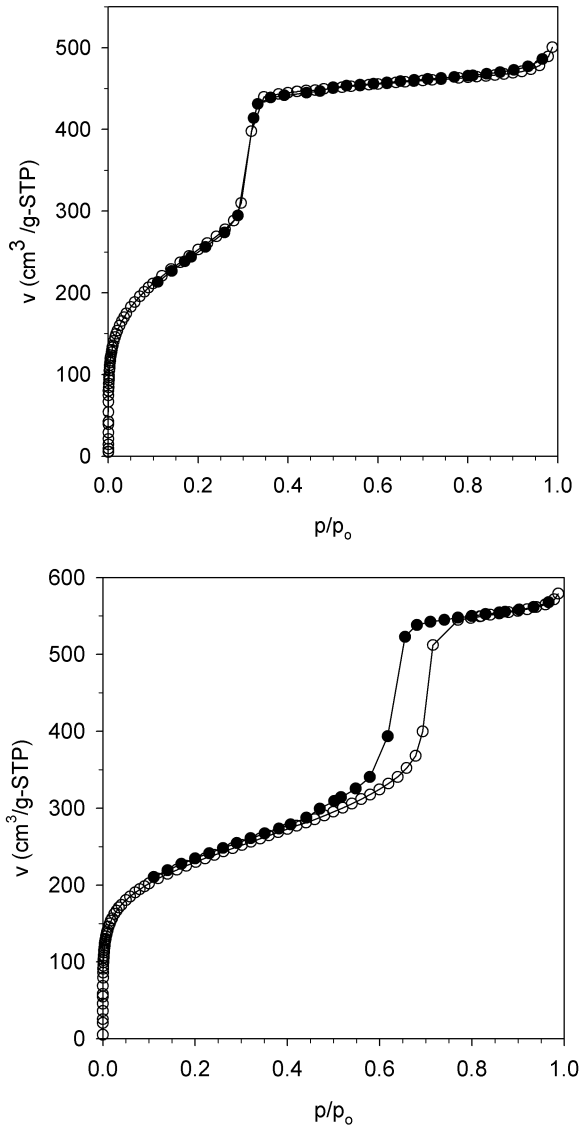

Figure 5.3. Nitrogen adsorption isotherms of (top) MCM-41 and (bottom) SBA-15. Adsorption branches are represented by open circles; desorption branches by solid circles.

Table 5.1. Summary of adsorption data of the OMS-nanocomposite materials.

Sample	$S(\alpha_s)$ (m^2/g)	$v_{meso}(\alpha_s)$ (cm^3/g)	d_{BJH} (nm)
MCM-41	906	0.68	3.5
NH_2-MCM-41	814	0.61	3.4
G1-AMP-MCM-41	597	0.40	3.0
G2-AMP-MCM-41	~ 0	~ 0	
G3-AMP-MCM-41	~ 0	~ 0	
G1-PIP-MCM-41	665	0.45	3.0
G2-PIP-MCM-41	408	0.22	3.0
G3-PIP-MCM-41	~ 0	~ 0	
SBA-15	766	0.78	7.8
NH_2-SBA-15	523	0.70	7.9
G1-AMP-SBA-15	401	0.56	7.9
G2-AMP-SBA-15	337	0.48	7.9
G3-AMP-SBA-15	320	0.43	7.5
G1-PIP-SBA-15	407	0.53	7.8
G2-PIP-SBA-15	339	0.43	7.5
G3-PIP-SBA-15	312	0.32	6.4

attached to the surface is in the mesopores given the pronounced decreases in the pore volume.

The amount of organic content occluded in the materials was determined by elemental analysis and thermogravimetric analysis. These results are summarized in Figure 5.4, along with calculations showing ideal weight loadings if every step proceeded at 100% efficiency. In general the elemental analysis and TGA data are in very good

agreement. However, the organic content of the amine-OMS samples is much higher (2.5-3 fold times larger) than would be predicted theoretically as are the G1 samples. NMR measurements do not show the presence of alkoxy groups. The TGA / EA results also indicate, consistent with the nitrogen adsorption data, that the reaction of converting the G2-MCM-41 materials to G3-MCM-41 materials is generally inefficient. Figure 5.5 shows the mmol of nitrogen per gram of silica for each of the samples as determined by elemental analysis. Several observations can be made from this data. The results shown here reinforce the conclusions from Figure 5.4. These include that the chemistry is inefficient in converting G2 dendrons to G3 dendrons, particularly for the AMP diamine. It also shows that conversion of the aminosilica to G1 dendrons is less efficient on SBA-15 than on MCM-41. We have observed this previously, and one possible explanation consistent with our prior work is that some of the amines preferentially graft into the micropores of SBA-15 and thus are inaccessible for further functionalization. If the chemistry went perfectly (i.e. 100% conversion at every step) the ratio of nitrogen should be 8: 22: 50 (1: 2.75: 6.25); as can be seen this is not observed. The motivation for showing Figure 5.5 is that all of the catalytic data will be presented as mmol of substrate consumed (or product formed) per mmol of nitrogen per gram of silica. Also, for the catalytic data shown the activity is normalized per mmol of nitrogen and not per mmol of periphery amines. In other words, we did not attempt to ascertain which fraction of the nitrogen atoms participate in the reaction. While it is not expected that the nitrogen centers on the cyanuric chloride, for instance, participate in the reaction it is unclear if the interior aliphatic amines do. Thus, given the consistency between the TGA and elemental analysis results we thought it appropriate to normalize based on the total nitrogen content.

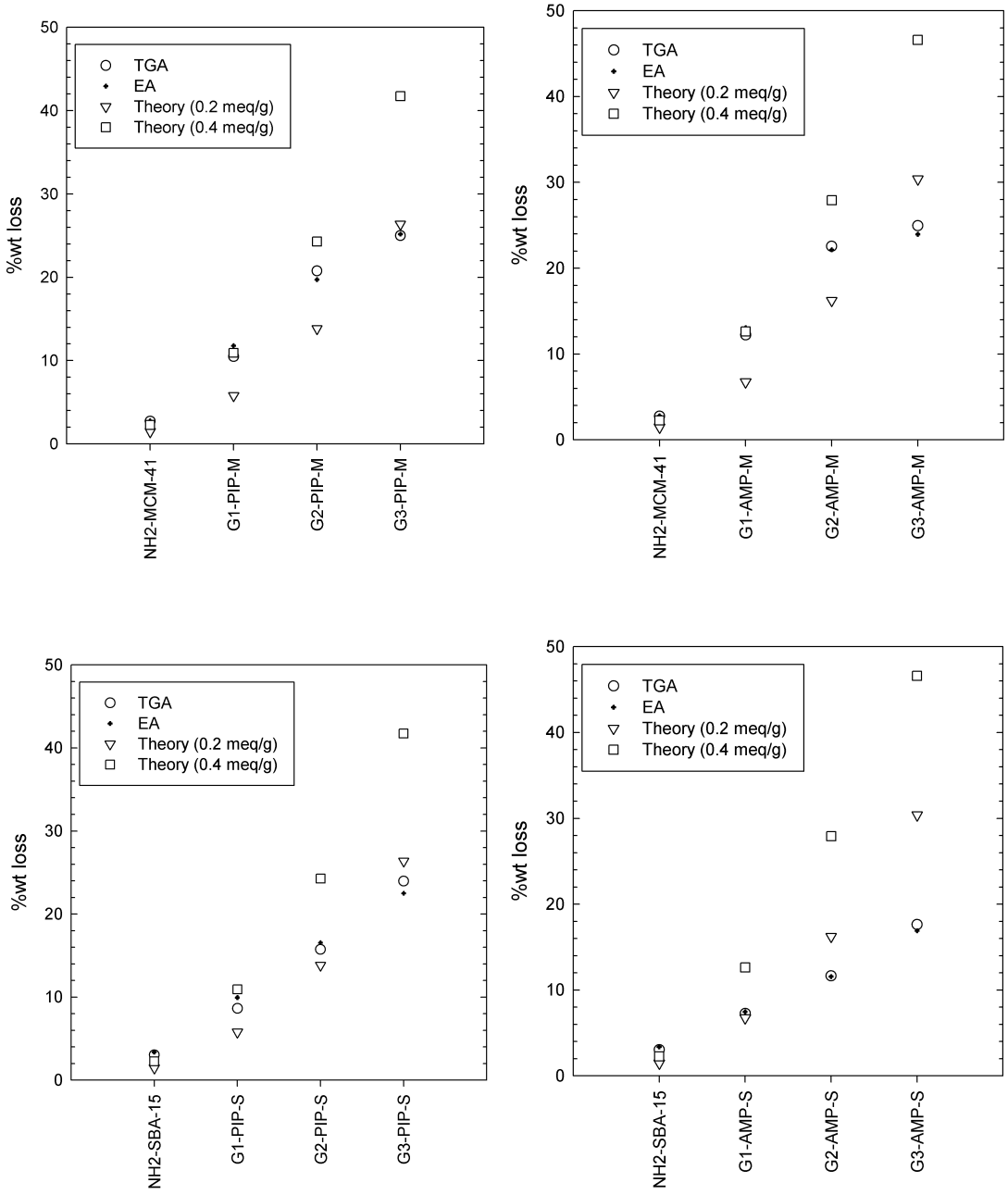

Figure 5.4. Plots comparing elemental analysis and TGA results along with theoretical weight losses assuming 100% conversion at every step.

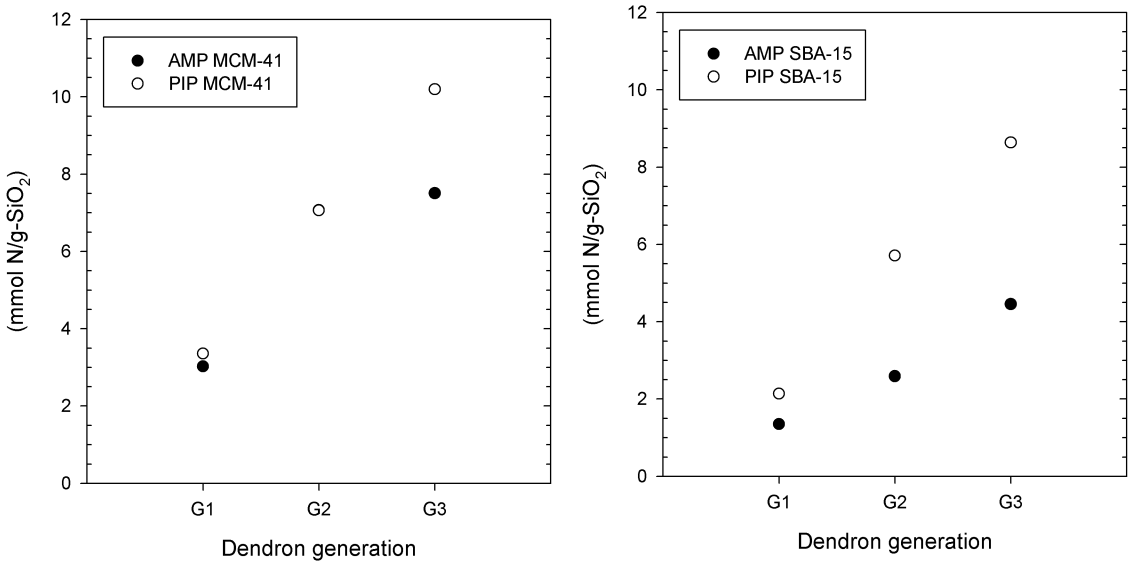

Figure 5.5. Nitrogen loading for the different samples as determined by elemental analysis. Note that for the G2-MCM-41 samples the mmol N/g-SiO_2 are essentially identical (i.e. the data markers overlap).

Evidence for organic group incorporation is obtained from $^{13}C\{^1H\}$ CP MAS NMR (Figure 5.6). The signal at 163 ppm is attributed to the aromatic carbons. The two resonances at approximately 40 and 25 ppm for the AMP-dendron hybrid samples are due to the aliphatic carbons of the 4-(aminomethyl)piperidine group. For the PIP-dendron hybrid samples the signal at 163 ppm is also due to the aromatic carbons from CC groups. The other strong signal at approximately 40 ppm is from the aliphatic carbons on piperazine groups.

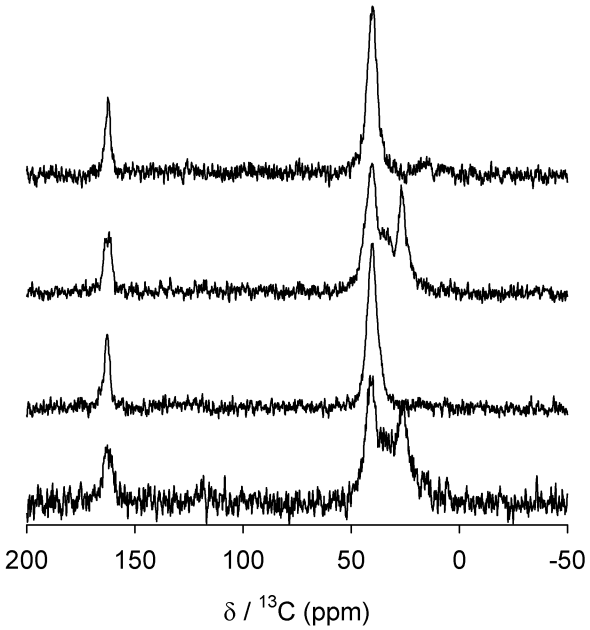

Figure 5.6. $^{13}C\{^{1}H\}$ CP MAS NMR spectra of (from top to bottom): G3-PIP MCM-41, G3-AMP MCM-41, G3-PIP SBA-15, and G3-AMP SBA-15.

5.3.2 Catalytic Testing, Nitroaldol Reaction

As several laboratories have investigated the nitroaldol reaction over amine-OMS materials we thought this was an appropriate test reaction to study the catalytic properties of our dendron-OMS materials. Figure 5.7 shows the conversion versus time and mmol of aldehyde consumed per mmol nitrogen per gram silica for the MCM-41-dendron composites. All samples (on a percent conversion basis) appear to possess reasonable activity for this reaction. When the conversion is normalized to the mmol of nitrogen per gram of silica several trends emerge. First, it becomes clear for both samples that the G1 dendron hybrids are the most active. Second, the AMP samples (on per mmol nitrogen basis) are also more active. Also noteworthy is that on a per site basis the G2 and G3

samples appear essentially identical. There are a few possible explanations for the decrease in activity of the higher generation dendrons. The first is that there are diffusion

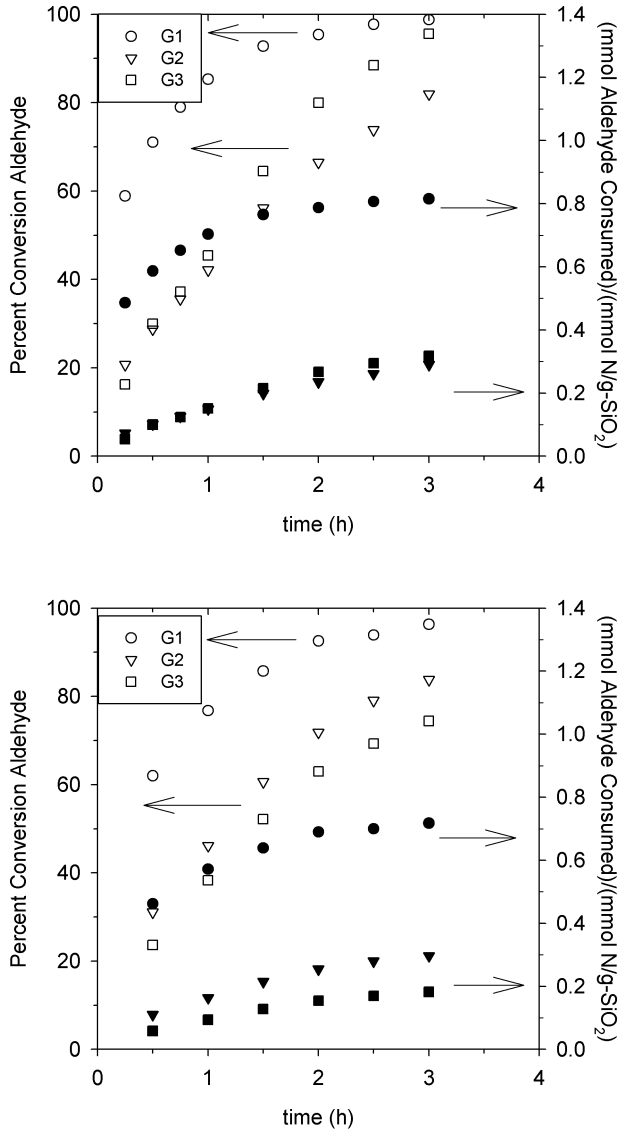

Figure 5.7. Conversion of aldehyde (left axis) and mmol aldehyde consumed per mmol nitrogen per gram of silica (right axis) versus time for AMP (top) and PIP (bottom) dendrons supported on MCM-41 in the nitroaldol reaction. Dendron generation denoted, solid symbols correspond to right axis, open symbols to left axis.

resistances present in the MCM-41 composites. The second is that the intrinsic activity of the sites decreases with increasing number densities of amines. The third, related to the second reason, is that as the dendron fragment gets larger there are less amine-silanol interactions. Based on the results mentioned below for the SBA-15 samples, we discount that the decreased activities observed can be solely attributed to diffusion effects.

Different generations of dendrimers, with AMP and PIP functional groups, on SBA-15 were also investigated (Figure 5.8). Again, on a percent conversion basis all samples appear active and comparable. When normalized to the nitrogen loading, however, some clear differences can be observed. First, these materials are more active on a per site basis than the MCM-41 samples, and there are clear differences in activity between G2 and G3 samples. This point can likely be assigned to the absence (or decrease) of diffusion resistances. The AMP samples are again more active than the PIP samples, and again the G1 samples are more active than the G2 and G3 samples. Taking the results in Figures 5.7 and 5.8 together, a few observations can be made. First, it appears that upon going to larger pored silicas the intrinsic activity of the dendrimers goes down with increasing dendron generation. The authors ascribe this to decreased amine-silanol interactions. The SBA-15 G2/G3 samples show statistically significant differences in reactivity in contrast to the MCM-41 G2/G3 samples. This likely indicates that for the MCM-41 samples significant diffusion resistances are present. The increase in the G1-AMP-SBA-15 reactivity as compared to the G1-AMP-MCM-41 sample also supports the presence of diffusion resistances in the MCM-41 composites.

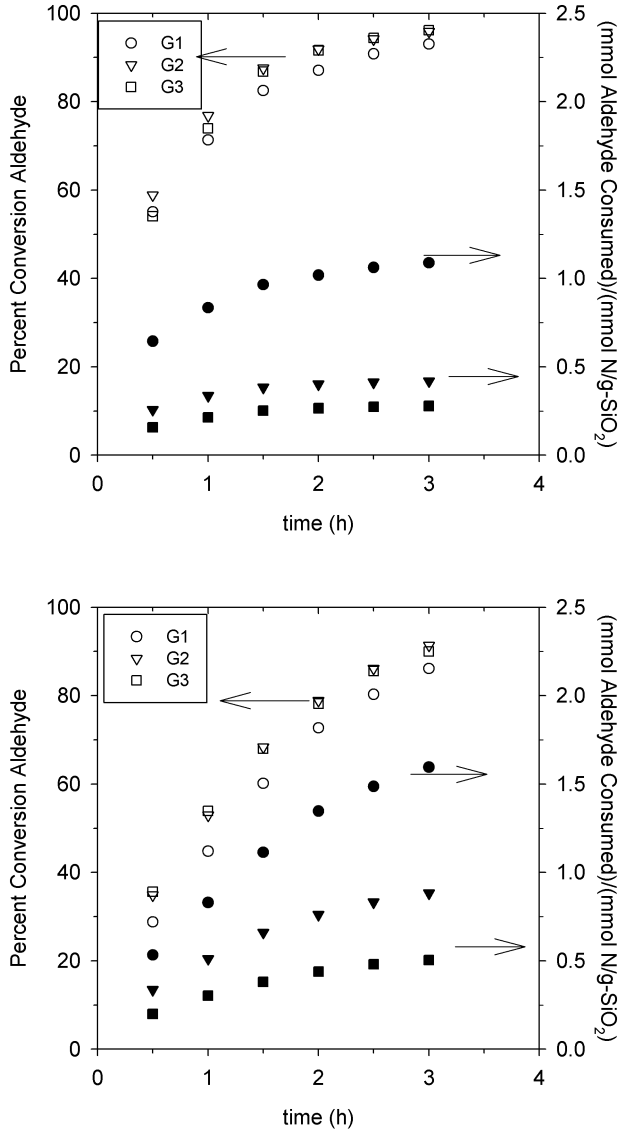

Figure 5.8. Conversion of aldehyde (left axis) and mmol aldehyde consumed per mmol nitrogen per gram of silica (right axis) versus time for AMP (top) and PIP (bottom) dendrons supported on SBA-15 in the nitroaldol reaction. Dendron generation denoted, solid symbols correspond to right axis, open symbols to left axis.

Figures 5.7 and 5.8 show that these materials are active catalysts for the Henry reaction. In addition, some clear trends can be discerned in the selectivity of the dendron

composites (i.e. alcohol versus alkene formation). Figure 5.9 shows the average selectivity for the samples as a function of dendron generation and amine (i.e. AMP versus PIP) identity. As can be seen in all cases, the selectivity to the nitroalcohol is very high (over 70%), and it can be observed that the nitroalcohol selectivity increases with increasing dendrimer generation and in going from primary amines to secondary amines. The error bars shown indicate one standard deviation from the average selectivity over the reaction run. That the selectivity to the alcohol is highest with the PIP samples and that it increases with increasing dendrimer generation are consistent with previous work by Katz as well as work from Asefa's laboratory.[85, 170, 220] In the case of the G3 dendrons one might expect that many of the amines are far enough from the surface that amine-silanol cooperativity effects are not observed. It is also worth noting that the 'initial' selectivity to the alcohol (at 15 or 30 minutes into the reaction) is always higher than the average selectivity shown in Figure 5.9. This would seem to indicate that it is possible for the alcohol to undergo subsequent dehydration to the olefin product.

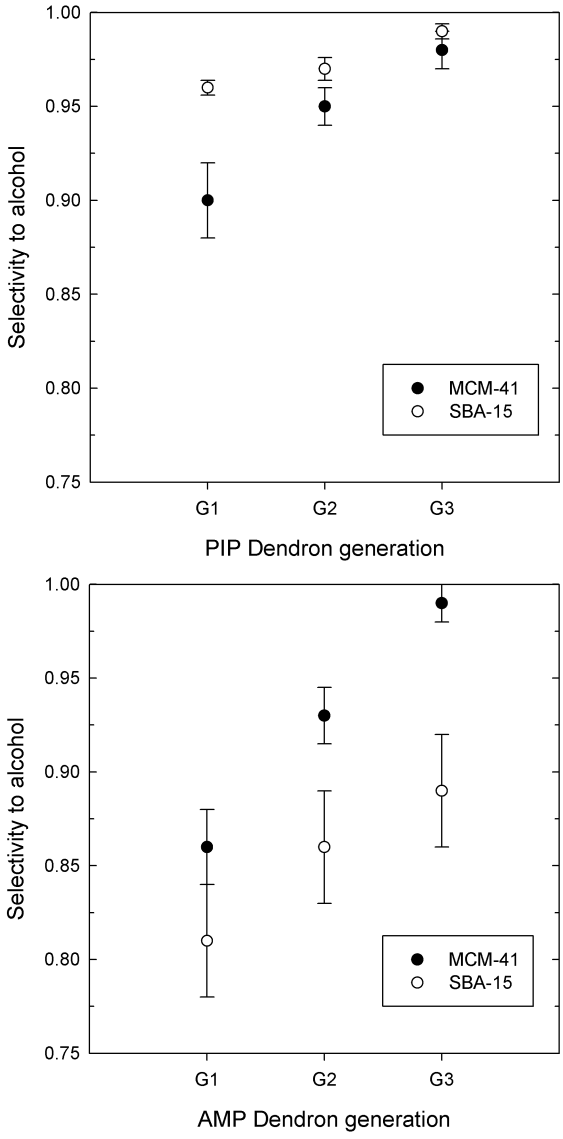

Figure 5.9. Selectivity to the nitroalcohol product for the AMP (top) and PIP (bottom) dendron composites.

5.3.3. Transesterification Reaction

Biodiesel, which is derived from triglycerides by transesterification with methanol, has attracted considerable attention during the past decade as a renewable, biodegradable, and nontoxic fuel [221-225]. Figure 5.10 shows conversion of triglyceride to methyl ester over dendron-MCM-41 hybrids at 338 K. The conversion is highest over the G1 samples, again consistent with diffusion resistances. The primary amine-terminated dendrons are slightly more active than the secondary amine-terminated dendrons based on the results in Figure 5.10. Figure 5.11 shows the same chemistry performed over SBA-15 dendron hybrids. The results in Figure 5.11 support the idea of diffusion resistances being present in the MCM-41 materials. The amount of methyl ester formed, particularly on a per mmol nitrogen basis, is significantly higher in the SBA-15 samples than in the MCM-41 samples. One can also see from the results in Figure 5.11 that the primary amines are significantly more active than the secondary amines in forming methyl esters.

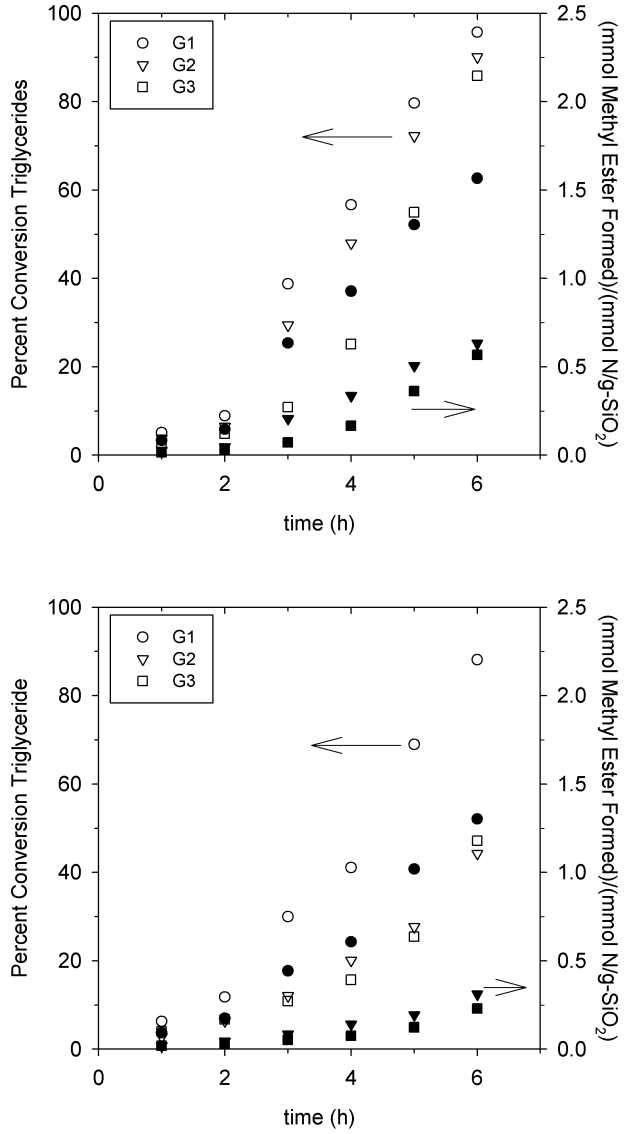

Figure 5.10. Conversion of triglyceride (left axis) and mmol methyl ester formed per mmol nitrogen per gram of silica (right axis) versus time for AMP (top) and PIP (bottom) dendrons supported on MCM-41. Dendron generation denoted, solid symbols correspond to right axis, open symbols to left axis.

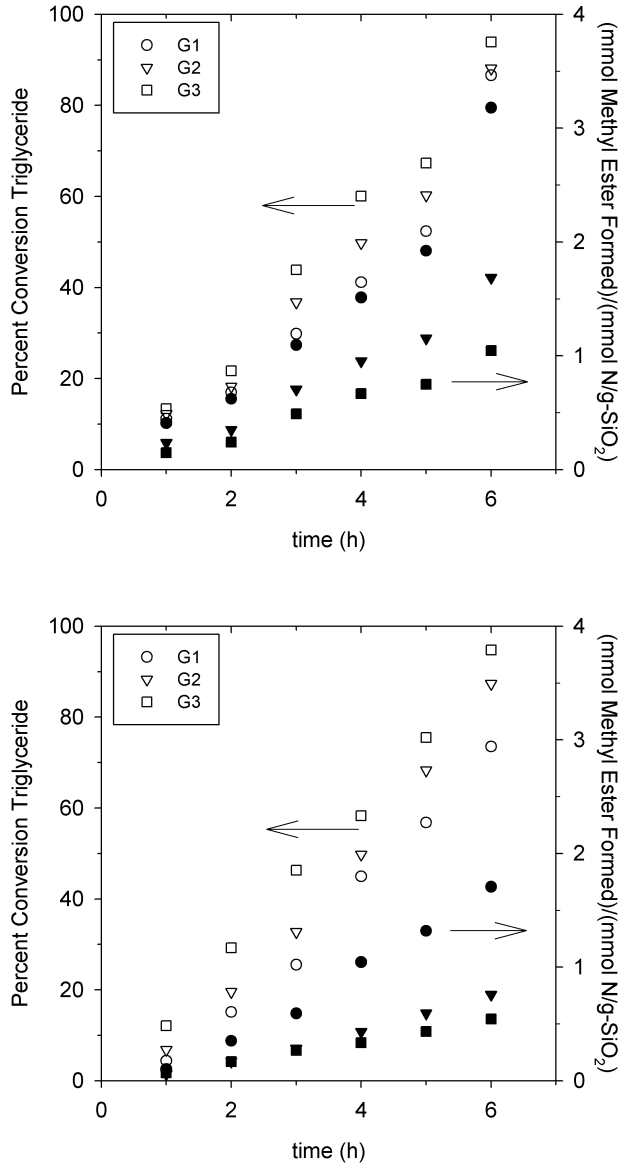

Figure 5.11. Conversion of triglyceride (left axis) and mmol methyl ester formed per mmol nitrogen per gram of silica (right axis) versus time for AMP (top) and PIP (bottom) dendrons supported on SBA-15. Dendron generation denoted, solid symbols correspond to right axis, open symbols to left axis.

While the conversions observed over these materials are encouraging the most significant result is their stability. Figure 5.12 shows the conversion of triglycleride after six hours as a function of catalyst recycle number. As can be seen there are only very modest decreases of conversion with multiple recycles. This is in contrast to previous work from our laboratory where simple aminosilane groups attached to OMS were used as catalysts for this reaction [226]. Thus the materials formed possess reasonable activity and stability. This is attributed to the dendron structure inhibiting the solvent from cleaving the silane attachment to the surface.

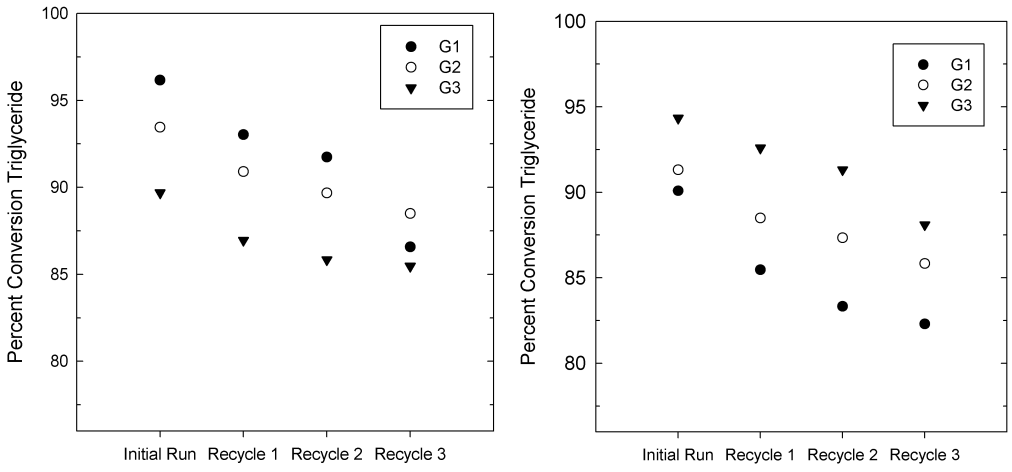

Figure 5.12. Conversion after six hours on stream versus recycle number for AMP MCM-41 (left) and AMP SBA-15 (right) dendron hybrids.

5.3.4 Aldol Coupling of HMF

The final reaction investigated was the condensation of 5-(hydroxymethyl)furfural (HMF) with acetone. This reaction represents a route to large alkanes in a biorefinery as HMF is formed via biomass hydrolysis and Aldol chemistry is often held up as a route to

larger hydrocarbons from biomass precursors [227, 228]. Figure 5.13 shows the conversions verse time in the cross aldol condensation of HMF with acetone catalyzed by G1-PIP MCM-41. The conversion is 20% after 6 hours of reaction and 80% after 32 hours. The preliminary result shows that the dendron-OMS hybrids are active in this reaction; however, the reaction rate is lower than those in the previously discussed reactions.

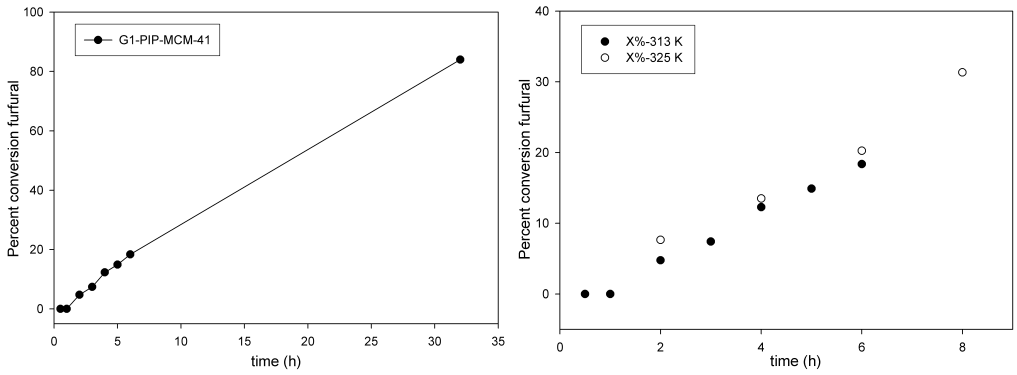

Figure 5.13. Conversion of HMF over G1-PIP MCM-41.

5.4 Conclusions

The synthesis and catalytic testing of several dendron-OMS materials are reported. These materials show potential for a wide range of chemical reactions including Aldol chemistry and transesterification reactions. The results observed in the nitroaldol reaction are qualitatively consistent with previous literature in terms of product selectivity, and the dendrons display good activity for this reaction. The dendron-OMS materials are not only active for the transesterification of triglycerides but also very stable. While possessing at best modest activity for the aldol reaction between HMF and

acetone at 313 K, the results indicate the OMS – dendron materials have potential as solid base catalysts for a range of reactions. Ongoing work is exploring additional chemistries, studying the thermal/solvothermal stability of the composites more carefully, and exploring multifunctional dendrons.

CHAPTER VI

^{2}H NMR DYNAMICS OF METHYLAMINE DENDRON ON MCM-41 AND SOLVENT EFFECTS

6.1 Introduction

In this chapter, methylpropylamine groups were attached to triazine-functionalized aminosilica MCM-41 to generate G1-methylamine-MCM-41. The functional group in the material was deuterium isotope labeled to investigate dynamics using ^{2}H MAS NMR. Here, the preliminary results indicated that the dendrimer structure leads to higher loading of methylamine groups, improving sensitivity. The deuterons located at the periphery of the dendrimer branches shows different or more motions, which is indicated by the narrower line shape of ^{2}H NMR spectra. Experiments were also performed where small amounts of solvent were adsorbed into the organic-OMS hybrids, providing a mimic 'in-situ' condition for the hybrid catalysts in the reaction. The effects of nitromethane solvent on the dynamics of functional groups were determined using ^{2}H MAS NMR.

6.2 Experimental

MCM-41 was synthesized and calcined as described in Chapter II, sublevel 2.4.2.1, and used as the solid support for post-synthetic grafting of propylamine groups (2.4.2.2). Scheme 6.1 shows how the materials were formed. The amine loading is 0.2 meq/g silica. Dealtails can be found in Chapter II, sublevel 2.4.5. The samples are

designated **2**–G1-MCM-41-0.2, and d_3-**2**–G1-MCM-41-0.2, which will be compared with the sample discussed in Chapter III, **2**-MCM-41-0.8, and d_3-**2**-MCM-41-0.8.

The solid-state ^{2}H MAS NMR spectra were recorded at 9.4 T on a Bruker Avance. The details of these experiments were discussed in (2.5.1.2).

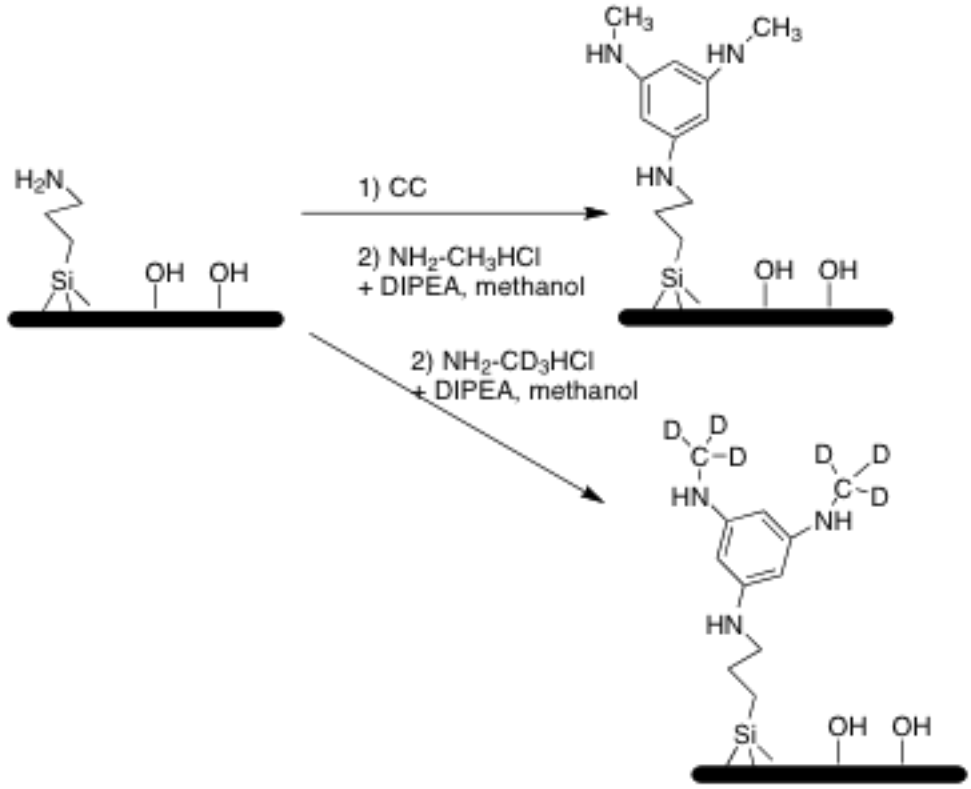

Scheme 6.1. Synthesis of *N*-methylpropylamine or d_3-*N*-methylpropylamine dendrons on MCM-41, designated as **2**-G1-MCM-41-0.2 or d_3-**2**-G1-MCM-41-0.2.

6.3 Results and Discussions

6.3.1 ^{2}H MAS NMR of *N*-methylpropylamine dendrons on MCM-41

Figure 6.1 shows the MAS spectra and fits of d_3-**2**-G1-MCM-41-0.2 at a loading of 0.2 meq/g and with spin rates of 2, 5, 10 kHz. In all the spectra, the envelopes of

spinning sidebands can be reasonably reproduced by the fits. The spectrum with the smallest MAS rate (2kHz) is most reliable for fitting purposes. Attempts to fit this spectrum lead to a QCC of approximately 28 kHz and a large asymmetry parameter of $\eta = 0.8$. To completely account for the central line intensity it was necessary to introduce another component with a QCC = 0 kHz and $\eta = 0$. The ratio of the intensity of two components determined from fitting is 95%: 5%. The need for two components is also observed for fitting the spectra at spin rates of 5 and 10 kHz.

Compared with the spectra and fittings of d_3-**2**-MCM-41-0.8 (shown in Figure 3.8 in Chapter III.) at a loading of 0.8 under the same spin rate, respectively, all the fittings here contain an additional isotropic line. Figure 6.1 shows that the dynamics of the methyl amine groups on the dendron have different rotational modes as compared to the simple *N*-methyl-propylamine groups investigated in Chapter III. Another point is that the dendritic propyl methylamine on MCM-41, d_3-**2**-G1-MCM-41-0.2 showed higher signal-to-noise ratios than d_3-**2**-MCM-41-0.8 under the same spin rates, even though the amine loading of the dendrimer structure is 0.2 meq/g, compared to that of 0.8 meq/g for d_3-**2**-MCM-41-0.8. Even considering double of the initial amine loadings 0.2 meq/g, 0.4

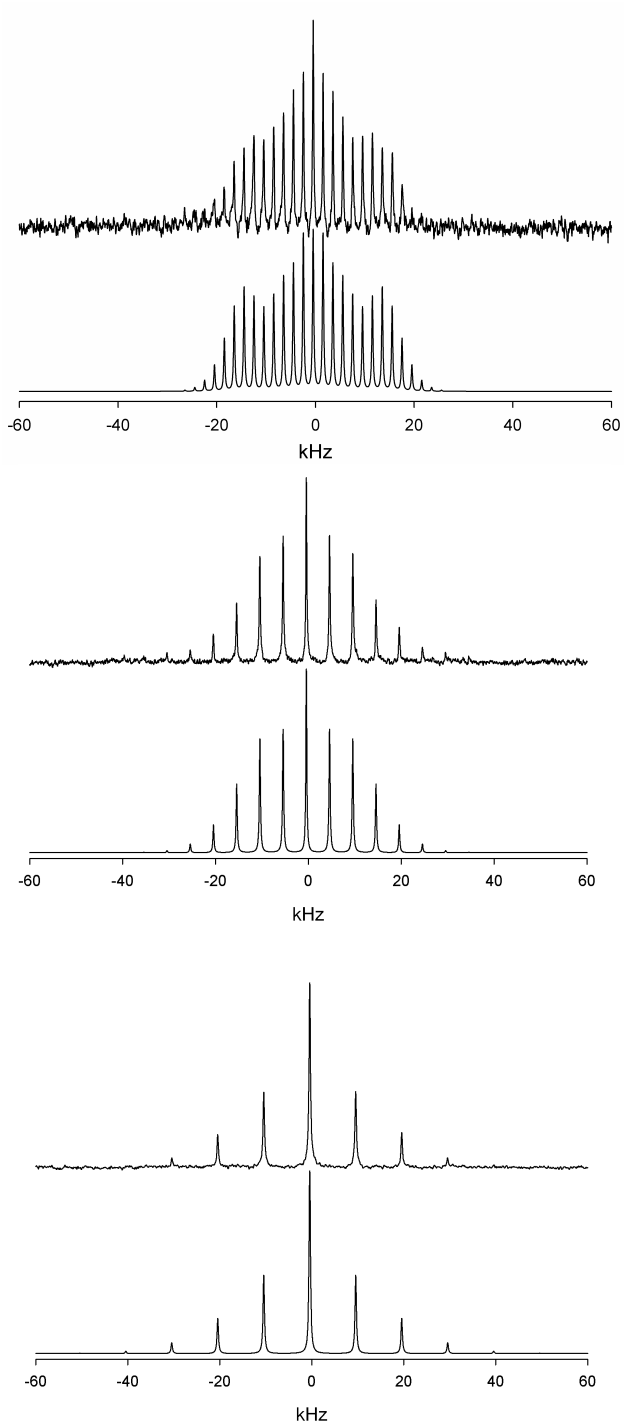

Figure 6.1. (From top to bottom) ^{2}H MAS NMR spectra and fits of **2**-G1-MCM-41-0.2 with spinning rates of 2 kHz, 5 kHz, and 10 kHz. In each stack plot, the upper trace is the spectrum and the lower trace is the fit.

meq/g of amine branches should be attached to MCM-41 in dendrimer structure, which is still lower than that of 0.8 meq/g loading. However, the sensitivity and signal-to-noise ratios of the spectra are still better than that of 0.8 meq/g loaded samples. For instance, the spectrum shown in Figure 6.1 with a spin rate of 2 kHz is recorded by the sum of 129400 FIDs, less than one third of 400000 FIDs used to obtain the spectrum in Figure 3.8 at the same spin rate but 3 times of original loadings. The narrower envelope of the sidebands indicates a smaller QCC, which is a consequence of multiple rotations. There are several possible explanations. First, the branched structures based on triazine possess more measurable deuterons on the OMS surface. Second, the dendrimer structure results in the *N*-methylpropylamine groups experiencing fewer steric constraints and potential hydrogen bonding as the groups are further from the OMS surface. The consequence of utilizing the triazine scaffold is shown in Scheme 6.2. The results above show that place the groups on the triazine scaffold leads to an increase in the rotational modes accessible.

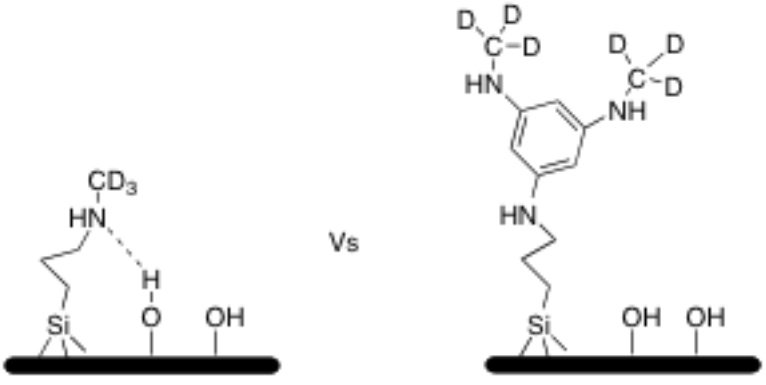

Scheme 6.2. Schematic hydrogen bonding between methylamine groups and surface silanols.

6.3.2 Solvent Effects on ^{2}H MAS NMR of *N*-methylpropylamine Dendrons on MCM-41

As shown in Chapters IV and V the amine functionalized OMS hybrid materials are catalytically active for the Henry reaction in nitromethane. Thus how solvent impacts dynamics and mobility is relevant from both a dynamics vantage but also in understanding the catalytic chemistry. Here I discuss some preliminary work about the dynamics of functional amines on MCM-41 in the presence of nitromethane using ^{2}H solid-state NMR spectroscopy.

Figure 6.2 shows the MAS spectra and fittings with spin rates of 2 kHz and 10 kHz of d_3-**2**-G1-MCM-41-0.2 with 15wt% of nitromethane solvent. Spectra obtained at spinning rates of both 2 kHz and 10 kHz are shown. Analysis of the spectrum at low spin rates should be more reliable. The spectrum of d_3-**2**-G1-MCM-41-0.2 with 15wt% of nitromethane measured at a spin rate of 2 kHz shows a shape close to a Pake doublet, with a small isotropic component observable. The QCC for the broad component is approximately 40 kHz with an asymmetry parameter η of 0.36. The intensity of the isotropic component is approximately 3%. The 'Pake doublet' fits the measured spectrum well.

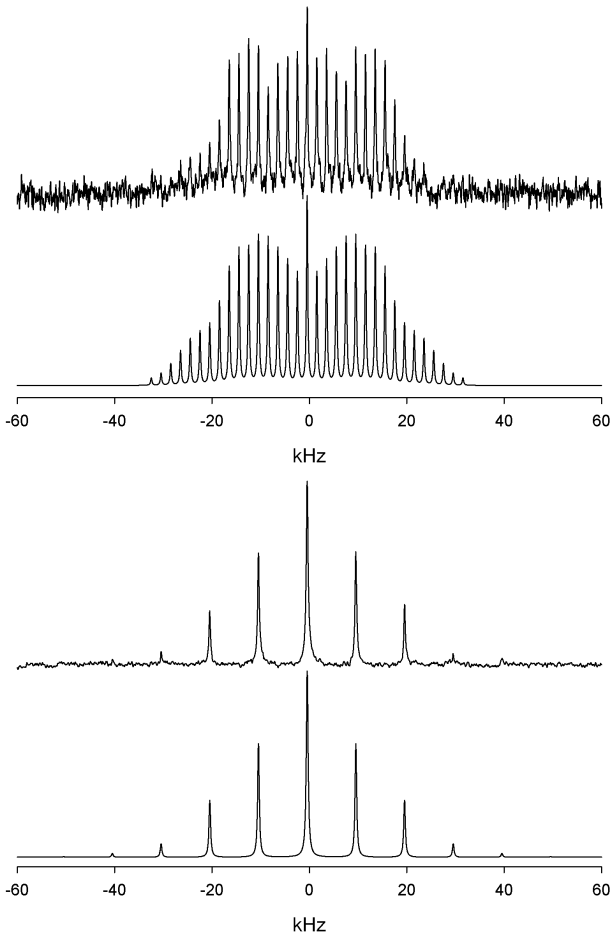

Figure 6.2. ^{2}H MAS NMR spectra and fits of **2**-G1-MCM-41 with 15wt% of nitromethane solvent measured with spinning rates of 2 kHz (top), and 10 kHz (bottom). In each stack plot, the upper trace is the spectrum and the lower trace is the fit.

Figure 6.3 shows the MAS spectra and fittings of d_3-**2**-G1-MCM-41-0.2 with 25wt% of nitromethane and with spin rates of 2 kHz, 10 kHz, and 0 kHz. The spectrum at 2 kHz is clearly triangular in shape. The spectrum could not be well explained by one resonance, and likely represents deuterons undergoing a broad distribution of motions. To fit the spectrum three components were needed, one with a QCC of 20 kHz and an asymmetry parameter η of 0.57, one with a QCC of 30 kHz with an asymmetry

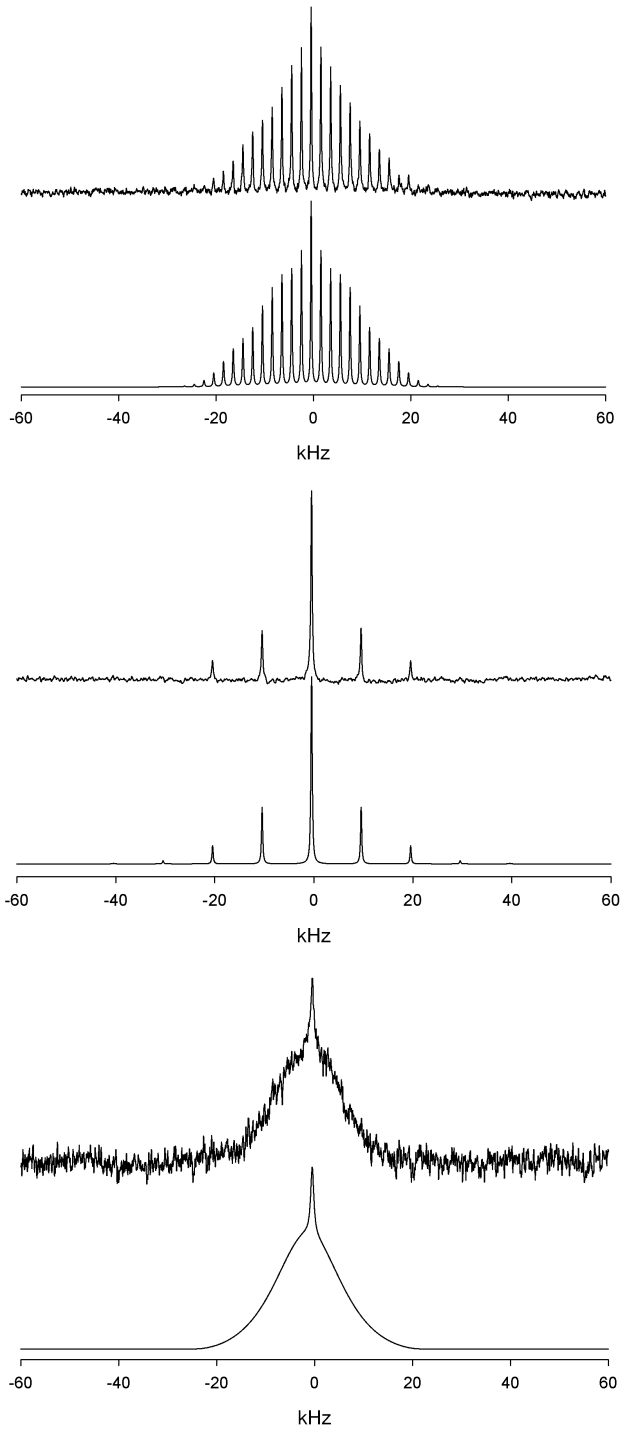

Figure 6.3. (From top to bottom) ^{2}H MAS NMR spectra and fits of **2**-G1-MCM-41 with 25wt% of nitromethane solvent measured with spinning rates of 2 kHz, 10 kHz, and 0 kHz. In each stack plot, the upper trace is the spectrum and the lower trace is the fit.

parameter η = 0.79, and an isotropic peak of 3% intensity. The intensities of the two quadrupolar components were 42% to 55%, respectively. As shown in Figure 6.3, the other two MAS spectra obtained with MASR of 10 kHz as well as 0 kHz. This fit is consistent with the presence of a broad distribution of motions, and attempts to interpret the line shape rigorously are likely not warranted. The static spectrum is consistent with the low speed MAS spectrum.

In all these spectra, the line width is narrower than that of methylamine groups not attached to dendrimers (i.e. Figure 3.7). The line narrowing indicates additional motions. The changes of spectra shape are due to the different motions of the deuterons under solvent surroundings. The results indicated that there are interactions between the methylamine groups and the nitromethane solvent, which may be the hydrogen bonding shown as Scheme 6.2. Also, the amount of solvent is a significant factor for the different line shapes in Figure 6.2 and Figure 6.3. The QCC of the spectrum in Figure 6.2 with less nitromethane solvent in the materials would be expected to be smaller than that of the sample measured without solvent. The results showed the other way that the QCC for the spectra in Figure 6.2 are larger than those in Figure 6.1, which indicated fewer motions. The phenomena can be explained by the hydrogen bonding between the amine groups and the nitromethane (as shown in Scheme 6.2). With this explanation, the spectra in Figure 6.3 of the sample with 25wt% of nitromethane, would show an even larger QCC from fewer motions. However, the spectra in Figure 6.3 display a combination of two smaller QCC compared with those in Figure 6.2, which indicates two sets of motions. The reason for this could be the hydrogen bonding between the amine groups and part of the nitromethane molecules, and the excess solvent system provided another solution

environment for the deuterons which access faster molecule motions in the solvent. Another possible reason for this is that the solvent inhibits H-bonding between the amines and silanols, and this leads to more rotational modes.

6.3.3 Solid-state ^{2}H MAS NMR of Methylamine-MCM-41 with Solvent Nitromethane

In order to verify the additional isotropic peak in the spectra is not due to nitromethane, ^{2}H MAS NMR spectra of **2**-MCM-41-0.8 with 30wt% nitromethane, in which no isotopically labeled chemicals were used, were performed at spin rate of 10 kHz, keeping the other parameters constant, and after about 7000 scans, there is no peak observed. The results indicated that the natural abundant of deuterons present in the nitromethane is not enough for the signal sensitivity to collect solid-state NMR spectra.

Figure 6.4 shows the MAS spectra and fittings of d_3-**2**-MCM-41-0.8 with 12.5wt% of nitromethane solvent with spin rates of 5 kHz and 10 kHz. The spectrum measured at 10 kHz (shown as Figure 6.4 bottom) is from the sum of 7000 FIDs. The spectrum at 5 kHz contains a quadrupolar component with a QCC of 41 kHz and an asymmetry parameter $\eta = 0.46$, an isotropic component. The relative intensities of the two components is 83%: 17%. The fit of the spectrum measured at a spin rate of 10 kHz is very similar.

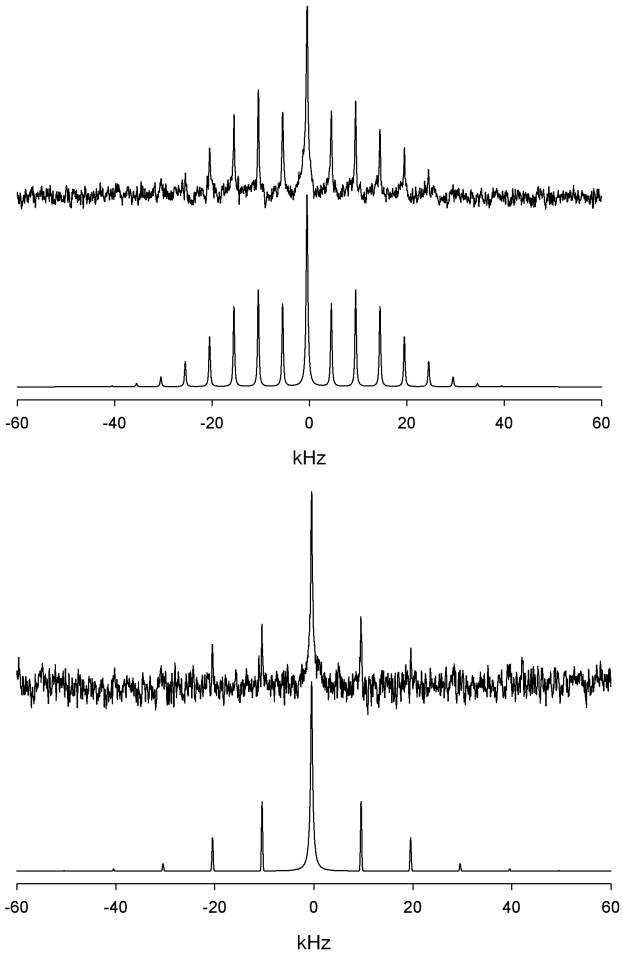

Figure 6.4. ^{2}H MAS NMR spectra and fits of **2**-MCM-41-0.8 with 12.5wt% of nitromethane solvent measured with spinning rates of 5 kHz (top), and 10 kHz (bottom). In each stack plot, the upper trace is the spectrum and the lower trace is the fit.

Compared with the spectra in Figure 3.8 of d_3-**2**-MCM-41-0.8 (without nitromethane present), some important differences emerge. In that case a broader line is observed, consistent with the amine group have more rotational modes accessible in the presence of solvent. As shown in Scheme 6.2, there is hydrogen bonding between simple methylamine groups with silanol groups on MCM-41 surface, which causes the bending motions of CD_3 groups discussed in Chapter III. Here, the introduction of nitromethane

likely reduces those influences, and the solvation results in more motions. The isotropic peak could arise from either isotropic reorientation or a rotational mode that averages $3\cos^2\theta$-1 to zero, i.e. diamond lattice. Another possibility for the isotropic component could be the H/D exchanging in the nitromethane solvent. While, comparing the signal sensitivity and intensity keeping the other measurement parameters constant for different trials, the possibility of H/D exchanging between nitromethane solvent and amine groups could be eliminated. In the experimental procedure, the sample with solvent was degassed in vacumm oven for 24 hours after collecting the NMR spectra, and then it was reloaded with similar amount of solvent, the spectra were recorded with the same number of FIDs under the same parameters. The results indicate that the intensity and signal-to-noise rate is stable, which means that possible H/D exchange is likely not origin of the central line.

Figure 6.5 shows the MAS spectra and fittings of d_3-**2**-MCM-41-0.8 with 30wt% of nitromethane solvent measured with a spin rate of 5 kHz, and the number of FIDs is similar to that of Figure 6.4, approximately 150000 scans. In this spectrum, the envelope of the sidebands is similar to that in Figure 6.4. Fitting by Dmfit program indicates that there are two components, one with a QCC of 32 kHz and an asymmetry parameter of 0.85, and the other is an isotropic line with an intensity of 35%. The results indicated that solvent leads to more motions. One possibility is that solvent inhibits the hydrogen bonding between methylamine groups and surface silanols. An increase in the isotropic line indicates an increasing population of spins undergoing multiple rotational modes.

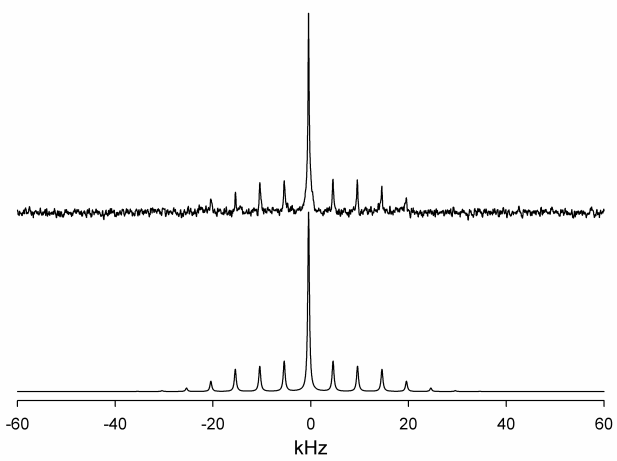

Figure 6.5. ^{2}H MAS NMR spectra and fits of **2**-MCM-41-0.8 with 30wt% of nitromethane measured with spinning rates of 5 kHz. In the figure, the upper trace is the spectrum and the lower trace is the fit.

6.4 Conclusions

In this chapter, methylamine groups were used to cap G1 dendrimer structures on MCM-41. The results indicated that the dendrimer structure increased the sensitivity of ^{2}H signals in solid-state ^{2}H MAS NMR measurements. Several examples of *N*-methylamine and its G1 dendrimer materials were successfully loaded with nitromethane solvent at the solid-state NMR measurements. The results indicated that one aspect of the effects of solvent on the molecular motions of CD_3 are due to the solvation, which reduced the hydrogen bonding between the methylamine groups and surface silanols. The other effect of the solvent is the solution environment, which cause higher intensity of the isotropic component. In order to quantify the interactions, more work based on a variety of nitromethane loadings would be worth pursuing.

CHAPTER VII

CONCLUSIONS AND FUTURE WORK

7.1 Conclusions

In this dissertation, we investigated syntheses and characterization of amine functionalized OMS (MCM-41 and SBA-15) hybrid materials. By introducing isotopically labeled amine groups on OMS, the dynamics of organic functional fragments covalently attached on OMS could be analyzed using solid-state ^{2}H NMR. The other work focused on the catalytic properties of the hybrid materials, through their applications in the base catalyzed reactions, such as the nitroaldol (Henry) reaction, transterification condensation, and aldol reaction.

First, several simple functional groups with isotope labeled ^{2}H were successfully covalently attached onto the surface of MCM-41 and SBA-15. The objective in these materials was to elucidating the organic-OMS interface and understanding the rotational mobility of the organic groups with respect to the surface by solid-state NMR techniques, especially ^{2}H NMR. These studies were addressed in Chapter III. The results showed that deuterons on different organic groups attached on OMS displayed distinct molecular motions. The steric structure of the functional groups, the restraint of the pore size from the solid supports MCM-41 and SBA-15, and the interactions of surface silanols with functional groups have vital effects on the molecular motions. The presence of the interactions of surface silanols with amine groups has been invoked to explain the observed catalytic properties of the hybrid materials, which were discussed in Chapter IV. The interesting results of Chapter III stimulated the discussions about the dynamics of

relatively complex structures. In Chapter VI, the G1 methylamine dendrons attached on MCM-41 were designed to study the effects of higher loadings from dendrimer structures on the mobility of the functional molecules. The space branching increased the sensitivity and intensity of deuteron signals compared with that of the propylamine attached on MCM-41. The possible factor for the phenomena should be more effective deuterons from eliminating the interactions of amine groups with surface silanols. Another respect of the studies about molecular dynamics is about the effects of solvent surroundings on the molecular motions. The preliminary results of the dynamics of simple propylmethylamine, G1 methylamine dendrons attached on MCM-41 with nitromethane solvent were covered in Chapter VI, which indicated that the solvent injected in the mesoporous materials influenced the molecule rotations because of the hydrogen bonding interactions between the solvent molecules and the amine groups. The amount of the loaded solvent is also important for the motions.

The other goal of our work here is the catalytic properties of amine-functionalized OMS hybrid materials. The hybrid catalysts were tested in several reactions. The amine identity, the density of amine goups, the surface hydrophobicity, the pore size of the solid supports used, and dendrimer structures were introduced to discussion. Chapter IV focuses on the catalytic properties of simple amines groups attached on MCM-41 in the nitroaldol reaction. Chapter V discussed the catalytic properties of polyamine dendrimer structures attached on MCM-41 and SBA-15 in the nitroaldol reaction, the transesterification reaction, and the aldol reaction. The dendron-OMS materials show potential applications for a wide range of chemical reactions. The hybrid catalysts showed good activity for the nitroaldol reaction and the transesterificaiton reaction as

well as good thermal stability. The materials also display potentials for the Aldol chemistry.

7.2 Future Work

Based on the results of this dissertation, there are many possible directions future work could be taken. In the following, suggested future work focuses on two terms of respects, one is determining the conformation and the dynamics of organic groups attached to the OMS surface, the other is designing more functionalities on OMS surface and testing the catalytic properties.

7.2.1 Molecular Dynamics Based on Solid-state NMR of Functional Groups Attached to OMS Surface

Based on the results of Chapter III and Chapter VI, ^{2}H NMR is useful to indicate the dynamics of functional groups covalently attached to OMS surface. The hyperbranched dendrimer structures lead to high loadings of functional groups. This has the advantage of improved sensitivity in the NMR work. The space branching structure changes the interactions between amine groups and surface silanols, which are dependent on the spin distance. The less restricted fragments may show faster mobility. The increased sensitivity by higher deuteron loading makes it possible to measure spin - lattice relaxation time T_1 of amine functional groups. In addition to methylpropylamine groups discussed in Chapter VI, many other organic functional fragments will be interesting for this study.

The promising results about the dynamics of the amine groups with nitromethne solvent, shown in Chapter VI, invoke further discussions of functional groups in-situ reaction conditions, like the reactant solvent. In this respect, many choices of solvents based on the polarity, the acidity, the molecular size, and so on, would be interesting fundamental researches. The materials were tested in the nitroaldol reaction, the transesterification reaction, and aldol reaction in our work here, so the corresponding solvents would be the first set of choice, such as nitromethane, methanol, acetone.

The dendrimer-OMS structure possesses well-defined architectures, which provide a model system for controlling the distances between functional groups via generation, or between proximal groups with different functionality. Multifunctionalities can be tethered to proximal branches in the dendrimer-OMS structure based on the selective attachment of triazine under different temperatures. The local conformation of multiple functionalities can be investigated by various solid-state NMR techniques as well as ^{2}H NMR, like REDOR.

7.2.2 Catalytic Properties of Organic-OMS Hybrid Materials

Our work issued in Chapter IV and V stimulates further investigations based on organic functionalizations on OMS surface. Ongoing work based on our material systems is exploring additional chemistries, studying the thermal/solvothermal stability of the dendron-OMS hybrid materials. The materials are active in the aldol reaction, however, the conversion rate should be improved, by controlling the reaction temperature, changing the density of active sites, and combining multiple functionalities on the hyperbranches.

REFERENCES

[1] M.E. Davis, Nature 417 (2002) 813-821.

[2] N. Husing, Porous Hybrid Materials. Wiley - VCH, Weinheim, 2007.

[3] C. Baerlocher, L.B. McCusker, D. Olson, W.M. Meier, Atlas of Zeolite Framework Types. Elsevier, 2007.

[4] O.M. Yaghi, M. O'Keeffe, N.W. Ockwig, H.K. Chae, M. Eddaoudi, J. Kim, Nature 423 (2003) 705-714.

[5] A. Imhof, D.J. Pine, Nature 389 (1997) 948-951.

[6] B.T. Holland, C.F. Blanford, A. Stein, Science 281 (1998) 538-540.

[7] B.T. Holland, L. Abrams, A. Stein, J. Am. Chem. Soc. 121 (1999) 4308-4309.

[8] B.T. Holland, C.F. Blanford, T. Do, A. Stein, Chem. Mater. 11 (1999) 795-805.

[9] C.F. Blanford, T.N. Do, B.T. Holland, A. Stein, Advanced Catalytic Materials-1998 549 (1999) 61-66

[10] H.W. Yan, C.F. Blanford, B.T. Holland, M. Parent, W.H. Smyrl, A. Stein, Adv. Mater. 11 (1999) 1003-1006.

[11] F. Svec, J.M.J. Frechet, Science 273 (1996) 205-211.

[12] C.T. Kresge, M.E. Leonowicz, W.J. Roth, J.C. Vartuli, J.S. Beck, Nature 359 (1992) 710-712.

[13] J.S. Beck, J.C. Vartuli, W.J. Roth, M.E. Leonowicz, C.T. Kresge, K.D. Schmitt, C.T.W. Chu, D.H. Olson, E.W. Sheppard, S.B. McCullen, J.B. Higgins, J.L. Schlenker, J. Am. Chem. Soc. 114 (1992) 10834-10843.

[14] D.Y. Zhao, J.L. Feng, Q.S. Huo, N. Melosh, G.H. Fredrickson, B.F. Chmelka, G.D. Stucky, Science 279 (1998) 548-552.

[15] D.Y. Zhao, Q.S. Huo, J.L. Feng, B.F. Chmelka, G.D. Stucky, J. Am. Chem. Soc. 120 (1998) 6024-6036.

[16] A. Corma, H. Garcia, Adv. Synth. Catal. 348 (2006) 1391-1412.

[17] D.M. Ford, E.E. Simanek, D.F. Shantz, Nanotechnology 16 (2005) S458-S475.

[18] A.P. Wight, M.E. Davis, Chem. Rev. 102 (2002) 3589-3613.

[19] F. Hoffmann, M. Cornelius, J. Morell, M. Froba, Angew. Chem. Int. Ed. 45 (2006) 3216-3251.

[20] A. Stein, Adv. Mater. 15 (2003) 763-775.

[21] K. Sakaguchi, M. Matsui, F. Mizukami, Applied Microbiology and Biotechnology 67 (2005) 306-311.

[22] S. Yoo, J.D. Lunn, S. Gonzalez, J.A. Ristich, E.E. Simanek, D.F. Shantz, Chem. Mater. 18 (2006) 2935-2942.

[23] D.R. Radu, C.Y. Lai, K. Jeftinija, E.W. Rowe, S. Jeftinija, V.S.Y. Lin, J. Am. Chem. Soc. 126 (2004) 13216-13217.

[24] A. Corma, H. Garcia, Chem. Rev. 103 (2003) 4307-4365.

[25] Y. Wan, and D. Zhao, Chem. Rev. 107 (2007) 2821-2860.

[26] D. Astruc, F. Lu, J.R. Aranzaes, Angew. Chem. Int. Ed. 44 (2005) 7852-7872.

[27] L.M. Bronstein, Top. Curr. Chem. 226 (2003) 55-89.

[28] J.D. Holmes, D.M. Lyons, K.J. Ziegler, Chem. Eur. J. 9 (2003) 2144-2150.

[29] B.F.G. Johnson, Top. Catal. 24 (2003) 147-159.

[30] Q.Q. Wang, D.F. Shantz, J. Sol. State. Chem. 181 (2008) 1659-1669.

[31] R. Ryoo, J.M. Kim, J. Chem. Soc., Chem. Commun. 7 (1995) 711-712.

[32] J.M. Kim, J.H. Kwak, S. Jun, R. Ryoo, J. Phys. Chem. 99 (1995) 16742-16747.

[33] A.E.A. Shahbazi, H. Younesi, A. Badiel, Chem. Eng. J. (2010), DOI: 10.10.16/j.cej.2010.11.053.

[34] K.J. Edler, P.A. Reynolds, J.W. White, J. Phys. Chem. B 102 (1998) 3676-3683.

[35] K.J. Edler, J.W. White, J. Mater. Chem. 9 (1999) 2611-2615.

[36] K.J. Edler, J.W. White, J. Chem. Soc., Chem. Commun. 2 (1995) 155-156.

[37] Q.S. Huo, R. Leon, P.M. Petroff, G.D. Stucky, Science 268 (1995) 1324-1327.

[38] C.Z. Yu, J. Fan, B.Z. Tian, D.Y. Zhao, Chem. Mater. 16 (2004) 889-898.

[39] J.S. Beck, J.C. Vartuli, G.J. Kennedy, C.T. Kresge, W.J. Roth, S.E. Schramm, Chem. Mater. 6 (1994) 1816-1821.

[40] V. Alfredsson, H. Amenitsch, K. Flodstrom, M. Linden, C.V. Teixeira, H. Wennerstrom, Nanoporous Materials 156 (2005) 69-74.

[41] U. Ciesla, F. Schuth, Micro. Meso. Mater. 27 (1999) 131-149.

[42] C.F. Cheng, Z.H. Luan, J. Klinowski, Langmuir 11 (1995) 2815-2819.

[43] G.D. Stucky, A. Monnier, F. Schuth, Q. Huo, D. Margolese, D. Kumar, M. Krishnamurty, P. Petroff, A. Firouzi, M. Janicke, B.F. Chmelka, Molecular Crystals and Liquid Crystals Science and Technology Section a-Molecular Crystals and Liquid Crystals 240 (1994) 187-200.

[44] Q.S. Huo, D.I. Margolese, U. Ciesla, P.Y. Feng, T.E. Gier, P. Sieger, R. Leon, P.M. Petroff, F. Schuth, G.D. Stucky, Nature 368 (1994) 317-321.

[45] Q.S. Huo, D.I. Margolese, U. Ciesla, D.G. Demuth, P.Y. Feng, T.E. Gier, P. Sieger, A. Firouzi, B.F. Chmelka, F. Schuth, G.D. Stucky, Chem. Mater. 6 (1994) 1176-1191.

[46] Y. Wan, D.Y. Zhao, Chem. Rev. 107 (2007) 2821-2860.

[47] S.D. Shen, Y.Q. Li, Z.D. Zhang, J. Fan, B. Tu, W.Z. Zhou, D.Y. Zhao, Chem. Commun. 19 (2002) 2212-2213.

[48] D.Y. Zhao, Q.S. Huo, J.L. Feng, J.M. Kim, Y.J. Han, G.D. Stucky, Chem. Mater. 11 (1999) 2668-2672.

[49] Q.S. Huo, D.I. Margolese, G.D. Stucky, Chem. Mater. 8 (1996) 1147-1160.

[50] Q.S. Huo, P. Sieger, A. Firouzi, B.F. Chmelka, G.D. Stucky, Abstracts of Papers of the American Chemical Society 209 (1995) 283.

[51] S. Che, A.E. Garcia-Bennett, T. Yokoi, K. Sakamoto, H. Kunieda, O. Terasaki, T. Tatsumi, Nature Materials 2 (2003) 801-805.

[52] S.D. Shen, A.E. Garcia-Bennett, Z. Liu, Q.Y. Lu, Y.F. Shi, Y. Yan, C.Z. Yu, W.C. Liu, Y. Cai, O. Terasaki, D.Y. Zhao, J. Am. Chem. Soc. 127 (2005) 6780-6787.

[53] Y. Sakamoto, M. Kaneda, O. Terasaki, D.Y. Zhao, J.M. Kim, G. Stucky, H.J. Shim, R. Ryoo, Nature 408 (2000) 449-453.

[54] X.H. Bu, P.Y. Feng, G.D. Stucky, Chem. Mater. 12 (2000) 1505-1507.

[55] S.A. Bagshaw, E. Prouzet, T.J. Pinnavaia, Science 269 (1995) 1242-1244.

[56] P.T. Tanev, T.J. Pinnavaia, Science 267 (1995) 865-867.

[57] J.Y. Ying, C.P. Mehnert, M.S. Wong, Angew. Chem. Int. Ed. 38 (1999) 56-77.

[58] A. Shimojima, K. Kuroda, Angew. Chem. Int. Ed. 42 (2003) 4057-4060.

[59] A. Shimojima, Z. Liu, T. Ohsuna, O. Terasaki, K. Kuroda, J. Am. Chem. Soc. 127 (2005) 14108-14116.

[60] K. Flodstrom, H. Wennerstrom, C.V. Teixeira, H. Amenitsch, M. Linden, V. Alfredsson, Langmuir 20 (2004) 10311-10316.

[61] F. Berube, F. Kleitz, S. Kaliaguine, J. Mate. Sci. 44 (2009) 6727-6735.

[62] S. Shylesh, M.P. Kapoor, L.R. Juneja, P.R. Samuel, C. Srilakshmi, A.R. Singh, J. Mol. Catal.-Chemical 301 (2009) 118-126.

[63] H. Kosslick, G. Lischke, G. Walther, W. Storek, A. Martin, R. Fricke, Micro. Mater. 9 (1997) 13-33.

[64] T.R. Pauly, Y. Liu, T.J. Pinnavaia, S.J.L. Billinge, T.P. Rieker, J. Am. Chem. Soc. 121 (1999) 8835-8842.

[65] R.F. Zhang, C. Yang, J. Mater. Chem. 18 (2008) 2691-2703.

[66] J. Iglesias, J.A. Melero, M. Sanchez-Sanchez, Micro. Meso. Mater. 132 (2010) 112-120.

[67] C.Z. Loebick, S. Lee, S. Derrouiche, M. Schwab, Y.A. Chen, G.L. Haller, L. Pfefferle, J. Catal. 271 (2010) 358-369.

[68] M.H. Lim, A. Stein, Chem. Mater. 11 (1999) 3285-3295.

[69] M. Barczak, S. Pikus, B. Skrzydlo-Radomanska, A. Dabrowski, Adsorption-Journal of the International Adsorption Society 15 (2009) 278-286.

[70] M. Barczak, E. Skwarek, W. Janusz, A. Dabrowski, S. Pikus, Applied Surface Science 256 (2010) 5370-5375.

[71] P.F. Fulvio, S. Pikus, M. Jaroniec, Acs Applied Materials & Interfaces 2 (2010) 134-142.

[72] B.F. Shi, Y.S. Wang, Y.L. Guo, Y.Q. Wang, Y. Wang, Y. Guo, Z.G. Zhang, X.H. Liu, G.Z. Lu, Catal. Today 148 (2009) 184-188.

[73] M. Barczak, A. Dabrowski, M. Iwan, Z. Rzaczynska, Nano 2008: 2nd National Conference on Nanotechnology 146 (2009) 12002-12002

[74] D. Brunel, A.C. Blanc, A. Galarneau, F. Fajula, Catal. Today 73 (2002) 139-152.

[75] M. Alvaro, A. Corma, D. Das, V. Fornes, H. Garcia, Chem. Commun. 8 (2004) 956-957.

[76] A. Cauvel, G. Renard, D. Brunel, J. Org. Chem. 62 (1997) 749-751.

[77] D. Brunel, Micro. Meso. Mater. 27 (1999) 329-344.

[78] S.J.O. Julia-Christina Wasilke, R. Tom Baker, Guillermo C. Bazan, Chem. Rev. 105 (2005) 1001-1020.

[79] M.H. Lim, A. Stein, Abstracts of Papers of the American Chemical Society 213 (1997) 391.

[80] D. Margolese, J.A. Melero, S.C. Christiansen, B.F. Chmelka, G.D. Stucky, Chem. Mater. 12 (2000) 2448-2459.

[81] V. Dufaud, M.E. Davis, J. Am. Chem. Soc. 125 (2003) 9403-9413.

[82] Y.F. Feng, X.Y. Yang, Y. Di, Y.C. Du, Y.L. Zhang, F.S. Xiao, J. Phys. Chem. B 110 (2006) 14142-14147.

[83] M.L. Testa, V. La Parola, A.M. Venezia, Catal. Today 158 (2010) 109-113.

[84] T. Nakamura, Y. Yamada, K. Yano, J. Mater. Chem. 17 (2007) 3726-3732.

[85] J.D. Bass, A. Katz, Chem. Mater. 18 (2006) 1611-1620.

[86] E.L. Margelefsky, A. Bendjeriou, R.K. Zeidan, V. Dufaud, M.E. Davis, J. Am. Chem. Soc. 130 (2008) 13442-13449.

[87] E.L. Margelefsky, R.K. Zeidan, M.E. Davis, Chem. Soc. Rev. 37 (2008) 1118-1126.

[88] E.L. Margelefsky, R.K. Zeidan, V. Dufaud, M.E. Davis, J. Am. Chem. Soc. 129 (2007) 13691-13697.

[89] R.K. Zeidan, M.E. Davis, J. Catal. 247 (2007) 379-382.

[90] J.D. Bass, A. Katz, Chem. Mater. 15 (2003) 2757-2763.

[91] J.D. Bass, A. Solovyov, A.J. Pascall, A. Katz, J. Am. Chem. Soc. 128 (2006) 3737-3747.

[92] J.D. Bass, S.L. Anderson, A. Katz, Angew. Chem. Int. Ed. 42 (2003) 5219-5222.

[93] J.L. Defreese, A. Katz, Chem. Mater. 17 (2005) 6503-6506.

[94] S. Huh, J.W. Wiench, J.-C. Yoo, M. Pruski, V.S.Y. Lin, Chem. Mater. 15 (2003) 4247-4256.

[95] S. Inagaki, S. Guan, Y. Fukushima, T. Ohsuna, O. Terasaki, J. Am. Chem. Soc. 121 (1999) 9611-9614.

[96] A. Stein, M.H. Lim, C.F. Blanford, Abstracts of Papers of the American Chemical Society 216 (1998) U315.

[97] K.K. Sharma, T. Asefa, Angew. Chem. Int. Ed. 46 (2007) 2879-2882.

[98] J.C. Hicks, R. Dabestani, A.C.I. Buchanan, C.W. Jones, Chem. Mater. 18 (2006) 5022-5032.

[99] J.C. Hicks, and C.W. Jones, Langmuir 21 (2006) 2676-2681.

[100] M.W. McKittrick, C.W. Jones, Chem. Mater. 15 (2003) 1132-1139.

[101] A. Stein, M.H. Lim, Abstracts of Papers of the American Chemical Society 214 (1997) 46.

[102] M. Manzano, V. Aina, C.O. Arean, F. Balas, V. Cauda, M. Colilla, M.R. Delgado, M. Vallet-Regi, Chem. Eng. J. 137 (2008) 30-37.

[103] M.K. Kidder, P.F. Britt, Z.T. Zhang, S. Dai, A.C. Buchanan, Chem. Commun. 22 (2003) 2804-2805.

[104] R.J. Chimentao, S. Abello, F. Medina, J. Llorca, J.E. Sueiras, Y. Cesteros, P. Salagre, J. Catal. 252 (2007) 249-257.

[105] Y. Kubota, Y. Nishizaki, H. Ikeya, M. Saeki, T. Hida, S. Kawazu, M. Yoshida, H. Fujii, Y. Sugi, Micro. Meso. Mater. 70 (2004) 135-149.

[106] Y. Kubota, H. Ikeya, Y. Sugi, T. Yamada, T. Tatsumi, J. Mol. Cat. A - Chem. 249 (2006) 181-190.

[107] Y. Kubota, Y. Sugi, T. Tatsumi, Catalysis Surveys from Asia 11 (2007) 158-170.

[108] F.C. Bigi, S.; Maggi, R.; Mazzacani, A.; Sartori, G., Stud. Surf. Sci. Catal. 130 (2000).

[109] X.G. Wang, K.S.K. Lin, J.C.C. Chan, S.F. Cheng, J. Phys. Chem. B 109 (2005) 1763-1769.

[110] G. Wulff, B. Heide, G. Helfmeier, J. Am. Chem. Soc. 108 (1986) 1089-1091.

[111] A. Walcarius, M. Etienne, B. Lebeau, Chem. Mater. 15 (2003) 2161-2173.

[112] X.G. Wang, K.S.K. Lin, J.C.C. Chan, S. Cheng, Chem. Commun. 23 (2004) 2762-2763.

[113] K.K. Sharma, R.P. Buckley, T. Asefa, Langmuir 24 (2008) 14306-14320.

[114] D.J. Macquarrie, R. Maggi, A. Mazzacani, G. Sartori, R. Sartorio, Appl. Catal. A - Gen. 246 (2003) 183-188.

[115] T. Yokoi, H. Yoshitake, T. Yamada, Y. Kubota, T. Tatsumi, J. Mater. Chem. 16 (2006) 1125-1135.

[116] S. Huh, H.T. Chen, J.W. Wiench, M. Pruski, and V.S.Y. Lin, J. Am. Chem. Soc. 126 (2004) 1010-1011.

[117] S. Huh, H.T. Chen, J.W. Wiench, M. Pruski, V.S.Y. Lin, Angew. Chem. Int. Ed. 44 (2005) 1826-1830.

[118] R.K. Zeidan, V. Dufaud, M.E. Davis, J. Catal. 239 (2006) 299-306.

[119] R.K. Zeidan, S.-J. Hwang, M.E. Davis, Angew. Chem. Int. Ed. 45 (2006) 6332-6335.

[120] S. Jaenicke, G.K. Chuah, X.H. Lin, X.C. Hu, Micro. Meso. Mater. 35-6 (2000) 143-153.

[121] P. Banet, N. Marcotte, D.A. Lemer, D. Brunel, Langmuir 24 (2008) 9030-9037.

[122] H.T. Chen, S. Huh, J.W. Wiench, M. Pruski, V.S.Y. Lin, J. Am. Chem. Soc. 127 (2005) 13305-13311.

[123] D.R. Radu, C.Y. Lai, J.G. Huang, X. Shu, V.S.Y. Lin, Chem. Commun. 10 (2005) 1264-1266.

[124] R.Y. Zhang, W. Ding, B. Tu, D.Y. Zhao, Chem. Mater. 19 (2007) 4379-4381.

[125] J.M. Rosenholm, A. Meinander, E. Peuhu, R. Niemi, J.E. Eriksson, C. Sahlgren, M. Linden, Acs Nano 3 (2009) 197-206.

[126] J.M. Rosenholm, M. Linden, Journal of Controlled Release 128 (2008) 157-164.

[127] J.M. Rosenholm, E. Peuhu, J.E. Eriksson, C. Sahlgren, M. Linden, Nano Letters 9 (2009) 3308-3311.

[128] X. Feng, G.E. Fryxell, L.Q. Wang, A.Y. Kim, J. Liu, K.M. Kemner, Science 276 (1997) 923-926.

[129] M.H. Lim, C.F. Blanford, A. Stein, J. Am. Chem. Soc. 119 (1997) 4090-4091.

[130] M.H. Lim, C.F. Blanford, A. Stein, Chem. Mater. 10 (1998) 467-470.

[131] F. Vögtle, G. Richardt, N. Werner, Dendrimer Chemistry. Wiley-VCH, 2009.

[132] G. Kickelbick, Hybrid Materials : Synthesis, Characterization, and Applications. Wiley - VCH, 2007.

[133] M.B. Steffensen, E. Hollink, F. Kuschel, M. Bauer, E.E. Simanek, Journal of Polymer Science Part a-Polymer Chemistry 44 (2006) 3411-3433.

[134] E.E. Simanek, H. Abdou, S. Lalwani, J. Lim, M. Mintzer, V.J. Venditto, B. Vittur, Proceedings of the Royal Society a-Mathematical Physical and Engineering Sciences 466 (2010) 1445-1468.

[135] E.J. Acosta, S.O. Gonzalez, E.E. Simanek, Journal of Polymer Science Part a-Polymer Chemistry 43 (2005) 168-177.

[136] E.J. Acosta, C.S. Carr, E.E. Simanek, D.F. Shantz, Adv. Mater. 16 (2004) 985-989.

[137] S. Yoo, J.D. Lunn, S. Gonzalez, J.A. Ristich, E.E. Simanek, D.F. Shantz, Chem. Mater. 18 (2006) 2935-2942.

[138] S. Yoo, S. Yeu, R.L. Sherman, E.E. Simanek, D.F. Shantz, D.M. Ford, J. Membrane Sci. 334 (2009) 16-22.

[139] S.J. Dilly, S.J. Carlisle, A.J. Clark, A.R. Shepherd, S.C. Smith, P.C. Taylor, A. Marsh, Journal of Polymer Science Part a-Polymer Chemistry 44 (2006) 2248-2259.

[140] J.M. Rosenholm, A. Penninkangas, M. Linden, Chem. Commun. 37 (2006) 3909-3911.

[141] J.M. Rosenholm, A. Duchanoy, M. Linden, Chem. Mater. 20 (2008) 1126-1133.

[142] K.Q. Yu, C.W. Jones, J. Catal. 222 (2004) 558-564.

[143] J.C. Hicks, J.H. Drese, D.J. Fauth, M.L. Gray, G.G. Qi, C.W. Jones, J. Am. Chem. Soc. 130 (2008) 2902-2903.

[144] B. Gonzalez, M. Colilla, C.L. de Laorden, M. Vallet-Regi, J. Mater. Chem. 19 (2009) 9012-9024.

[145] J.P.K. Reynhardt, Y. Yang, A. Sayari, H. Alper, Chem. Mater. 16 (2004) 4095-4102.

[146] J.P.K. Reynhardt, Y. Yang, A. Sayari, H. Alper, Adv. Func. Mater. 15 (2005) 1641-1646.

[147] C.C. Yu, L.X. Zhang, F. Qin, J.T. Li, J.L. Shi, D.S. Yan, J. Inorg. Mater. 23 (2008) 1231-1235.

[148] M.P. Kapoor, H. Kuroda, M. Yanagi, H. Nanbu, L.R. Juneja, Topics in Catalysis 52 (2009) 634-642.

[149] M.P. Kapoor, Y. Kasama, T. Yokoyama, M. Yanagi, S. Inagaki, N. Hironobu, L.R. Juneja, J. Mater. Chem. 16 (2006) 4714-4722.

[150] B. Fadhel, M. Hearn, A. Chaffee, Micro. Meso. Mater. 123 (2009) 140-149.

[151] Z.J. Liang, B. Fadhel, C.J. Schneider, A.L. Chaffee, Adsorption-Journal of the International Adsorption Society 15 (2009) 429-437.

[152] Z. Liang, B. Fadhel, C.J. Schneider, A.L. Chaffee, Micro. Meso. Mater. 111 (2008) 536-543.

[153] R. Serna-Guerrero, E. Da'na, A. Sayari, Industrial & Engineering Chemistry Research 47 (2008) 9406-9412.

[154] M. Bhagiyalakshmi, S. Do Park, W.S. Cha, H.T. Jang, Applied Surface Science 256 (2010) 6660-6666.

[155] L. Hajiaghabael, A. Badiel, M.R. Ganjali, S. Heydari, Y. Khaniani, G.M. Ziarani, Desalination 266 (2011) 182-187.

[156] A.P. Wight, M.E. Davis, Chem. Rev. 102 (2002) 3589-3614.

[157] A. Corma, H. Garcia, Adv. Synth. Catal. 348 (2006) 1391-1412.

[158] I. Rodriguez, S. Iborra, A. Corma, F. Rey, J.L. Jorda, Chem. Commun. 7 (1999) 593-594.

[159] I. Rodriguez, S. Iborra, F. Rey, A. Corma, Appl. Catal. a-General 194 (2000) 241-252.

[160] I. Diaz, C. Marquez-Alvarez, F. Mohino, J. Perez-Pariente, E. Sastre, J. Catal. 193 (2000) 283-294.

[161] W.D. Bossaert, D.E. De Vos, W.M. Van Rhijn, J. Bullen, P.J. Grobet, P.A. Jacobs, J. Catal. 182 (1999) 156-164.

[162] W.M. Van Rhijn, D.E. De Vos, B.F. Sels, W.D. Bossaert, P.A. Jacobs, Chem. Commun. 3 (1998) 317-318.

[163] J.H. Clark, A.J. Butterworth, S.J. Tavener, A.J. Teasdale, S.J. Barlow, T.W. Bastock, K. Martin, Journal of Chemical Technology and Biotechnology 68 (1997) 367-376.

[164] Y. Kubota, K. Goto, S. Miyata, Y. Goto, Y. Fukushima, Y. Sugi, Chem. Lett. 32 (2003) 234-235.

[165] K.-I. Shimizu, E. Hayashi, T. Inokuchi, T. Kodama, H. Hagiwara, Y. Kitayama, Tetrahedron Lett. 43 (2002) 9073-9075.

[166] K. Shimizu, H. Suzuki, E. Hayashi, T. Kodama, Y. Tsuchiya, H. Hagiwara, Y. Kitayama, Chem. Commun. 10 (2002) 1068-1069.

[167] X.H. Lin, G.K. Chuah, S. Jaenicke, J. Mol. Cat. A - Chem. 150 (1999) 287-294.

[168] A. Katz, M.E. Davis, Nature 403 (2000) 286-289.

[169] A. Anan, R. Vathyam, K.K. Sharma, T. Asefa, Catal. Lett. 126 (2008) 142-148.

[170] K.K. Sharma, T. Asefa, Angew. Chem. Int. Ed. 46 (2007) 2879-2882.

[171] D. Dhar, I. Beadham, S. Chandrasekaran, Proc. Indian Acad. Sci. (Chem. Sci.) 115 (2003) 365-372.

[172] S.W. Kim, S.J. Bae, T. Hyeon, B.M. Kim, Micro. Meso. Mater. 44 (2001) 523-529.

[173] A. Bhaumik, T. Tatsumi, J. Catal. 189 (2000) 31-39.

[174] R.Y. Zhang, W. Ding, B. Tu, D.Y. Zhao, Chem. Mater. 19 (2007) 4379-4381.

[175] H.W. Spiess, K. Schmidt-Rohr, Disorder Effects on Relaxational Processes. Springer, 1994.

[176] D.L. Tzou, K. Schmidt-Rohr, H.W. Spiess, Polymer 35 (1994) 4728-4733.

[177] J. Leisen, K. Schmidt-Rohr, H.W. Spiess, Journal of Non-Crystalline Solids 172 (1994) 737-750.

[178] J. Sommer, Y. Yang, D. Rambow, J. Blumel, Inorg. Chem. 43 (2004) 7561-7563.

[179] T. Posset, F. Rominger, J. Blumel, Chem. Mater. 17 (2005) 586-595.

[180] A. Huwe, F. Kremer, M. Arndt, P. Behrens, W. Schwieger, G. Ihlein, O. Akdogan, F. Schuth, Dynamics in Small Confining Systems Iv 543 (1999) 115-123

[181] F. Kremer, A. Huwe, M. Arndt, P. Behrens, W. Schwieger, Journal of Physics-Condensed Matter 11 (1999) A175-A188.

[182] A. Huwe, F. Kremer, P. Behrens, W. Schwieger, Phys. Rev. Lett. 82 (1999) 2338-2341.

[183] F. Kremer, Molecular Dynamics in Confined Space. Wiley-VCH, 2003.

[184] F. Kremer, A. Schonhals, Broadband Dielectric Spectroscopy. Springer, 2003.

[185] A. Vyalikh, T. Emmler, I. Shenderovich, Y. Zeng, G.H. Findenegg, G. Buntkowsky, PhysChemChemPhys 9 (2007) 2249-2257.

[186] G. Buntkowsky, H. Breitzke, A. Adamczyk, F. Roelofs, T. Emmler, E. Gedat, B. Grunberg, Y.P. Xu, H.H. Limbach, I. Shenderovich, A. Vyalikh, G. Findenegg, PhysChemChemPhys 9 (2007) 4843-4853.

[187] T. Amitay-Rosen, S. Kababya, S. Vega, J. Phys. Chem. B 113 (2009) 6267-6282.

[188] W. Masierak, T. Emmler, E. Gedat, A. Schreiber, G.H. Findenegg, G. Buntkowsky, J. Phys. Chem. B 108 (2004) 18890-18896.

[189] J.L. Defreese, S.J. Hwang, A.N.G. Parra-Vasquez, A. Katz, J. Am. Chem. Soc. 128 (2006) 5687-5694.

[190] D.D. Laws, H.M.L. Bitter, A. Jerschow, Angew. Chem. Int. Ed. 41 (2002) 3096-3129.

[191] H. Friebolin, Basic One- and Two-Dimensional NMR-Spectroscopy. Wiley-VCH, 2005.

[192] K. Schmidt-Rohr, H.W. Spiess, Multidimensional Solid-state NMR and Polymers. Academic Press, 1994.

[193] J. Schraml, J.M. Bellama, Two-Dimensional NMR Spectroscopy. Wiley, 1988.

[194] R.N. Ibbett, NMR Spectroscopy of Polymers. Blackie Academic & Professional, 1993.

[195] M.J. Duer, Introduction to Solid-state NMR Spectroscopy. Blackwell, Oxford, 2004.

[196] M.A. Kennedy, R.R. Vold, R.L. Vold, J. Magn. Reson. 91 (1991) 301-315.

[197] D.F. Shantz, C. Fild, H. Koller, R.F. Lobo, J. Phys. Chem. B 103 (1999) 10858-10865.

[198] J.S. Waugh, J. Magn. Reson. 68 (1986) 189-192.

[199] J. Schaefer, E.O. Stejskal, R. Buchdahl, Abstracts of Papers of the American Chemical Society 172 (1976) 4-4.

[200] J. Schaefer, E.O. Stejskal, J. Am. Chem. Soc. 98 (1976) 1031-1032.

[201] J.L. Weil, S.L. Tan, J.S. Waugh, D.D. Osheroff, J. Magn. Reson. 66 (1986) 264-273.

[202] D.A. Torchia, A. Szabo, J. Magn. Reson. 49 (1982) 107-121.

[203] F. Rouquerol, J. Rouquerol, K.S.W. Sing, Adsorption by Powders and Porous Solids: Principles, Methodology and Applications. Academic Press, 1999.

[204] M. Jaroniec, M. Kruk, J.P. Olivier, Langmuir 15 (1999) 5410-5413.

[205] S.J. Gregg, K.S.W. Sing, Adsorption, Surface Area and Porosity. Academic Press, 198.

[206] M. Kruk, M. Jaroniec, A. Sayari, Langmuir 13 (1997) 6267-6273.

[207] K.J. Edler, J.W. White, Chem. Mat. 9 (1997) 1226-1233.

[208] D. Massiot, F. Fayon, M. Capron, I. King, S. Le Calve, B. Alonso, J.O. Durand, B. Bujoli, Z.H. Gan, G. Hoatson, Magn. Reson. Chem. 40 (2002) 70-76.

[209] M. Bak, J.T. Rasmussen, N.C. Nielsen, J. Magn. Reson. 147 (2000) 296-330.

[210] M. Morgenstern, J. Cline, S. Meyer, S. Cataldo, Energy Fuels 20 (2006) 1350-1353.

[211] G. Buntkowsky, H. Breitzke, A. Adamezyk, F. Roelofs, T. Emmler, E. Gedat, B. Grunberg, Y. Xu, H.H. Limbach, J. Shenderovich, A. Vyalikh, G.H. Findenegg, PhysChemChemPhys 9 (2007) 4843-4853.

[212] A. Jentys, K. Kleestorfer, H. Vinek, Micro. Meso. Mater. 27 (1999) 321-328.

[213] H. Kosslick, H. Landmesser, R. Fricke, Journal of the Chemical Society-Faraday Transactions 93 (1997) 1849-1854.

[214] S. Ashtekar, J.J. Hastings, P.J. Barrie, L.F. Gladden, Spectroscopy Letters 33 (2000) 569-584.

[215] N. Bloembergen, Nuclear Magnetic Relaxation. W. A. Benjamin Inc., 1961.

[216] A.J. Vega, Z. Luz, J. Phys. Chem. 91 (1987) 365-373.

[217] H.W. Spiess, H. Sillescu, J. Magn. Reson. 42 (1981) 381-389.

[218] S.L. Hruby, B.H. Shanks, J. Catal. 263 (2009) 181-188.

[219] R.W. Snell, E. Combs, B.H. Shanks, Top Catal. 53 (2010) 1248-1253.

[220] K.K. Sharma, T. Asefa, Angew. Chem. Int. Ed. 46 (2007) 2879-2882.

[221] A. Cauvel, G. Renard, D. Brunel, Journal of Organic Chemistry 62 (1997) 749-751.

[222] M. Di Serio, M. Ledda, M. Cozzolino, G. Minutillo, R. Tesser, E. Santacesaria, Industrial & Engineering Chemistry Research 45 (2006) 3009-3014.

[223] M. Di Serio, R. Tesser, L. Pengmei, E. Santacesaria, Energy Fuels 22 (2008) 207-217.

[224] S. Gryglewicz, Bioresource Technology 70 (1999) 249-253.

[225] F. Ma, M.A. Hanna, Bioresource Technology 70 (1999) 1-15.

[226] V. Varela Guerrero, D.F. Shantz, Industrial & Engineering Chemistry Research 48 (2009) 10375-10380.

[227] G.W. Huber, J.N. Chheda, C.J. Barrett, J.A. Dumesic, Science 308 (2005) 1446-1450.

[228] J.N. Chheda, G.W. Huber, J.A. Dumesic, Angew. Chem. Int. Ed. 46 (2007) 7164-7183.

APPENDIX A

ADDITIONAL FIGURES FROM CHAPTER III

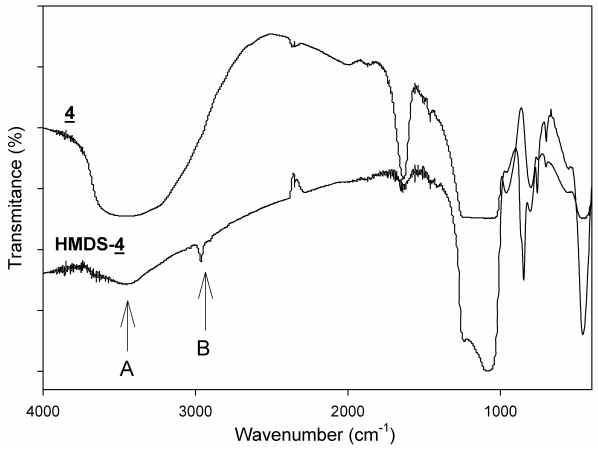

Figure A1. FTIR spectra of sample **4** and **HMDS-4** with 0.8mmol/g amine loading

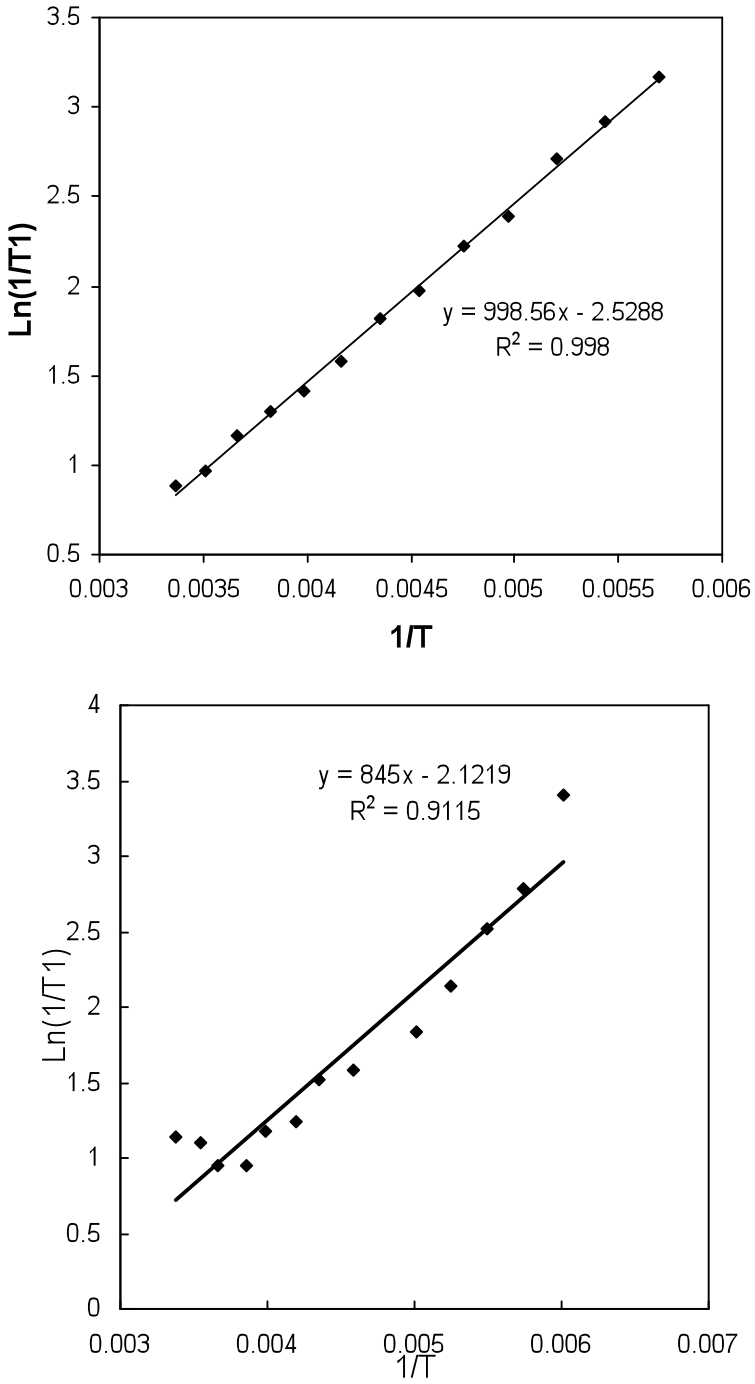

Figure A2. Determination of the activation energies for **1**-MCM-41 (bottom) and **1**-SBA-15 (top) made with deuterated HMDS.

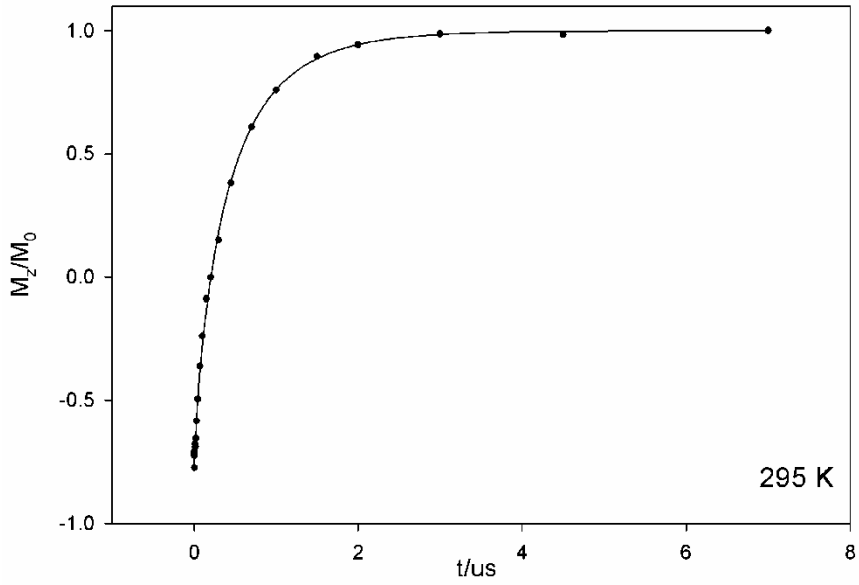

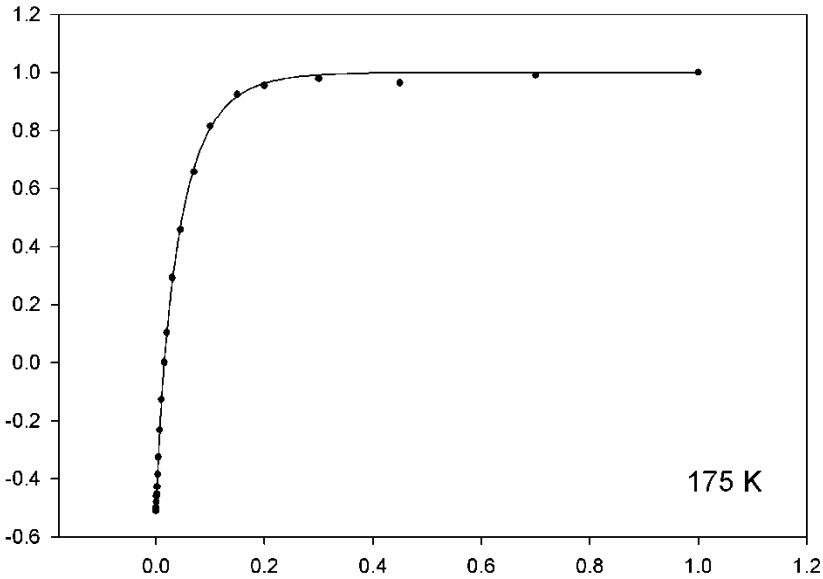

Figure A3. Plot M_z/M_o for d_9-**1**-SBA-15 used to determine spin-lattice relaxation values.

APPENDIX B

ADDITIONAL FIGURES FROM CHAPTER IV

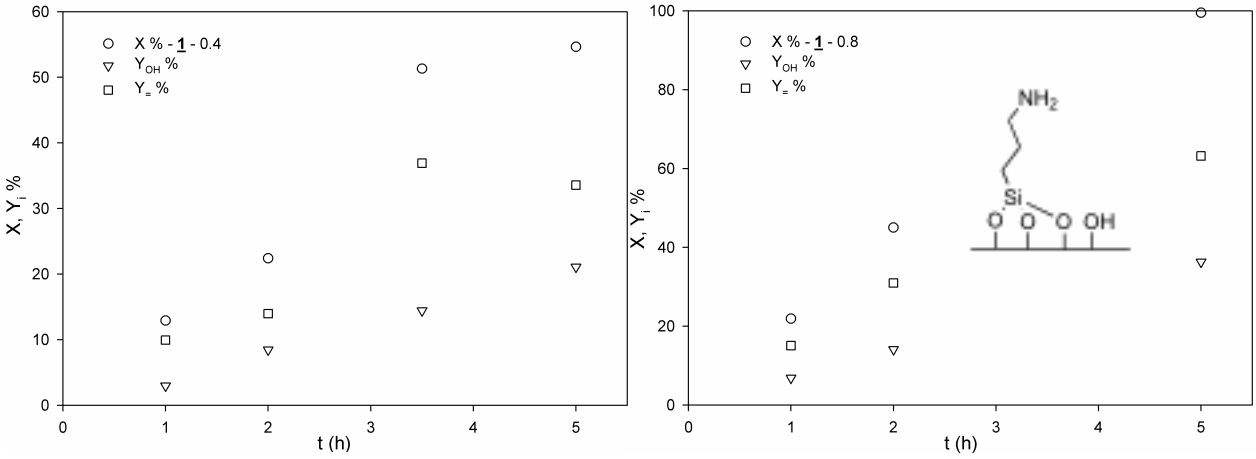

Figure B1. Conversion and yields for **1**-MCM-41 as a function of amine loading (0.4 (left), and 0.8 (right) meq/g target loading), Y_{OH}% is the yield of nitroalcohol product, $Y_{=}$% is the yield of nitrostyrene product.

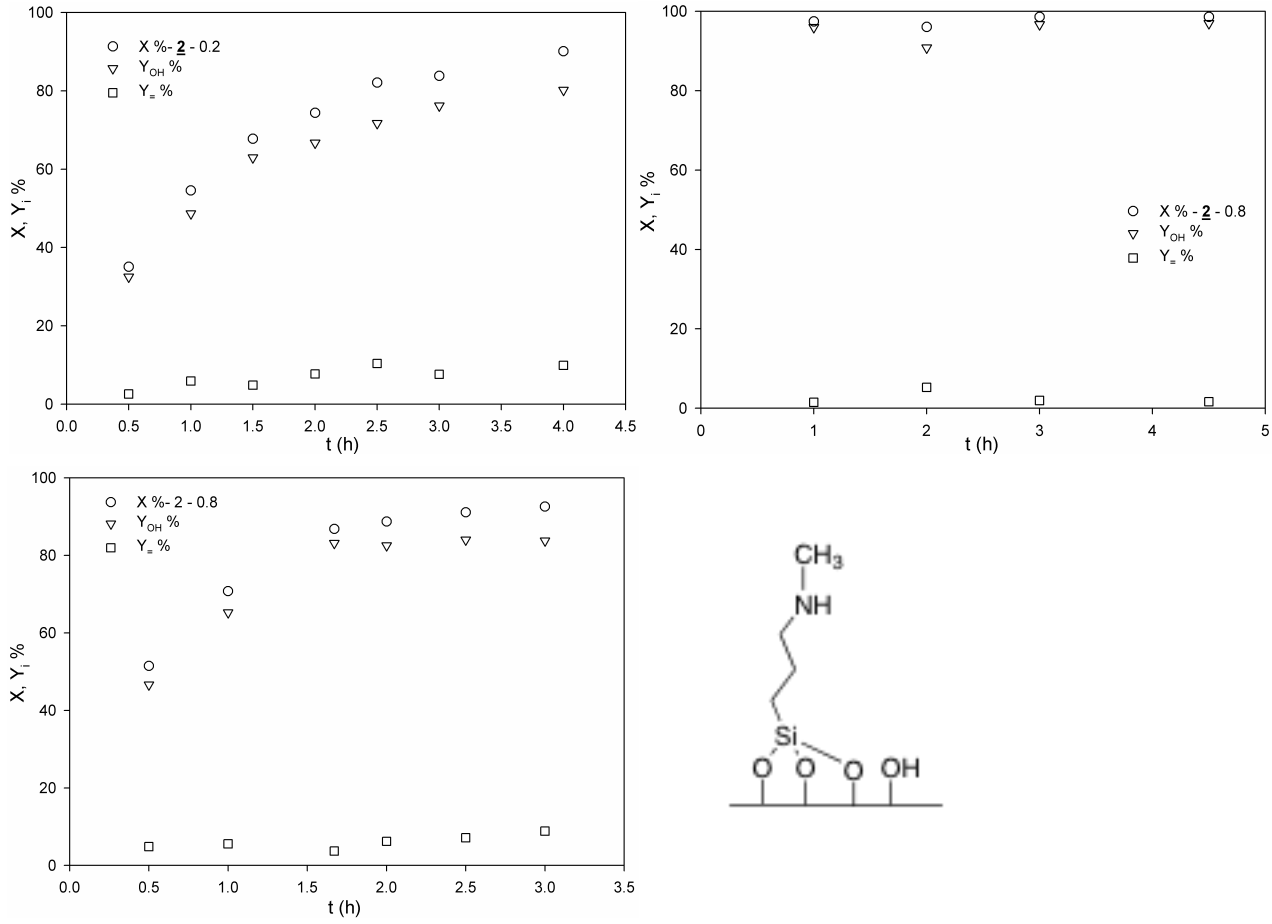

Figure B2. (Clockwise from top right) Conversion and yields for **2**-MCM-41 as a function of amine loading (0.2, 0.8 meq/g target loading), and 0.8 meq/g target loading with 3 times of reactants as 0.2 meq/g loading sample.

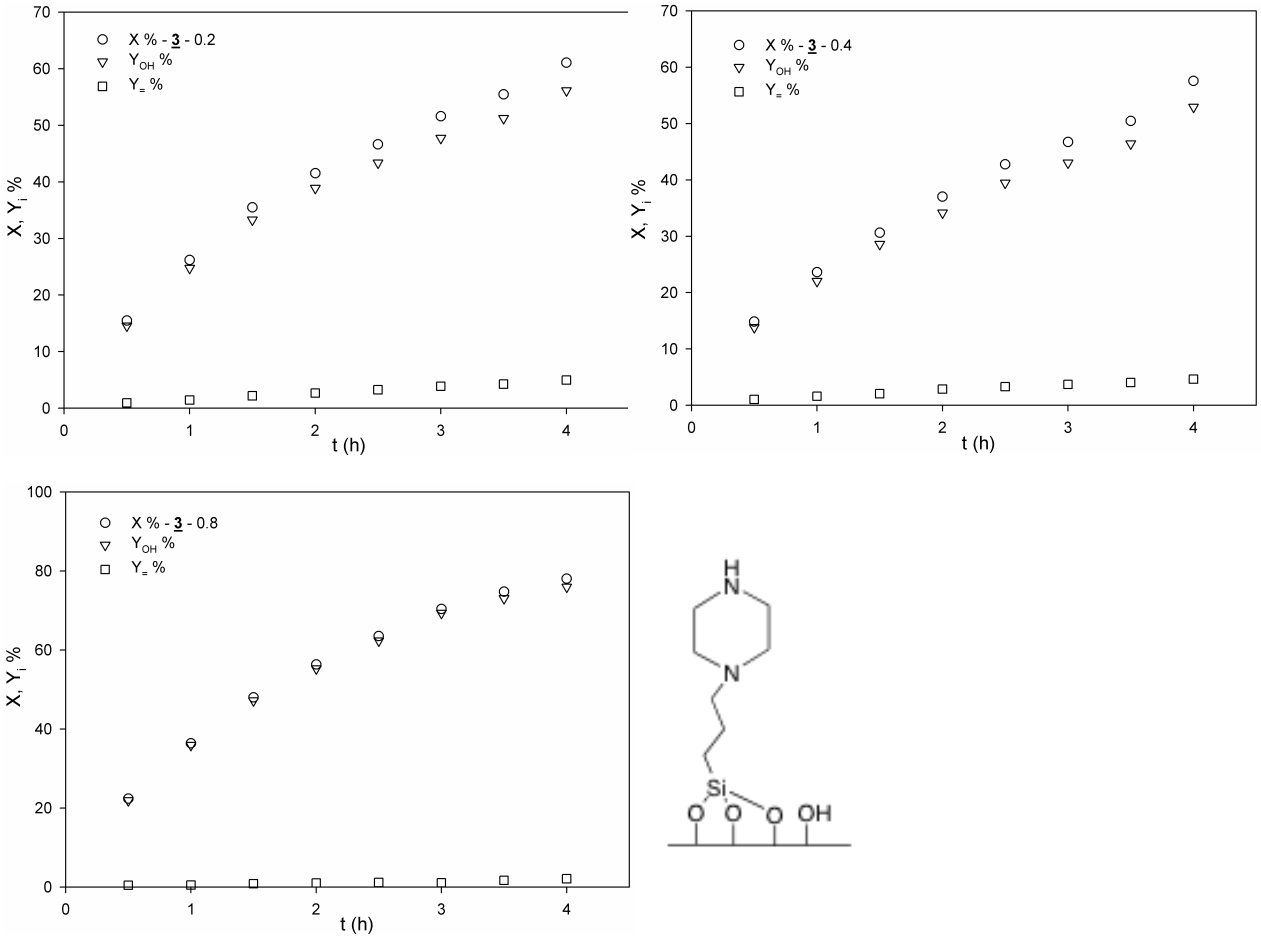

Figure B3. (Clockwise from top left) Conversion and yields for **3**-MCM-41 as a function of amine loading (0.2, 0.4, and 0.8 meq/g target loading).

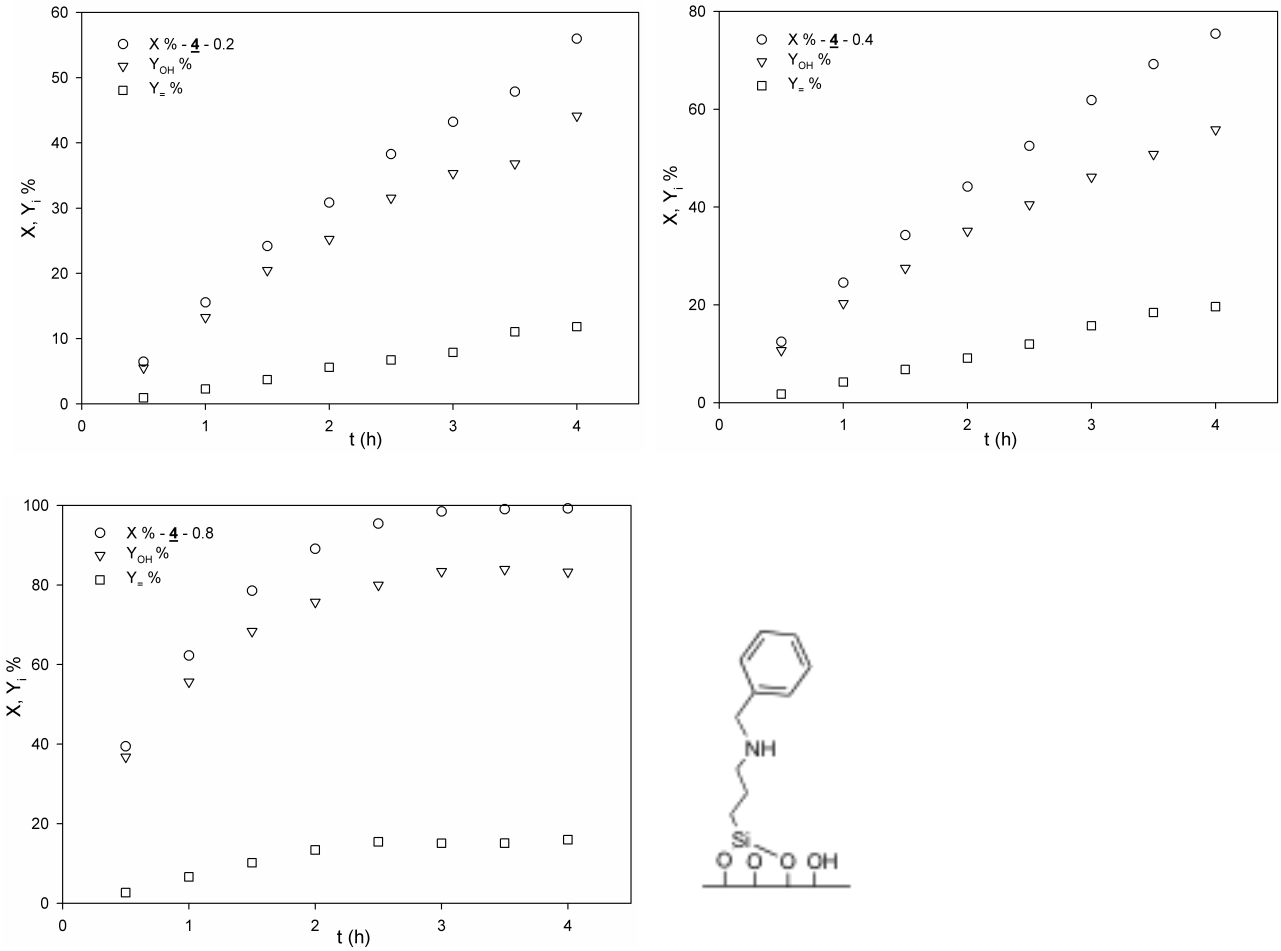

Figure B4. (Clockwise from top left) Conversion and yields for **4**-MCM-41 as a function of amine loading (0.2, 0.4, and 0.8 meq/g target loading).

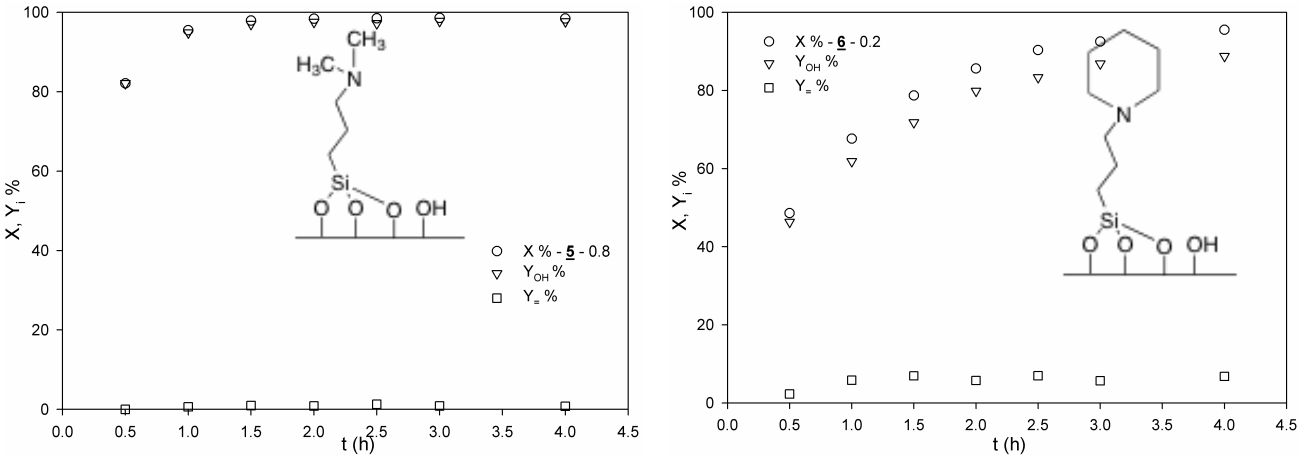

Figure B5. Conversion and yields for **5**-MCM-41 with 0.8 meq/g loading (left) and **6**-MCM-41 with 0.2 meq/g loading (right).

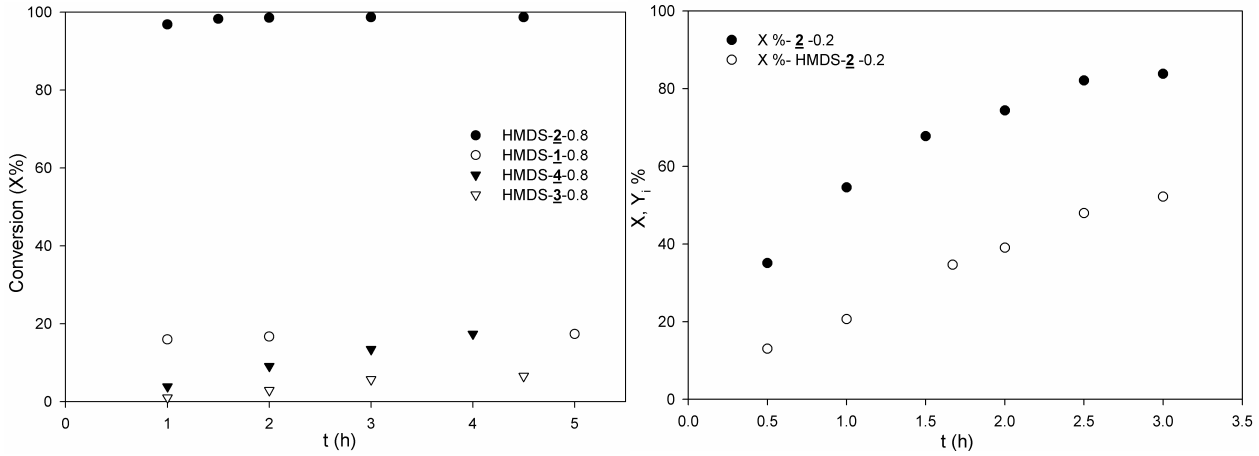

Figure B6. Conversion versus time for HMDS treated samples.

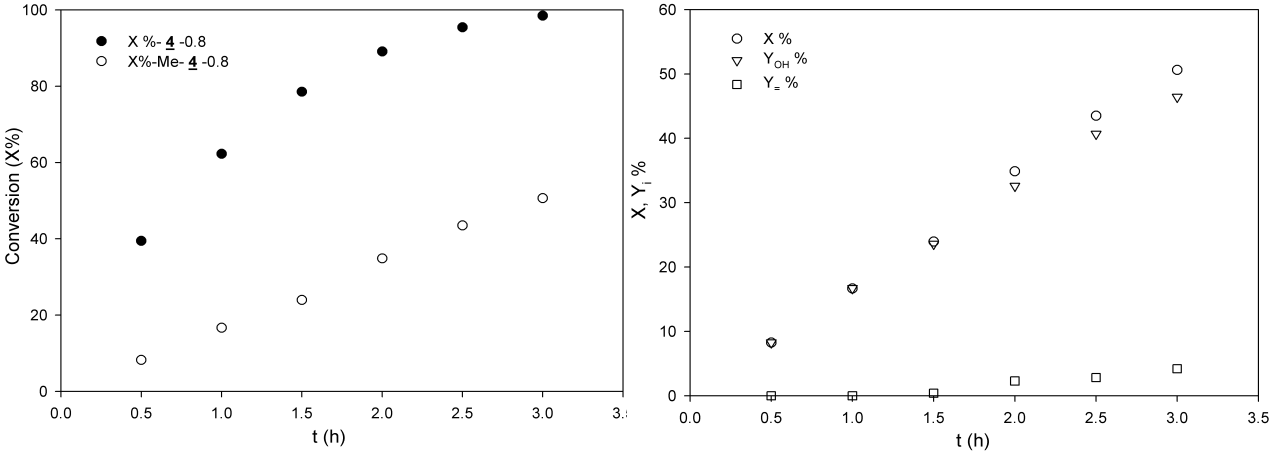

Figure B7. Conversion and yield versus time for **4** and samples of **4** treated with methyltrimethoxysilane.

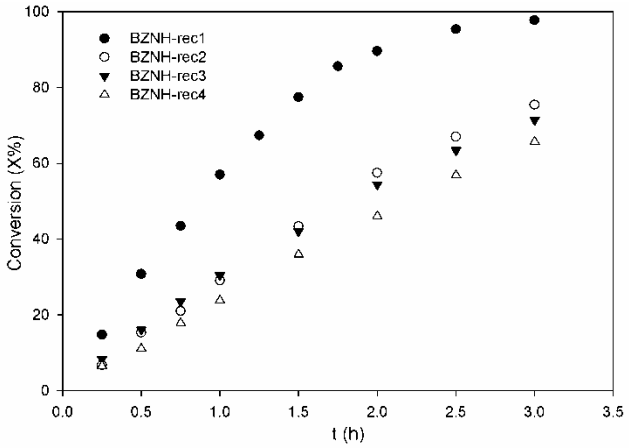

Figure B8. Conversion versus time for **4**-MCM-41 (0.8 meq/g) in recycle reactions.

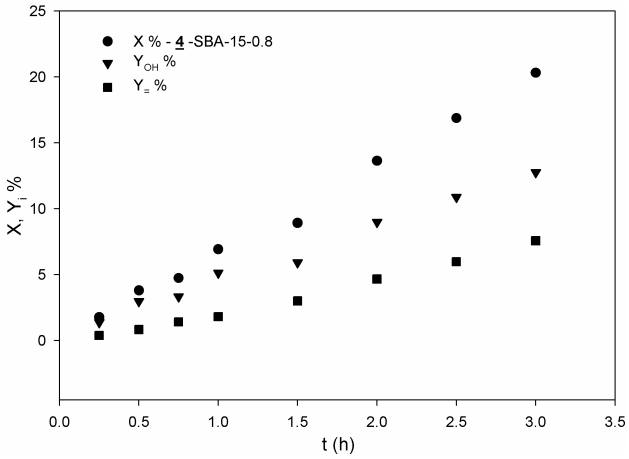

Figure B9. Conversion and yields versus time for **4**-SBA-15.

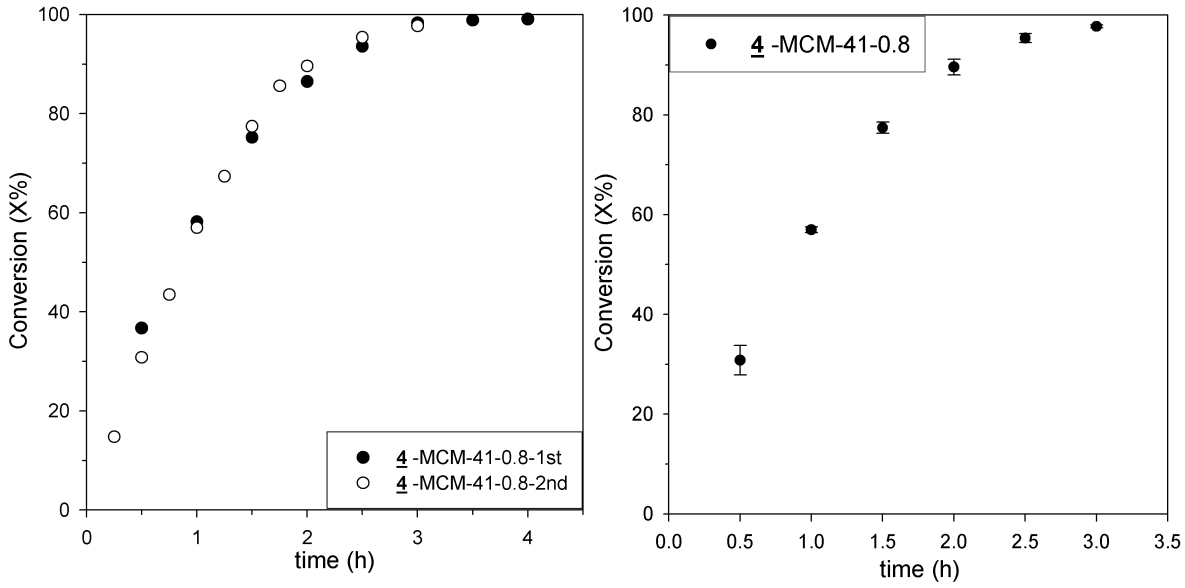

Figure B10. Conversions versus time for **4**-MCM-41-0.8 in multiple runs of the Nitroaldol reaction, keeping all the conditions constant.

VITA

Name: Qingqing Wang

Email Address: oliveqq@tamu.edu

Mail Address: 3122 TAMU, College Station, TX, 77843

Education: B.S., Materials Science and Engineering, Zhejiang University, 2003

M.S., Materials Science and Engineering, Zhejiang University, 2006

Ph.D., Chemical Engineering, Texas A&M University, 2011

Publications:

Qingqing Wang and Daniel F. Shantz, "Nitroaldol Reactions Catalyzed by Amine - MCM-41 Hybrids," *Journal of Catalysis*, 271 (2010) 170-177.

Qingqing Wang, Victor Varela, Anirban Ghosh, Seunguk Yeu, Jonathan D. Lunn, and Daniel F. Shantz, "Synthesis, Characterization, and Catalytic Testing of Dendron-OMS Nanocomposites," *Journal of Catalysis*, 269 (2010) 15-25.

Qingqing Wang, Edgar Jordan, and Daniel F. Shantz, "2H NMR Studies of Simple Organic Groups Covalently Attached to Ordered Mesoporous Silica," *Journal of Physical Chemistry C*, 113 (2009) 18142-18151.

Qingqing Wang and Daniel F. Shantz, "Ordered Mesoporous Silica-based Inorganic Nanocomposites", *Journal of Solid State Chemistry*, 181 (2008) 1662-1672.